



Universitetet
i Stavanger

FACULTY OF SCIENCE AND TECHNOLOGY

MASTER'S THESIS

Study programme/specialisation: Master of Science in Offshore Technology, Marine and Subsea Technology	Spring semester, 2017 Open/ Confidential
Author: Rohan Shabu Joseph (signature of author)
Supervisor: Prof. Muk Chen Ong Co-supervisors: Dr. Jungao Wang, Prof. Jasna Bogunovic Jakobsen	
Title of master's thesis: Numerical Investigation on the Vortex-Induced Vibration Effects of a Deep Sea Mining Riser	
Credits(ECTS): 30	
Keywords: VIV, Deep sea mining, Marine riser, Vessel motion, Response frequency model	Number of pages: 108 + supplemental material/other: 15 Stavanger, 14 June 2017

(This page intentionally left blank)

Numerical Investigation on the Vortex-Induced Vibration Effects of a Deep Sea Mining Riser

Rohan Shabu Joseph

Spring 2017

MASTER THESIS

Department of Mechanical and Structural Engineering and Materials Science

University of Stavanger

Main supervisor: Prof. Muk Chen Ong

Co-supervisors: Dr. Jungao Wang

Prof. Jasna Bogunović Jakobsen

(This page intentionally left blank)

Abstract

In recent times, the deep sea mining industry has attracted growing attention globally as it targets mining activities in deeper waters of up to 6,000 m depth. Many of the technologies used in deep sea mining have been adopted from the offshore oil and gas industry. A self-propelled Seafloor Production Tool (SPT) is placed on the sea bottom and collects minerals from the seabed. These are then transported to the surface vessel through a Riser and Lifting System (RALS). The lift is achieved by either pneumatic or hydraulic means.

The major part of the RALS is the vertical riser that runs from the vessel and is connected to the SPT via a flexible hose, which decouples the relative motion between the riser and the SPT. Since the restriction by the flexible hose is relatively negligible, the bottom of the riser is free to move and large motions are expected under top vessel motion. As in the case of offshore oil and gas industry, the design, analysis and maintenance of the riser (major part of RALS) is one of the most challenging task.

One major issue for the marine riser is the vortex-induced vibrations (VIVs) caused by the shedding of vortices by the flow around the riser. The back and forth motion of the riser in the water due to the vessel motion can also generate an equivalent oscillatory flow which can cause VIV (Wang et al., 2016b). The present work aims to study the VIV effects due to vessel motion on a deep sea mining riser. An empirical model is proposed to predict the VIV response of a riser under vessel motions of low Keulegan-Carpenter (KC) numbers with the vessel motion conditions under a fatigue sea-state. Numerical method validation was carried against model test results and full-scale measurement data. The results of the validation were used to fine tune the model for predicting the VIV response of an ultra-long mining riser under vessel motions. Since the vessel motion-induced VIV would cause similar stresses and fatigue damage as the current induced VIV (Wang et al., 2016b), a fatigue damage analysis of the riser due to vessel motion induced VIV is also conducted. Further, VIV due to ocean current is also investigated and compared with the VIV due to vessel motions.

Acknowledgement

This thesis has been submitted in partial fulfillment of the requirement for completing the degree of Master of Science in Offshore Technology at the University of Stavanger.

I take this opportunity to express my gratitude to all those who have provided me with valuable guidance and support.

First of all, I would like to thank my supervisor Prof. Muk Chen Ong for giving me this opportunity to work on this challenging and interesting topic. His constant motivation and encouragement helped me a lot towards the completion of this work.

I would like to extend my heartfelt gratitude to Dr. Jungao Wang, whose valuable advices and inputs were the key for the completion of this thesis. Despite his busy schedule, he took time to review my progress and was always available to guide me with his inputs and suggestions. Without his comments and remarks, this thesis report would not have been perfected. I would also like to thank Prof. Jasna Bogunović Jakobsen for her feedback on the work in this thesis.

I would like to express my deepest thanks to Dr. Lin Li for helping me with her expertise in the areas of vessel motion and mooring systems. Also, I would like to thank Dr. Etienne Cheynet for his valuable inputs regarding accelerometers and acceleration data.

I gratefully acknowledge BP and MIT for sharing the full-scale measurement data in the VIV Data Repository hosted by Center for Ocean Engineering, MIT.

Finally, I would like to thank my parents and my friends for their affection and support during my stay in Stavanger.

Contents

Abstract	i
Acknowledgement	ii
1 Introduction	1
1.1 Background and Motivation	1
1.2 Objectives	4
1.3 Outline of the Thesis	4
2 Theory	7
2.1 Vortex Shedding and Vortex Induced Vibration	7
2.1.1 Vortex shedding	7
2.1.2 Vortex induced vibration and lock-in	8
2.2 Governing Physical Parameters of VIV	9
2.2.1 Reynolds number	9
2.2.2 Vortex shedding frequency	10
2.2.3 Mass ratio	12
2.2.4 Reduced velocity	12
2.2.5 Keulegan-Carpenter (KC) number	13
2.3 Semi-empirical VIV Prediction Method	15
3 Empirical Model for Prediction of Vessel Motion-induced VIV	19
3.1 Introduction	19
3.2 Proposed Empirical Prediction Model	21
3.2.1 Equivalent current profile	21

3.2.2	Representative KC number	24
3.2.3	Response frequency model for low KC number cases	25
3.2.4	VIV prediction for high KC number cases	27
3.3	Vibration Amplitudes for Irregular Motions	28
4	Empirical Model Validation: Against Model Test Results	29
4.1	Introduction	29
4.2	Methodology	29
4.3	Validation Based on Water Intake Riser Model Test	30
4.3.1	Results and discussion	31
4.4	Validation Based on Free-Hanging Riser Model Test	36
4.4.1	Results and discussion	37
4.5	Discussion	45
5	Empirical Model Validation: Against Full-scale Measurements	47
5.1	Introduction	47
5.2	Full-scale Data Information	48
5.2.1	Riser configuration	48
5.2.2	Environment and current data	51
5.2.3	Instrumentation	51
5.2.4	Accelerations and events	51
5.2.5	Limitations	52
5.3	Data Analysis	53
5.4	Methodology	55
5.5	Results and Discussion	56
5.5.1	Vessel motion-induced VIV dominant cases	57
5.5.2	Ocean current-induced VIV dominant cases	71
5.5.3	Discussion	74
6	Numerical VIV Prediction of Deep Sea Mining Riser	77
6.1	Introduction	77

6.2	Riser Configuration	78
6.3	Simplifications and Assumptions	79
6.4	Case Studies	80
6.4.1	Regular motion case with $A=1.5$ m	81
6.4.2	Regular motion case with $A=2.5$ m	86
6.4.3	Regular motion case with $A=5$ m	89
6.4.4	Irregular motion case	93
6.4.5	Current-induced VIV case	98
6.5	Discussion	100
7	Conclusions	103
	Bibliography	105
A	Small-scale Riser Model Tests: Comparison of Eigen Frequencies	109
B	Modelling of Drilling Riser	111
C	Hydrodynamic Coefficients used for Deep Sea Mining Riser	113
D	MATLAB Codes for Acceleration Data Analysis	115
E	Full-scale Measurement Data Logger Specifications	121

List of Figures

1.1	Deep sea mineral deposits around the globe (Nautilus Minerals, 2016a)	2
1.2	Overview of Deep Sea Mining System (Nautilus Minerals, 2016b)	3
2.1	Cylinder exposed to uniform flow (Goharzadeh and Molki, 2014)	7
2.2	Mechanism of vortex shedding (Sumer and Fredsøe, 2006)	8
2.3	Vortex patterns behind a cylinder for various Re regimes	10
2.4	Variation of Strouhal number with Reynolds number	11
2.5	CF response of a cylinder in steady flow	13
2.6	Excitation zones along the structure exposed to a shear current	16
2.7	Excitation zones along the structure without overlapping frequencies	16
3.1	Illustration of velocities along the riser	21
3.2	Illustration of Equivalent Current Profile 1	22
3.3	Illustration of Equivalent Current Profile 2	23
3.4	Illustration of Equivalent Current Profile 3	24
3.5	Illustration of representative KC number	25
3.6	Flowchart illustrating the empirical frequency response model	27
4.1	Eigen modes and Eigen frequencies of the WIR model	32
4.2	Normalized mode shapes for the WIR model	32
4.3	Equivalent current profile for WIR	33
4.4	KC number distribution for WIR	33
4.5	Excitation frequencies for WIR	34
4.6	Response frequency along the riser from experiment for WIR (Wang et al., 2016c)	35

4.7	Comparison of RMS strain values for WIR	35
4.8	Comparison of RMS A/D for WIR	36
4.9	Eigen modes and Eigen frequencies of the free hanging riser model	38
4.10	Normalized mode shapes for the free hanging riser model	38
4.11	Equivalent current profile for Case 1	39
4.12	KC number distribution for Case1	39
4.13	Response freq. along riser for Case 1 from experiment (Wang et al., 2016a) .	40
4.14	Excitation frequencies from VIVANA for Case 1	40
4.15	Strain values for Case 1	41
4.16	Time varying strain from experiment for Case 1 (Wang et al., 2016a)	41
4.17	Equivalent current profile for Case 2	42
4.18	KC number distribution for Case 2	43
4.19	Response freq. along riser for Case 2 from experiment (Wang et al., 2016a) .	43
4.20	Excitation frequencies from VIVANA for Case 2	44
4.21	Strain values for Case 2	45
4.22	Time varying strain from experiment for Case 2 (Wang et al., 2016a)	45
5.1	Configuration of the drilling riser (BP and 2H Offshore, 2008)	49
5.2	Riser tension and mud density (BP and 2H Offshore, 2008)	50
5.3	Acceleration time series at a particular sensor showing poor quality data . .	52
5.4	Acceptable acceleration time series at a particular sensor	53
5.5	An example of acceleration spectrum	55
5.6	Eigen modes and eigen frequencies for the drilling riser	56
5.7	Normalized mode shapes for the drilling riser	56
5.8	Equivalent current profile and the ocean current profile (Event 58)	57
5.9	Spectra of acceleration in X direction across all loggers (Event 58)	58
5.10	Spectra of acceleration in Y direction across all loggers (Event 58)	58
5.11	Displacement spectrum of logger S01 (Event 58)	59
5.12	KC number distribution along the riser (Event 58)	60
5.13	Excitation frequencies vs. displacement spectrum at S07 (Event 58)	60

5.14	Comparison of RMS A/D along the riser (Event 58)	61
5.15	Equivalent current profile and the ocean current profile (Event 612)	62
5.16	Spectra of acceleration in X direction across all loggers (Event 612)	62
5.17	Spectra of acceleration in Y direction across all loggers (Event 612)	63
5.18	Displacement spectrum of logger S01 (Event 612)	63
5.19	KC number distribution along the riser (Event 612)	64
5.20	Excitation frequencies vs. displacement spectrum at S05 (Event 612)	65
5.21	Comparison of RMS A/D along the riser (Event 612)	65
5.22	Equivalent current profile and the ocean current profile (Event 413)	66
5.23	Comparison of shedding frequencies (Event 413)	67
5.24	Spectra of acceleration in X direction across all loggers (Event 413)	68
5.25	Spectra of acceleration in Y direction across all loggers (Event 413)	68
5.26	Displacement spectrum of logger S01 (Event 413)	69
5.27	KC number distribution along the riser (Event 413)	69
5.28	Excitation frequencies vs. displacement spectrum at S09 (Event 413)	70
5.29	Comparison of RMS A/D along the riser (Event 413)	70
5.30	Equivalent current profile and the ocean current profile (Event 434)	71
5.31	Spectra of acceleration in X direction across all loggers (Event 434)	72
5.32	Spectra of acceleration in Y direction across all loggers (Event 434)	73
5.33	Excitation frequencies vs. displacement spectrum at S03 (Event 434)	73
5.34	Comparison of RMS A/D along the riser (Event 434)	74
6.1	Configuration of the riser	78
6.2	Eigenmodes and eigen frequencies for the deep sea mining riser	80
6.3	Normalized mode shapes for the deep sea mining riser	81
6.4	Equivalent current profile (regular motion case with A=1.5 m)	82
6.5	KC number distribution (regular motion case with A=1.5 m)	82
6.6	Excitation frequencies (regular motion case with A=1.5 m)	83
6.7	RMS A/D along the riser (regular motion case with A=1.5 m)	84
6.8	Strain along the riser (regular motion case with A=1.5 m)	84

6.9	Fatigue damage along the riser (regular motion case with A=1.5 m)	85
6.10	Equivalent current profile (regular motion case with A=2.5 m)	86
6.11	KC number distribution (regular motion case with A=2.5 m)	87
6.12	Excitation frequencies (regular motion case with A=2.5 m)	87
6.13	RMS A/D along the riser (regular motion case with A=2.5 m)	88
6.14	Strain along the riser (regular motion case with A=2.5 m)	88
6.15	Fatigue damage along the riser (regular motion case with A=2.5 m)	89
6.16	Equivalent current profile (regular motion case with A=5 m)	90
6.17	KC number distribution (regular motion case with A=5 m)	90
6.18	Excitation frequencies (regular motion case with A=5 m)	91
6.19	RMS A/D along the riser (regular motion case with A=5 m)	92
6.20	Strain along the riser (regular motion case with A=5 m)	92
6.21	Fatigue damage along the riser (regular motion case with A=5 m)	93
6.22	Displacement spectrum of the vessel motion (irregular motion case)	94
6.23	Equivalent current profile (irregular motion case)	94
6.24	The KC number distribution along the riser (irregular motion case)	95
6.25	Excitation frequency along the riser (irregular motion case)	96
6.26	RMS A/D along the riser (irregular motion case)	96
6.27	Strain along the riser (irregular motion case)	97
6.28	Fatigue damage along the riser (irregular motion case)	97
6.29	Ocean current profile (current-induced VIV case)	98
6.30	Excitation frequencies along the riser (current-induced VIV case)	99
6.31	Strain along the riser (current-induced VIV case)	99
6.32	Fatigue damage along the riser (current-induced VIV case)	100

List of Tables

3.1	Value of the ratio N for various KC regimes (Williamson, 1985)	20
3.2	Frequency information from experiment (Wang et al., 2016c)	20
4.1	Properties of model riser (Wang et al., 2016c)	31
4.2	Riser motions (Wang et al., 2016c)	31
4.3	Properties of model riser (Wang et al., 2016a)	37
4.4	Riser motions (Wang et al., 2016a)	37
5.1	Locations of the loggers	50
5.2	Events considered for analysis	57
6.1	Properties of the riser	79
6.2	Vessel motions for regular motion case with $A=1.5$ m	81
6.3	Vessel motions for regular motion case with $A=2.5$ m	86
6.4	Vessel motions for regular motion case with $A=5$ m	89
6.5	Comparison of case studies	100

List of Abbreviations

ADCP	Acoustic Doppler Current Profiler
CF	Cross Flow
FBG	Fiber Brag Grating
IL	In Line
KC	Keulegan-Carpenter
MSL	Mean Sea Level
RALS	Riser and Lifting System
RMS	Root Mean Square
SMS	Seafloor Massive Sulfides
SPT	Seafloor Production Tool
VIV	Vortex-Induced Vibration
WIR	Water Intake Riser

List of Symbols

f_n	Natural frequency
-------	-------------------

f_v	Vortex shedding frequency
f_{dom}	Dominant response frequency
f_{im}	Imposed motion/Vessel motion frequency
f_{resp}	Response frequency
St^*	Equivalent Strouhal number
V_r	Reduced velocity
A/D	Amplitude to Diameter ratio
Re	Reynolds number
St	Strouhal number

Chapter 1

Introduction

1.1 Background and Motivation

The deep seafloor holds huge resource potential in the form of deposits of manganese nodules, cobalt rich crusts, polymetallic nodules and Seafloor Massive Sulfides (SMS). These deposits, which are found at depths of upto 6,000 m below the sea level, have attracted global interests in deep sea mining since 1960's. Huge demand for minerals coupled with rapidly declining land-based deposits have prompted companies to venture into commercial scale deep sea mining. Many companies are now actively focusing on SMS deposits which contain appreciable amounts of copper and gold. These deposits are located at comparatively shallower depths of less than 2,000 m (Hoagland et al., 2010). Figure 1.1 shows the estimated resources of SMS and polymetallic nodules in oceanic waters around the globe. Though a lot of research and conceptual studies have been conducted in the area of deep sea mining, the industry is still in its early days. In 2011, Nautilus Minerals Inc., a deep sea mining company, have obtained mining license for an SMS deposit site located 30 km offshore Papua New Guinea. The exploration and development of this site, which is named *Solwara-1*, is being undertaken and the production is expected to start in the year 2018 (Berndt, 2015).

Many of the technologies used in deep sea mining have been adopted from the offshore

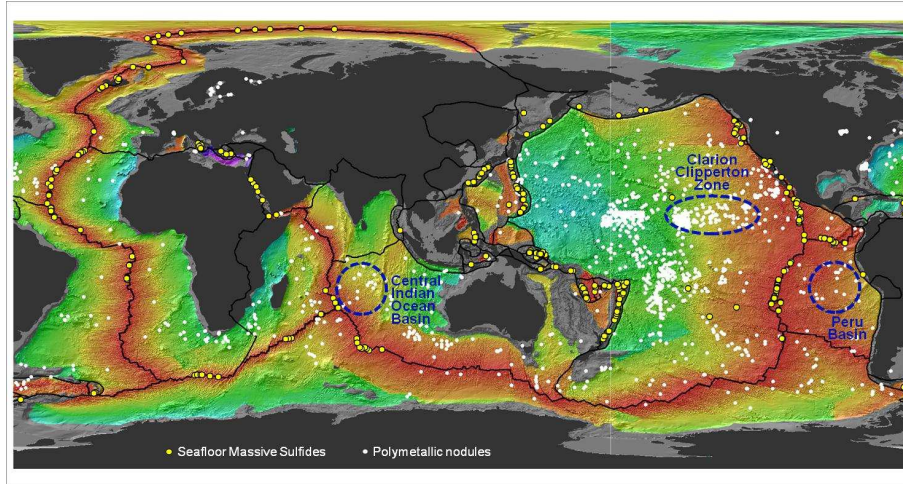


Figure 1.1 Deep sea mineral deposits around the globe (Nautilus Minerals, 2016a)

oil and gas industry. According to Chung and Tsurusaki (1994), the 1980's saw significant technological developments in deep sea nodule-mining system and subsystems like hoisting systems, pipe deployment and retrieval systems and control systems. The major operations involved in deep sea mining are (1) exploration survey, (2) collection of nodules from the seabed, (3) hoisting the nodules to the surface vessel, (4) transportation to land and (5) processing of nodules either offshore or onshore. Hence, the mining system can be thought of as an integration of seafloor miner system, riser and lifting system, ship system and transportation system. An overview of the deep sea mining system is shown in Figure 1.2. The Seafloor Production Tool (SPT) is a self-propelled vehicle, which moves on the seafloor and executes the task of excavating the minerals. These minerals are then collected by the SPT and hoisted to the production support vessel using the Riser and Lifting System (RALS). Further processing and transportation occurs at the surface.

The Riser and Lifting System (RALS) consists of a riser deployed from the production support vessel and a buffer equipment at the bottom end of the riser, which contains the pumping system for the nodules. The buffer is connected to the SPT using a flexible hose, which allows for the relative motion of the SPT with respect to the riser. This configuration means that the bottom end of the riser is free to move with very little resistance from the flexible hose. As the mining industry targets deeper and deeper waters, the length of the riser increases and many technical challenges arise as a result.

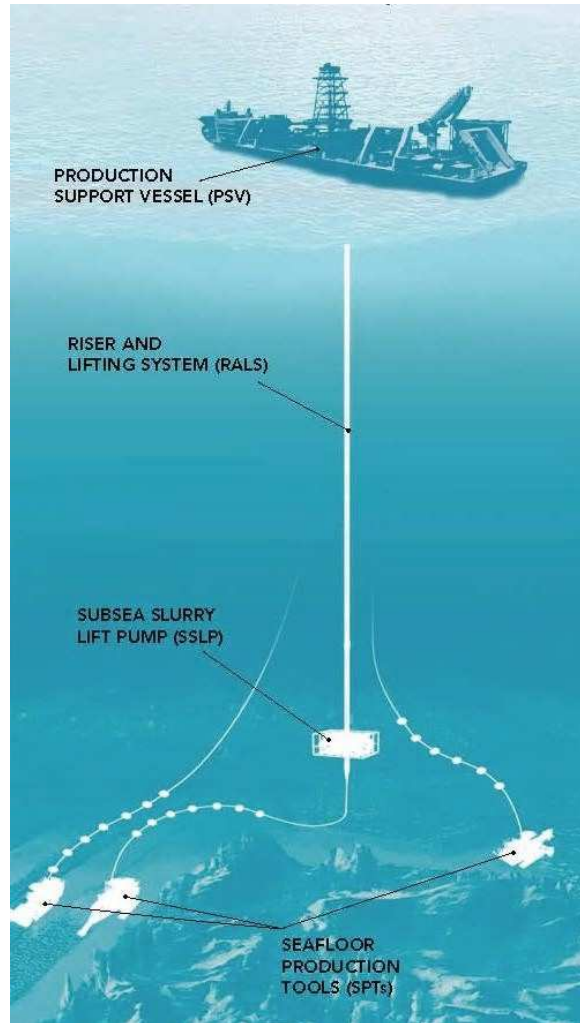


Figure 1.2 Overview of Deep Sea Mining System (Nautilus Minerals, 2016b)

One of the key issues related to such a long riser is the Vortex-Induced Vibration (VIV), which is caused by the shedding of vortices around the riser in a current. Researches have confirmed that VIV can also occur to a flexible riser due to pure vessel motion (Wang et al., 2016b). Vessel motions, predominantly the surge and the sway, can create an equivalent oscillating current due to the relative motion of the riser in water. This vessel motion-induced VIV can cause similar fatigue damage to the riser as the ocean current-induced VIV (Wang et al., 2016b). The phenomenon of VIV in marine slender systems is still not fully comprehended and we have very little understanding of the VIV due to vessel motions. Although various numerical tools such as VIVANA and Shear7 are available to analyze the VIV of flexible systems, they are mostly suitable for ocean current induced cases and not for vessel motion-

induced cases. The present work attempts to bridge that gap and propose an empirical model for the prediction of vessel motion-induced VIV of a riser based on VIVANA software.

1.2 Objectives

The main objectives of this Master thesis study are as follows:

1. Formulate an empirical model for the prediction of vessel motion-induced VIV of a riser.
2. Validate the empirical model with the results from available riser model tests.
3. Validate the empirical model using full-scale data from actual field measurements of a drilling riser.
4. Use the validated empirical model to predict the VIV response due to vessel motions for an ultra-long deep sea mining riser .

1.3 Outline of the Thesis

The rest of the thesis is organized as follows:

Chapter 2 gives the theoretical background of the present work. A brief explanation on the phenomenon of VIV is provided and the key parameters related to VIV are defined.

In Chapter 3, the empirical model for the prediction of vessel motion-induced VIV is proposed. A brief explanation about the steps involved is presented.

In Chapter 4, the proposed model is validated against experimental results from small-scale riser model tests. The results from experiment is compared with the results from numerical analysis to validate the model.

In Chapter 5, the vessel motion-induced VIV is firstly identified in the full-scale measurements of a drilling riser and is then used for validation. The behaviour of a full-scale riser with

regard to vessel motion-induced VIV is investigated.

In Chapter 6, the validated empirical model is applied to an ultra-long deep sea mining riser. The VIV due to vessel motion is investigated and fatigue analysis is conducted. Current induced VIV is also studied and compared with vessel motion-induced VIV.

Chapter 7 summarizes the thesis work.

Chapter 2

Theory

2.1 Vortex Shedding and Vortex Induced Vibration

2.1.1 Vortex shedding

A cylindrical structure exposed to a uniform flow is shown in Figure 2.1.

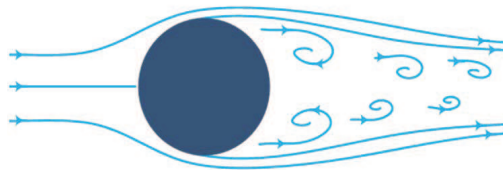


Figure 2.1 Cylinder exposed to uniform flow (Goharzadeh and Molki, 2014)

When the fluid flows past the cylinder, a boundary layer is formed over its surface. This boundary layer is separated at the back end of the cylinder due to the adverse pressure gradient formed because of the diverging geometry of the cylinder cross-section. As a result, a shear layer, which separates itself from the surface, is formed. The fluid flowing over the

cylinder surface contains a significant amount of vorticity. This vorticity is fed into the shear layer as well, which makes it to roll up into a vortex. Similarly, another vortex which rotates in the opposite direction, is formed from the other side of the cylinder. This pair of vortices are largely unstable and one of them will grow larger than the other. The larger vortex attracts the other one across the wake region behind the cylinder. Since both the vortices rotate in opposite directions, the approach of the smaller vortex of opposite vorticity will cut off further supply of vorticity to the larger one. At this instant the larger vortex is shed and moves downstream of the flow. When the vortex is shed, a new vortex will be formed at that side which is attracted towards the larger vortex on the other side. This leads to the shedding of vortex on the other side. This process continues and vortices are shed alternatively from both the sides (Sumer and Fredsøe, 2006).

The vortex shedding mechanism is depicted in Figure 2.2. The vortex B is drawn towards the larger vortex A. Once vortex A is shed, a new vortex C is formed there which in turn is drawn towards the vortex B.

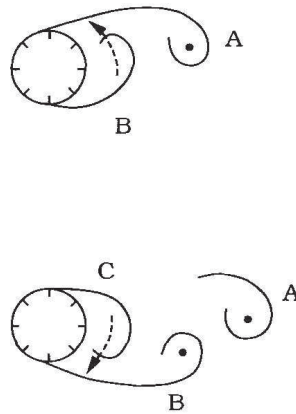


Figure 2.2 Mechanism of vortex shedding (Sumer and Fredsøe, 2006)

2.1.2 Vortex induced vibration and lock-in

When slender marine structures like risers, pipeline free spans and mooring lines are exposed to a current flow, they may experience oscillations or vibrations. These vibrations are caused due to the shedding of vortices around the structure and when the shedding

frequency approaches the natural frequency of the structure. These are called Vortex Induced Vibrations (VIV).

A cylinder in still water will have many natural frequencies (f_n) based on the different modes of vibrations. When the cylinder is exposed to a flow, vortex shedding occurs with a shedding frequency f_v . When this shedding frequency is equal to one of the natural frequencies of the cylinder, we have a resonance and the cylinder vibrates with a larger amplitude. The frequency of the response is equal to the other two frequencies. This is called as “lock-in”. Once we have a “lock-in”, the cylinder is said to experience VIV. It should be noted that in water, the added mass will vary and as a result the natural frequencies will also vary. Also, when the cylinder starts oscillating, the “effective diameter” will vary and as a result the vortex shedding frequency is not a constant. Hence, the response frequency of the cylinder will be a compromise between the natural frequency and vortex shedding frequency. VIV is a self-limiting process due to the hydrodynamic damping with increasing vibration amplitude, which means that if the amplitude exceeds a certain value, there will be no more transfer of energy from fluid to the cylinder but vice versa. The vibration along the direction of the flow is called as In-line (IL) VIV and the one perpendicular to the flow is called Cross-flow (CF) VIV. Generally, the amplitudes along the CF direction are much larger than the IL direction with IL frequency being twice that of CF frequency.

2.2 Governing Physical Parameters of VIV

2.2.1 Reynolds number

The flow around a cylinder can be described using a non-dimensional quantity called Reynolds Number, which is defined as,

$$Re = \frac{\text{Inertia Force}}{\text{Viscous Force}} = \frac{UD}{\nu} \quad (2.1)$$

where,

D is the diameter of the cylinder (Characteristic length of the object)

U is the velocity of the flow

ν is the kinematic viscosity of the fluid ($1 \times 10^{-6} \text{ m}^2/\text{s}$ at 20° C for water)

When the Re is less than 5, no separation of the flow occurs behind the cylinder. As we increase the Re , a fixed pair of symmetric vortices are formed. This holds for the range $5 < Re < 40$. When the Re is increased above 40, we get a laminar flow with alternate shedding of vortices. As the flow reaches the regime $300 < Re < 3 \times 10^5$, known as sub-critical flow region, the wake is fully turbulent with alternate shedding of vortex. Many of the realistic flow problems falls in this region. The vortex shedding patterns for various range of Re values are shown in Figure 2.3.





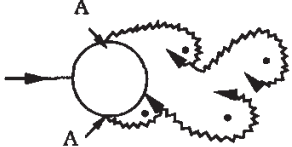
a) 	No separation. Creeping flow	$Re < 5$
b) 	A fixed pair of symmetric vortices	$5 < Re < 40$
c) 	Laminar vortex street	$40 < Re < 200$
d) 	Transition to turbulence in the wake	$200 < Re < 300$
e) 	Wake completely turbulent. A: Laminar boundary layer separation	$300 < Re < 3 \times 10^5$ Subcritical

Figure 2.3 Vortex patterns behind a cylinder for various Re regimes (Sumer and Fredsøe, 2006)

2.2.2 Vortex shedding frequency

The frequency of the vortex shedding of a fixed cylinder (i.e. shedding of a pair of vortices) is governed by the non-dimensional number known as Strouhal number. The Strouhal number

is defined as,

$$St = \frac{f_v D}{U} \quad (2.2)$$

where,

f_v is the vortex shedding frequency of a fixed cylinder subjected to steady flow

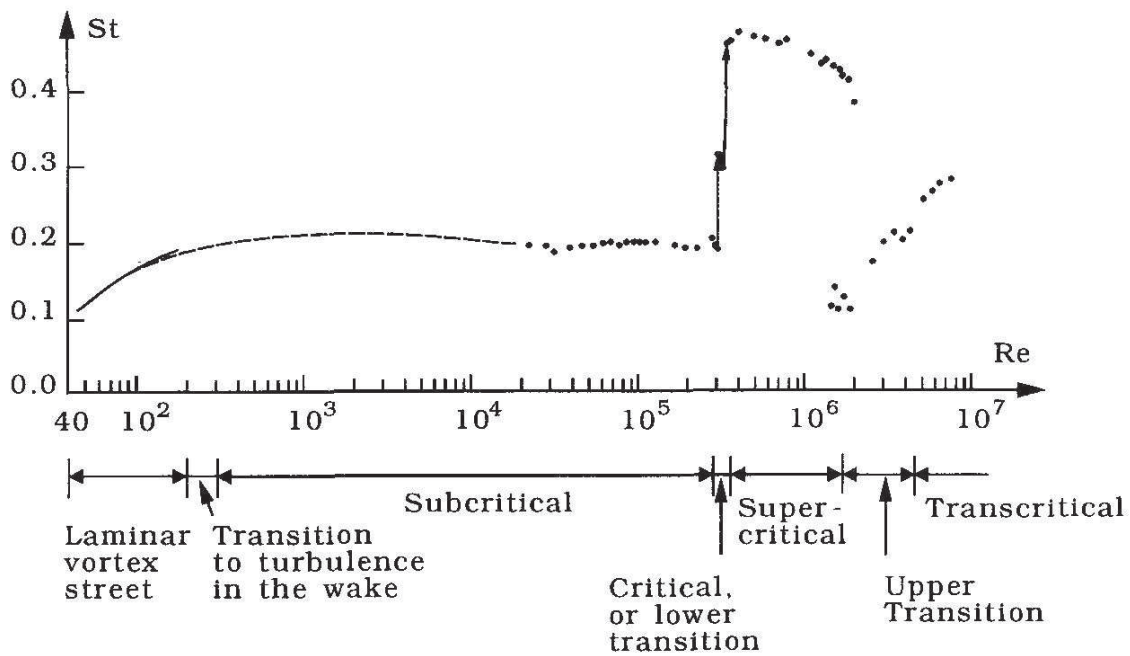


Figure 2.4 Variation of Strouhal number with Reynolds number (Sumer and Fredsøe, 2006)

Figure 2.4 shows the relationship between the Strouhal number and Reynolds number for a smooth cylinder. It can be seen that the Strouhal number remains a constant with a value of 0.2 throughout the sub-critical range. The Strouhal number is also a function of the roughness of the cylinder.

2.2.3 Mass ratio

Mass ratio is defined as the ratio of mass of the cylinder per unit length to the mass of the displaced fluid per unit length.

$$M = \frac{4m}{\rho\pi D^2} \quad (2.3)$$

where,

m is the mass of the cylinder per unit length

ρ is the fluid density

Mass ratio is a parameter which indicates the tendency of the structure to experience flow induced vibrations. Higher the mass ratio, lower will be the vibrations due to flow.

2.2.4 Reduced velocity

The non-dimensional parameter reduced velocity is defined as,

$$V_r = \frac{U}{f_i D} \quad (2.4)$$

where,

f_i is the natural frequency of the cylinder.

A reduced velocity can be found for each natural frequency of the cylinder. When a cylinder vibrates with a frequency f_i in a flow of constant velocity U , then V_r is the ratio of the wavelength of the flow trajectory ($U \times 1/f_i$) to the diameter of the cylinder (D) (Sumer and Fredsøe, 2006), i.e. in cross flow vibrations, it represents the travelling length during a vibration period w.r.t the diameter. The lock-in phenomenon can be explained using reduced velocity. From Figure 2.5, which is for a mass ratio of 5.3, it can be seen that the vibration starts to occur with large amplitudes when the ratio of vortex shedding frequency and natural frequency (y-axis) reaches 1 at around $V_r = 5$. When V_r is in the range of 6-8, the shedding frequency departs from the Strouhal law and follows the natural frequency of the system. This range is the lock-in range corresponding to the non-dimensional frequency region where there is positive C_{LV} (lift coefficient in phase with

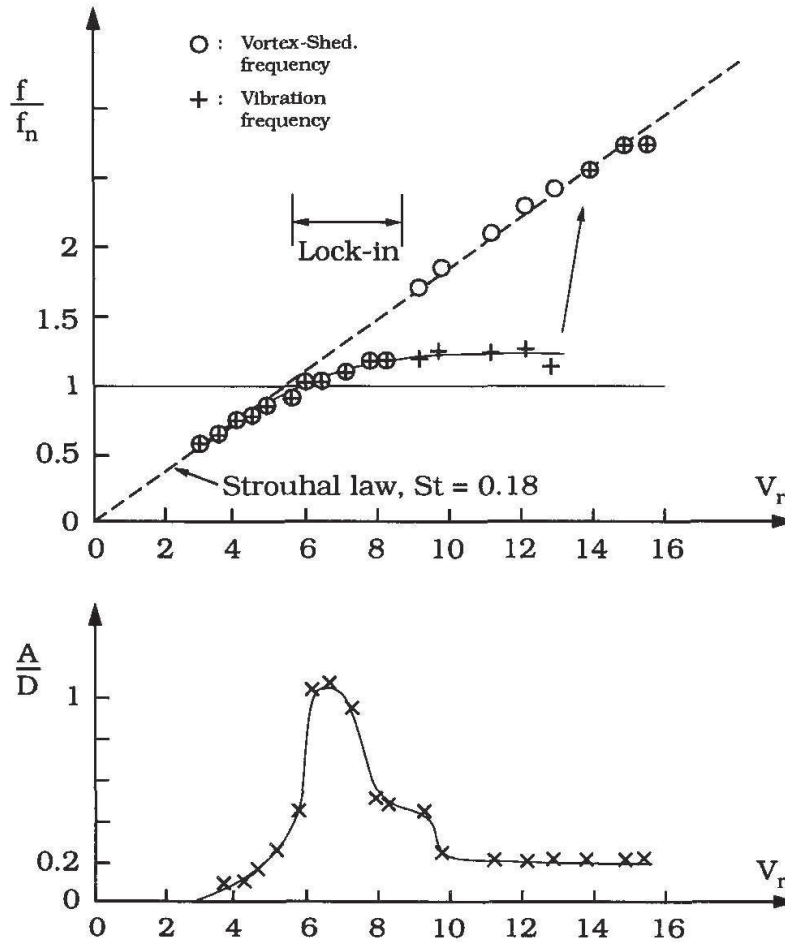


Figure 2.5 CF response of a cylinder in steady flow (Mass ratio=5.3) (Sumer and Fredsøe, 2006)

CF velocity) and larger amplitudes of vibration. After that, the vortex shedding frequency follows the Strouhal law.

2.2.5 Keulegan-Carpenter (KC) number

When a cylinder is subjected to an oscillatory flow, Reynolds number is not the only parameter that describes the flow. A parameter called Keulegan-Carpenter (KC) number also comes into picture. The KC number is defined as (Sumer and Fredsøe, 2006),

$$KC = \frac{U_m T_w}{D} \quad (2.5)$$

where,

U_m is the maximum velocity

T_w is the period of the oscillatory flow

KC number indicate the ratio of drag force to the inertia force on a cylinder.

In case of a harmonic flow,

$$U_m = \frac{2\pi A}{T_w} \quad (2.6)$$

where A is the amplitude of the motion

Hence, the KC number can be written as,

$$KC = \frac{2\pi A}{D} \quad (2.7)$$

This equation describes the distance covered by a water particle, under oscillatory flow, relative to the width of the cylinder. Large KC number indicates that the particles travel a longer distance relative to the width of the cylinder and results in separation from the surface and hence vortex shedding. Smaller KC number indicates shorter distance travelled and it is possible that the separation may not occur in this case (Sumer and Fredsøe, 2006).

Sumer and Fredsøe (2006) also gives the relation between VIV response frequency f_{resp} and frequency of the imposed motion of the cylinder f_{im} for different KC ranges based on the results from flexibly mounted rigid cylinder tests in oscillatory flows.

$$N = \frac{f_{resp}}{f_{im}} = \begin{cases} 2; 7 < KC < 15 \\ 3; 15 < KC < 24 \\ 4; 24 < KC < 32 \\ \dots \end{cases} \quad (2.8)$$

According to Sumer and Fredsøe (2006) and Fernandes et al. (2014), N also depends on the range of V_r and Re for a rigid cylinder. In case of a flexible cylinder, it is more KC dominant. The local response at a point is influenced by the response from nearby points.

2.3 Semi-empirical VIV Prediction Method

Standard numerical tools for the prediction of VIV use empirical hydrodynamic force models in combination with finite element method for the structure. VIVANA is such a program used for the prediction of VIV of slender marine structures subjected to a current flow. In VIVANA, the concurrent or space sharing assumption is followed in which all the possible response frequencies are allocated various sections of the structure (MARINTEK, 2016). Each response frequency will have its own zone where it is excited due to the vortex shedding at that zone. This zone is defined based on the dimensionless parameter called non-dimensional frequency, which is defined as:

$$\hat{f}_i(z) = \frac{f_{osc,i}D(z)}{U(z)} \quad (2.9)$$

where $f_{osc,i}$ is the response frequency.

Figure 2.6 explains the allocation of the excitation zones along the length of the structure subjected to a shear current flow.

It is to be noted that an interval of 0.125-0.3 for \hat{f} is used to define the excitation zones. This interval is based on the findings from the experiments conducted on rigid cylinders by Gopalkrishnan (1993). There may be cases of overlap of many response frequencies at a certain point on the structure. In such a case, VIVANA uses an excitation parameter based on energy considerations to prioritize among the overlapping frequencies. This parameter is defined as (MARINTEK, 2016),

$$E_i = \int_{L_{e,i}} U^3(z) D^2(z) \left(\frac{A}{D} \right)_{C_e=0} ds \quad (2.10)$$

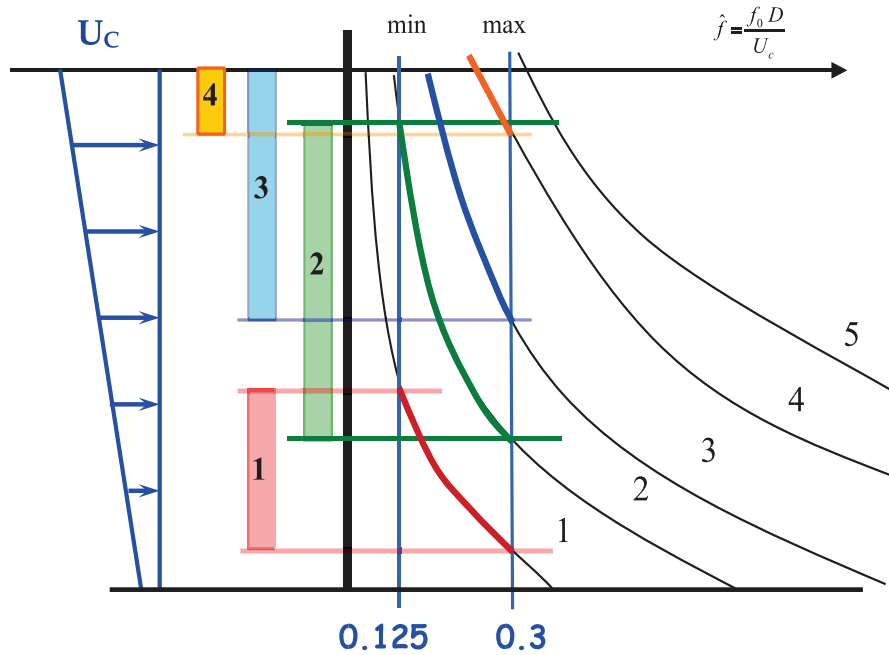


Figure 2.6 Excitation zones along the structure exposed to a shear current (MARINTEK, 2016)

where $L_{e,i}$ is the length of the excitation zone and $\left(\frac{\hat{A}}{D}\right)_{C_e=0}$ is the non-dimensional amplitude where the excitation coefficient shifts from positive to negative value.

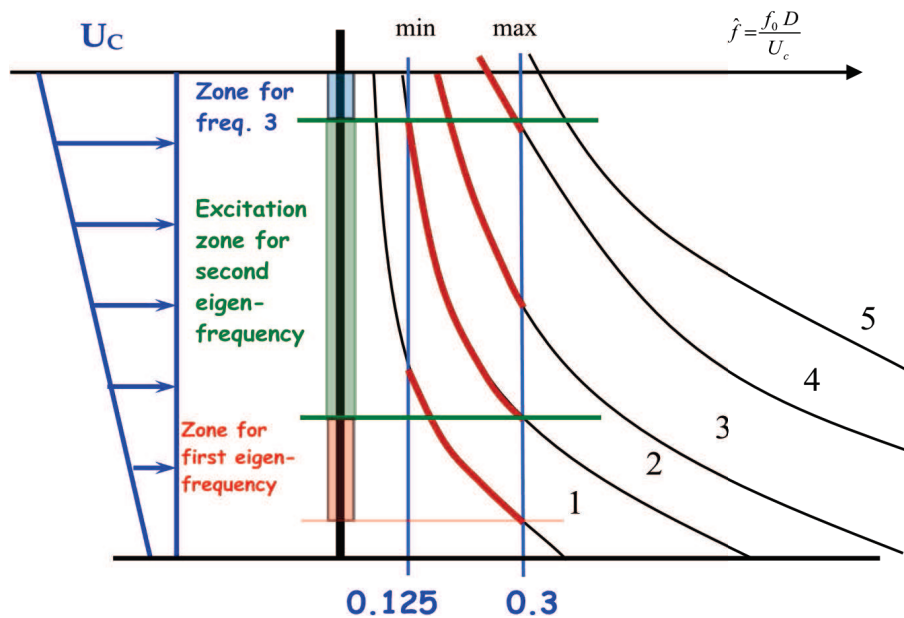


Figure 2.7 Excitation zones along the structure without overlapping frequencies (MARINTEK, 2016)

Finally, VIVANA allocates a unique zone for each response frequency candidate as shown in Figure 2.7. The final response of the structure will be considering all the excitation frequencies along the structure.

Once the VIV frequency is obtained and dominant mode identified, then the response of the structure is evaluated using the built-in hydrodynamic force model of VIVANA.

Chapter 3

Empirical Model for Prediction of Vessel Motion-induced VIV

3.1 Introduction

The vessel motion-induced VIV was first reported in STRIDE, a Joint Industry Project focused on compliant risers (Willis and Thethi, 1999). This was further studied by Gonzalez (2001), Cunff et al. (2005) and Rateiro et al. (2013). Many studies were later conducted using model tests to study the VIV of a free-hanging riser under oscillatory motion. Kwon et al. (2015) conducted experiments on a riser model under oscillatory motion for KC numbers as low as 2.24. Wang et al. (2016a) did similar study on an 8 m long free-hanging riser subjected to pure vessel motion. The equivalent current velocity, effect of KC number and VIV responses were investigated. The CF VIV was observed for a KC number as low as 12.

The effect of low KC numbers on VIV was further studied by Vedeld et al. (2016) for free-span pipelines under waves. At low KC numbers ($KC < 40$), the oscillations are no longer governed by the dimensionless parameters like reduced velocity, but by the ratio N of dominating frequency of the lift force f_L (or dominating response frequency f_{resp}) and the wave frequency

f_w (or the frequency of imposed motion f_{im}), i.e.,

$$N = \frac{f_L}{f_w} = \frac{f_{resp}}{f_{im}} \quad (3.1)$$

The values of N for various KC number ranges are found through experiments by Williamson (1985). It was observed that the value of N increases step-wise with KC number. N is found to increase by 1 with an increase of 8 in KC number. Table 3.1 shows values of N for various KC regimes.

Table 3.1 Value of the ratio N for various KC regimes (Williamson, 1985)

KC number range	N
7<KC<15	2
15<KC<24	3
24<KC<32	4
32<KC<40	5

Similar observations were made by Wang et al. (2016c) when they conducted a model test on a free-hanging Water Intake Riser (WIR) under vessel motions. The frequencies observed during this study are presented in Table 3.2. At low KC numbers, the observed dominant response frequency does not match with the shedding frequency estimated from Strouhal relation using $St=0.2$, but follows an integral relationship with the frequency of motion.

Table 3.2 Frequency information from experiment (Wang et al., 2016c)

Case No.	KC_{top}	Frequency of motion f_{im} (Hz)	Dominant response frequency f_{resp} (Hz)	N	Estimated shedding frequency f_{stmax} (Hz)
1	25.5	0.14	0.28	2	0.5
2	22.5	0.21	0.42	2	0.66
3	9.9	0.32	0.32	1	0.44
4	5.33	0.42	0.42	1	0.31
5	2.28	0.63	0.63	1	0.2

In this chapter, an empirical model to predict the vessel motion-induced VIV of a marine riser under low KC numbers using VIVANA software is proposed. Vessel motion can generate

an equivalent oscillatory flow which is experienced by the riser. As mentioned before, the important non-dimensional parameter that govern an oscillatory flow is KC number. For low KC number cases (<40), the response frequency is not in agreement with the shedding frequency estimated from Strouhal relation, but follows an integral relation with the imposed motion frequency.

3.2 Proposed Empirical Prediction Model

3.2.1 Equivalent current profile

Current Profile is the major input for VIV analysis. VIVANA allows a two dimensional current profile, i.e. variation of current velocity with depth, to be given as the input. When considering vessel motion-induced cases, it is necessary to convert the motion of the vessel and the riser into an *equivalent current profile*. Equivalent current is the current that the riser “sees” due to its relative motion in water. The VIV of the riser due to this current is then analysed in VIVANA to get the responses.

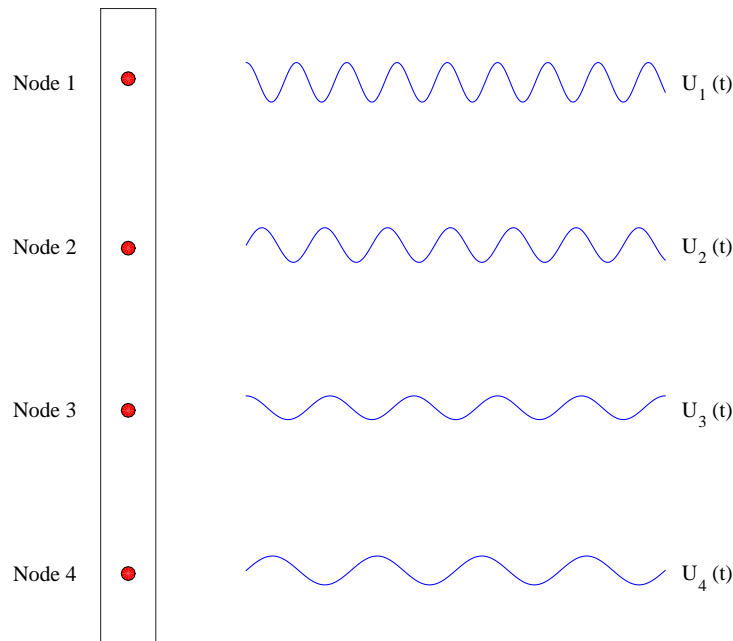


Figure 3.1 Illustration of velocities along the riser

As seen from the illustration in Figure 3.1, the motion of the riser in water over time provides us with velocity time series at each node. An equivalent current profile has to be then derived from these velocities.

Following are the various methods of generating equivalent current profile from the velocity time series:

1. Equivalent Current Profile 1: Here the maximum velocity at each node is taken and a current profile is generated based on it. This is illustrated in Figure 3.2.

$$U_e(z) = \max(U(z, t)) \quad (3.2)$$

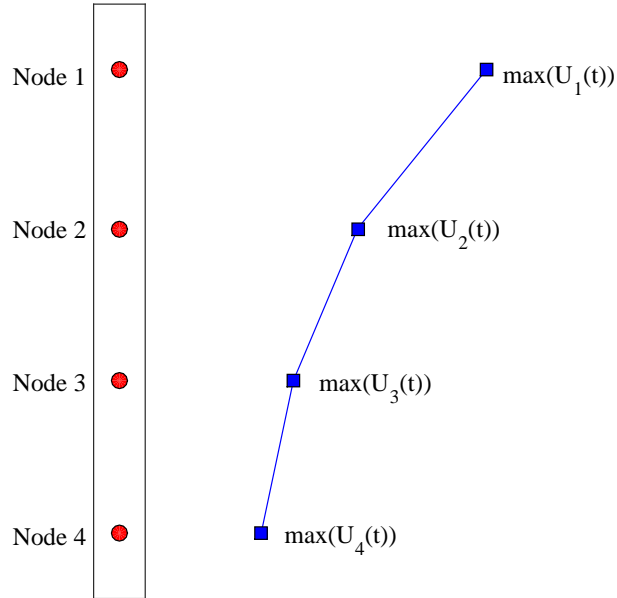


Figure 3.2 Illustration of Equivalent Current Profile 1

2. Equivalent Current Profile 2: Here the standard deviation of the velocity time series is multiplied by $\sqrt{2}$ in order to get the representative maximum at each node. If the velocity time series is harmonic, then this profile will be similar to Equivalent Current Profile 1. This method can be used to estimate the equivalent current profile in case of irregular vessel motions (Wang et al., 2016b). This method is shown in Figure 3.3.

$$U_e(z) = \sqrt{2} \times \sigma_U(z, t) \quad (3.3)$$

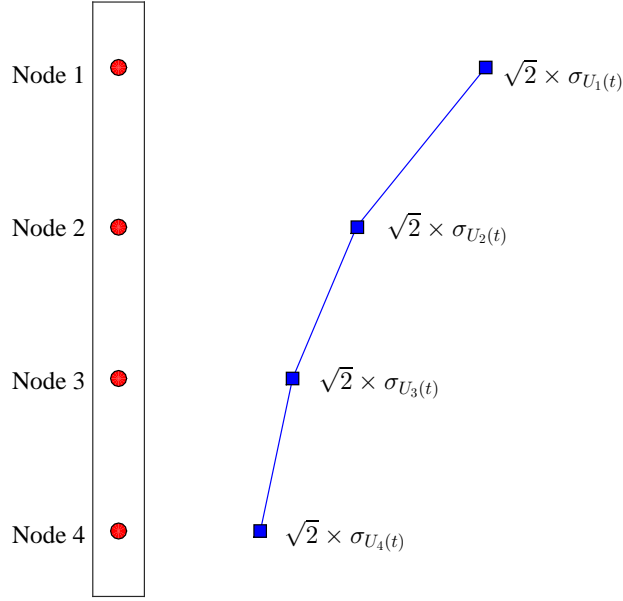


Figure 3.3 Illustration of Equivalent Current Profile 2

3. Equivalent Current Profile 3: A number of velocity snapshots along the length of the riser, each at a particular instant of time, are taken and these snapshots are used as the equivalent current profiles. The VIV responses for each profile is investigated and the final response is taken as the average of all of them.

$$\left(\frac{A}{D}\right)(z) = \frac{1}{N} \sum_{i=1}^N \left(\frac{A}{D}\right)_i(z) \quad (3.4)$$

where N is the no. of velocity snapshots.

Equation 3.4 shows how the response amplitude is averaged. Stress and fatigue damage can be calculated in similar way. The profile is illustrated in Figure 3.4. This method of multiple time windows can be said to be the best approximation of analysis with time varying velocity profiles and has been demonstrated by Wu et al. (2015) when investigating the VIV response of a steel catenary riser under heave induced motion.

The first two methods are mostly suitable for the low KC number cases, where VIV is more consistent in time in terms of response frequency. For large KC number cases, VIV is more time-varying in terms of response frequency, mode and amplitude. Hence, use of multiple time windows and then averaging them as an approximation comes into significance.

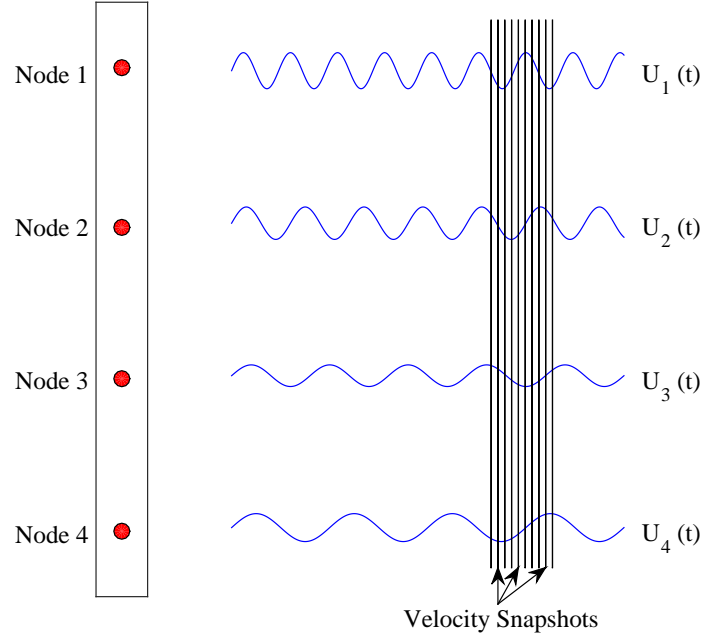


Figure 3.4 Illustration of Equivalent Current Profile 3

3.2.2 Representative KC number

A riser moving in water will have a varying KC number distribution along its length. In most cases, the maximum occurs at the top of the riser due to the vessel motion and the rest of the riser experience a value lower than the one at the top. It is necessary to define a representative KC number that best describes the riser motion. This value will be used to obtain the value of N . Figure 3.5 shows an illustration of a typical KC number distribution. It can be seen that the maximum value is not a representation of the KC distribution. Hence, in this model we define the representative KC number as the midpoint of the distribution (midpoint value between max. and min. of the distribution). This is also illustrated in the figure. It is to be noted that this definition will be necessary only if the variation in KC along the length is large. In case of small variations, the representative KC range can be judged easily from the distribution.

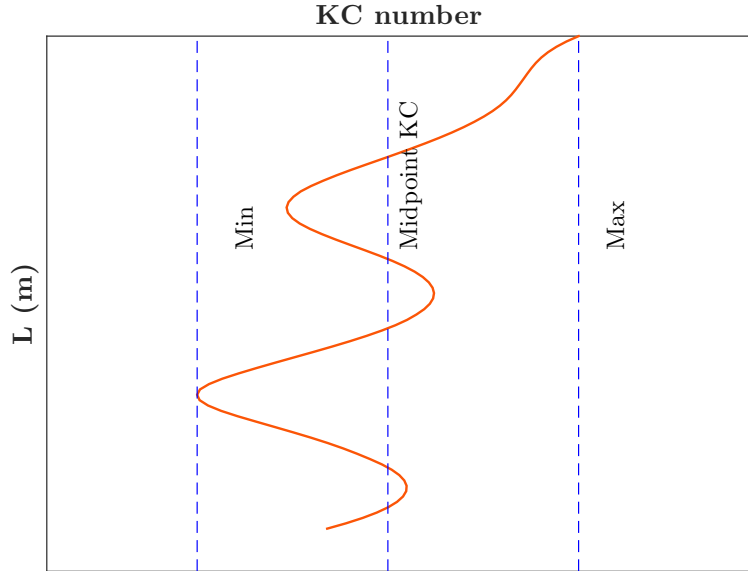


Figure 3.5 Illustration of representative KC number

3.2.3 Response frequency model for low KC number cases

As discussed before, when the KC number is less than 40, the VIV response is no longer governed by the Strouhal relationship. There exists an integral relationship between response frequency and imposed motion frequency (Vedeld et al., 2016). As a result, for the cases with low KC numbers, the value of N from the Table 3.1 is used to estimate the response frequency.

$$f_{resp} = N \times f_{im} \quad (3.5)$$

At lock-in we have $f_v = f_{resp}$

This can be applied to the Strouhal relation to get the equivalent Strouhal number that causes this f_v

$$St^* = \frac{f_v D}{U} \quad (3.6)$$

This equivalent Strouhal number St^* is to be used in VIVANA to predict the VIV. This is based on the empirical model that at low KC numbers we can predict the response frequency based on the imposed motion frequency and the KC number range. Here U is the "dominant" velocity that causes the dominant frequency along the riser. In many cases it is the maximum

velocity, but it can also be the average velocity or any value in between and this depends on the distribution of the equivalent current profile.

A step-by-step approach to predict the vessel motion-induced VIV at low KC numbers is given below. This process is illustrated in Figure 3.6 using a flowchart. The empirical model is also described in Wang et al. (2017).

Step 1: Calculate the riser response based on the vessel motions. Obtain the velocity distribution $U(z, t)$ and the KC number distribution $KC(z)$ along the riser length.

Step 2: Generate the equivalent current profile $U_e(z)$ based on the methods described previously. In case of a harmonic motion, equivalent current profile 1 can be used (refer Equation 3.2). Equivalent current profile 2, proposed by Wang et al. (2016b), is a more generalized method and is suitable to irregular motions as well (refer Equation 3.3).

Step 3: Choose the value of N from Table 3.1 based on the KC number distribution along the riser and calculate f_{resp} from Equation 3.5.

Step 4: An initial equivalent Strouhal number St^* is then calculated from Equation 3.6 using the maximum velocity as U .

Step 5: Using $U_e(z)$ and St^* as inputs, the dominant response frequency, f_{dom} is identified from VIVANA. Further, the value of St^* is updated so that f_{dom} from VIVANA is approx. equal to f_{resp} calculated from Step 3.

The methodology used by VIVANA to determine the response frequencies is described in Chapter 2 section 2.3. In our response frequency model, we define the dominant response frequency f_{dom} as the frequency excited along the major length of the riser. The final response will be heavily influenced by this frequency.

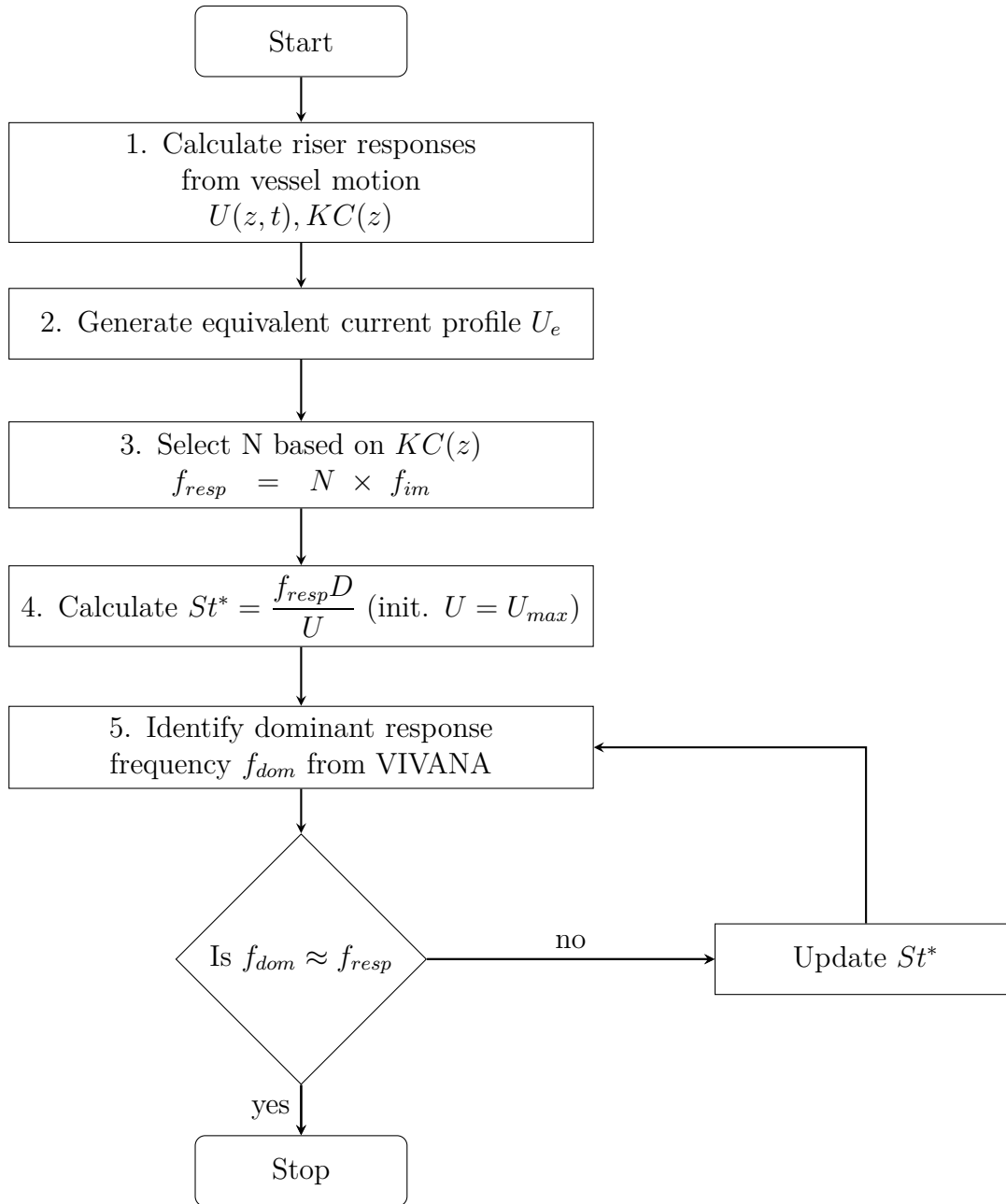


Figure 3.6 Flowchart illustrating the empirical frequency response model

3.2.4 VIV prediction for high KC number cases

In case of high KC numbers, i.e. $KC > 40$, the response frequency is influenced by the Strouhal relation and hence the empirical model need not necessarily be used. However, the N-KC relationship exists for high KC number cases as well and hence the model can be considered

as generic. Whereas in low KC number cases the Strouhal relation would not predict the actual response frequency and the model should be used, in high KC number cases either of them would provide the response. The value of N can be incremented by 1 for every increase of 8 in KC number (Sumer and Fredsøe, 2006). Hence, the Table 3.1 can be expanded to accommodate higher values of KC as well.

3.3 Vibration Amplitudes for Irregular Motions

The vessel motion that causes the VIV can be both regular and irregular. Although in realistic scenarios the motions are irregular, experimental studies mainly concern with regular motions for the purpose of fundamental studies. In case of irregular motions, the amplitudes of vibration from the numerical analysis is to be reduced by 60% (Sumer and Fredsøe, 2006, p. 441-442). According to Sumer and Fredsøe (2006), for cases with irregular waves, "the maximum amplitudes are reduced by about 60% with respect to the values experienced in the case of regular waves". Hence, it is imperative to reduce the amplitude of vibration obtained from VIVANA by 60% while considering irregular motions.

Chapter 4

Empirical Model Validation: Against Model Test Results

4.1 Introduction

An empirical model to predict the VIV due to vessel motion was described in the previous chapter. In order to validate the model, a validation study is conducted. Two experimental models of free-hanging risers under vessel motions are validated here. The experimental setups are modelled in RIFLEX and the VIV is analysed using VIVANA. The main target of the validation is to recreate the riser model and be able to predict the response frequency with good accuracy using the proposed empirical model.

4.2 Methodology

The riser configuration is modelled in RIFLEX based on the riser properties. A modal analysis of the riser is then conducted. The natural frequencies of the riser in still water and the mode shapes are obtained. The comparison of the natural frequencies from the modal analysis and the experimental results is a good way to check whether the modelled configuration is similar to the actual test riser.

The riser is then subjected to regular harmonic vessel motions of the form $x = A\sin\omega t$, where A is the amplitude of the motion and ω is the frequency in rad/s.

The dynamic behavior of the riser under the vessel motion is analyzed over a period of time (preferably $20 \times$ period of motion) to obtain the steady state responses. These responses are used to compute the velocities at each node of the riser. Once the velocities are known, equivalent current profile is generated. The KC number is then calculated from Equation 2.7 and the distribution along the riser is obtained. The maximum amplitude at each node is used in the equation to calculate the KC number. The value of N is chosen from Table 3.1 based on the KC range. Finally, from Equation 3.1 f_{resp} is estimated and equivalent Strouhal number St^* is calculated. This, along with equivalent current profile, is the input for VIVANA analysis.

Two validation studies are performed using the data from the model tests of a free-hanging riser under vessel motion conducted by Wang et al. (2016c) and Wang et al. (2016a) respectively. These are simpler small scale models of a free-hanging riser and are subjected to simple harmonic vessel motions.

4.3 Validation Based on Water Intake Riser Model Test

This study is based on the results from the experiment conducted by Wang et al. (2016c). The aim of the experiment was to study the dynamic behaviour of a WIR prototype under vessel motion. A scaled model of the riser, made of HDPE (High Density Polyethylene), was tested in an ocean basin and the top of the riser was excited with various harmonic motions. The dimensions and properties of the model riser are given in Table 4.1.

The main measured parameter in the experiment is the strain values measured at 16 points along the riser. 4 FBG (Fiber Brag Grating) strain sensors were placed around the cross-section at each measuring point (Wang et al., 2016c). The riser model was subjected to motions of various amplitudes and time periods of which one is selected for the validation

Table 4.1 Properties of model riser (Wang et al., 2016c)

Item	Value	Unit
Length	35.66	m
Outer diameter	0.165	m
Inner diameter	0.15	m
Cross-sectional area, A	0.0037	m ²
Modulus of elasticity, E	8.9×10^8	N/m ²
Bending stiffness, EI	12022	Nm ²
Tensioning stiffness, EA	3.3×10^6	N
Mass/unit length in air	3.61	kg/m
Mass of buffer in air	13.53	kg

study. The amplitude and time period of the oscillation are summarized in Table 4.2.

Table 4.2 Riser motions (Wang et al., 2016c)

Amp (m)	T (s)	f (Hz)	KC_{top}
0.67	7.13	0.14	25.5

4.3.1 Results and discussion

The eigen frequencies of the riser in still water are calculated based on the riser properties. The eigen frequencies for the first 10 modes are shown in Figure 4.1. The normalized mode shapes for the first 5 modes are presented in Figure 4.2.

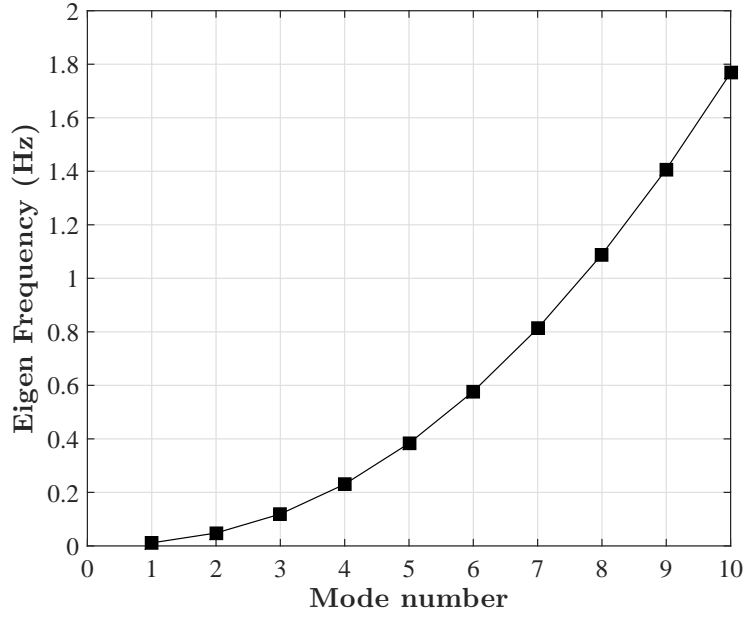


Figure 4.1 Eigen modes and Eigen frequencies of the WIR model

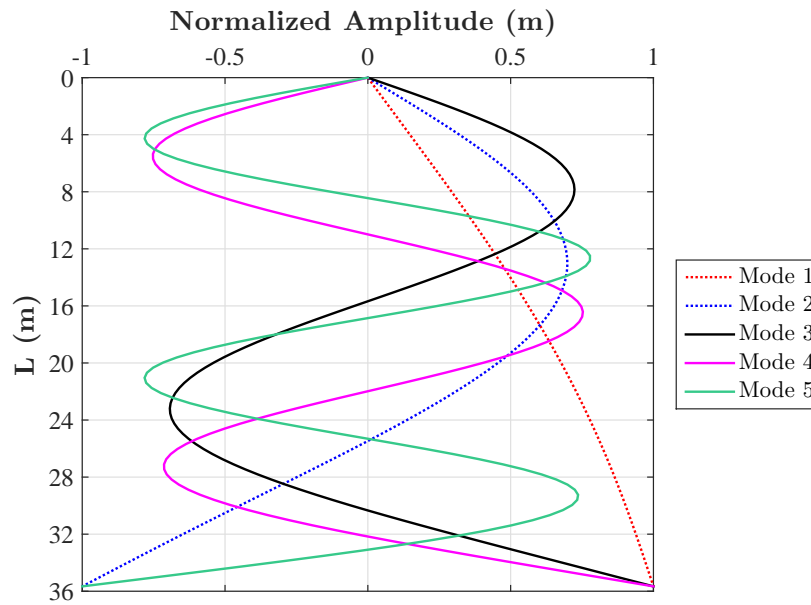


Figure 4.2 Normalized mode shapes for the WIR model

The equivalent current profile generated for the case is shown in Figure 4.3. In this case Equation 3.3 is used to obtain the equivalent current profile.

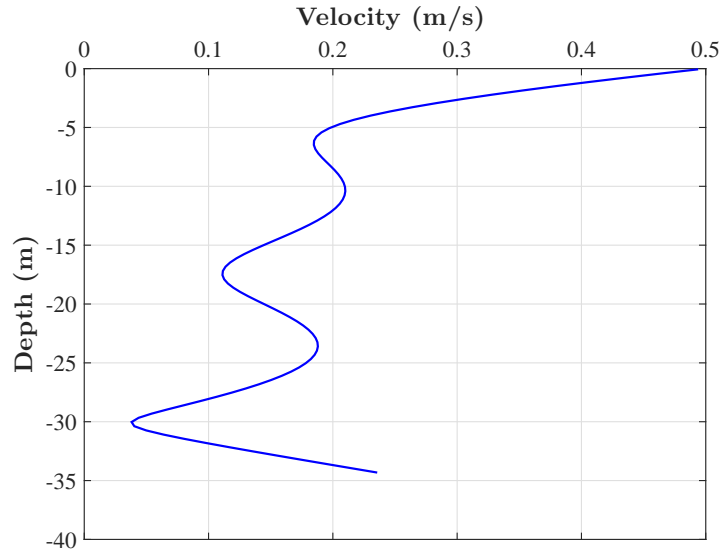


Figure 4.3 Equivalent current profile for WIR

The KC number distribution is presented in Figure 4.4. The maximum value of KC occurs at the top part of the riser and the major portion of the riser experience a much lower KC number. The representative KC number which best describes the KC distribution is found to be in the range of 7-15. According to Sumer and Fredsøe (2006), in this case the integral ratio N of response frequency and imposed frequency of the riser is to be equal to 2, i.e., the dominant response frequency expected for the riser is twice the frequency of top motion.

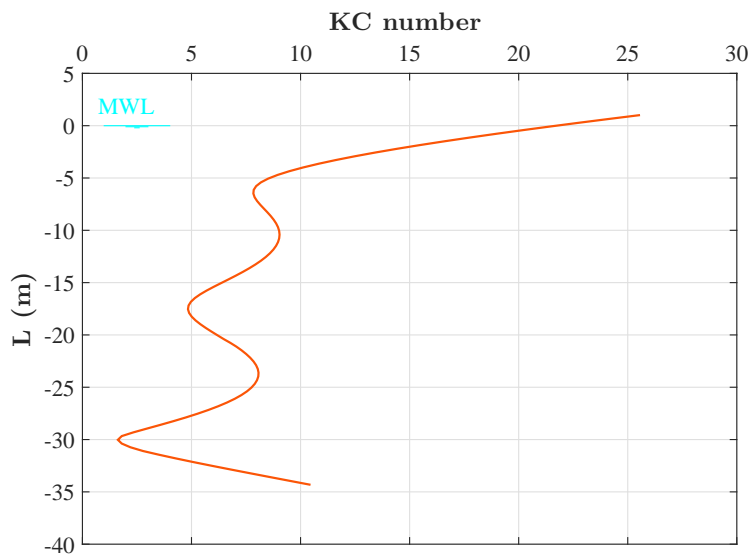


Figure 4.4 KC number distribution for WIR

As mentioned in the previous chapter, the maximum velocity is used to calculate an initial St^* . This is used in VIVANA to analyze the VIV. The dominant response frequency from the VIVANA is then used to update the value of St^* . In this case, the value of St^* which gives $f_{dom} = f_{resp}$ is equal to 0.36.

Figure 4.5 shows the excitation frequencies along the length of the riser obtained from VIVANA analysis. It can be seen that the dominant response frequency along the riser is 0.28 Hz, which is twice the frequency of the imposed motion (0.14 Hz). The response plots from the experiment also point to a frequency of the same value and this corresponds to 4th mode of the riser (refer Figure 4.6).

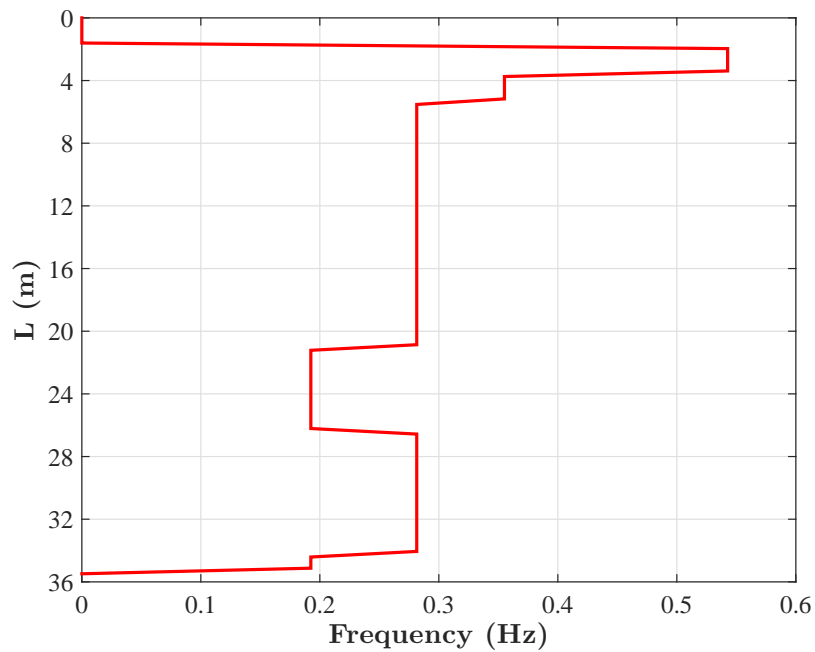


Figure 4.5 Excitation frequencies for WIR

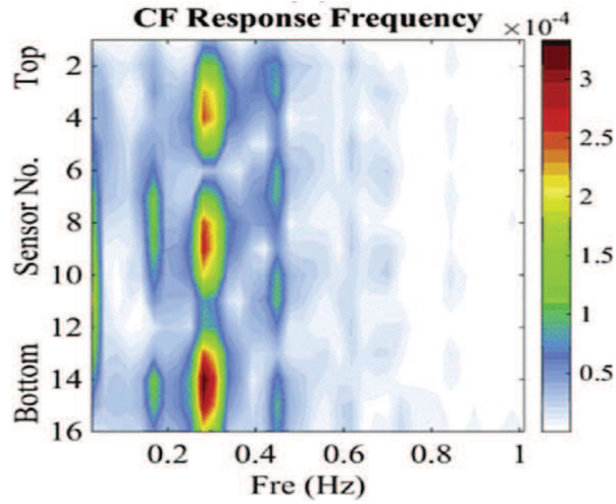


Figure 4.6 Response frequency along the riser from experiment for WIR (Wang et al., 2016c)

The RMS value of strain measurements from the experiment is compared with that obtained from the analysis and is presented in Figure 4.7. It can be seen that the mode from the analysis agrees well with the mode from the experiments. The maximum strain value obtained is slightly higher and hence is a conservative prediction.

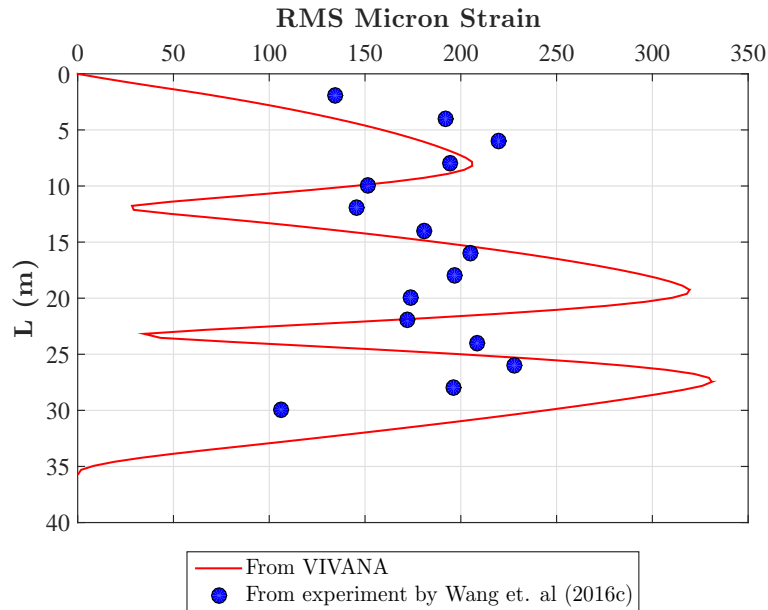


Figure 4.7 Comparison of RMS strain values for WIR

The RMS A/D is compared in Figure 4.8. The mode shape agrees well with the experimental results. The values are in good agreement for the one-third of the riser.

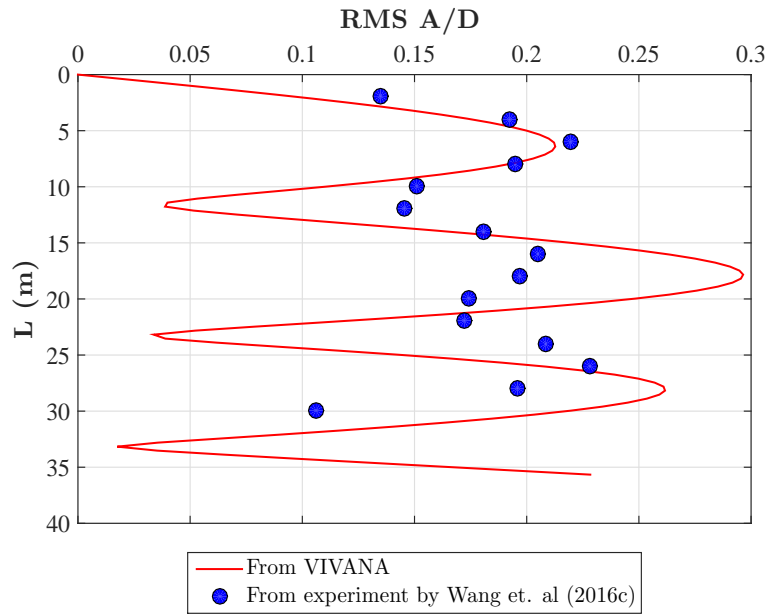


Figure 4.8 Comparison of RMS A/D for WIR

The difference in the strain values between analysis and measurements may be due to the difference in relative structural damping of the actual model and the numerical model. Since the data was unavailable, 5% relative structural damping was assumed based on the findings by Munson et al. (2012) for HDPE (High Density Polyethylene) pipe.

4.4 Validation Based on Free-Hanging Riser Model Test

The empirical model is validated based on the results from the experiments of Wang et al. (2016a). A model test of an 8 m long free-hanging riser was conducted for pure vessel motions under different ranges of KC numbers. The properties of the riser are summarized in Table 4.3.

It is to be noted that here the initial 1.38 m of the riser is kept above the water level. In this experiment also, the responses were measured using the strain gauges. A total of 64 FBG

Table 4.3 Properties of model riser (Wang et al., 2016a)

Item	Value	Unit
Length	8	m
Outer diameter	0.029	m
Inner diameter	0.019	m
Cross-sectional area, A	0.00037	m ²
Modulus of elasticity, E	1.42×10^9	N/m ²
Bending stiffness, EI	50.8	Nm ²
Tensioning stiffness, EA	5.3×10^5	N
Mass/unit length in air	1.61	kg/m
Mass of buffer in air	9	kg

sensors were used in this case. There were 16 measuring points along the riser and at each point 4 sensors were placed symmetrically along the cross-section (Wang et al., 2016a). The amplitudes and periods of riser motions selected for the validation are given in Table 4.4.

Table 4.4 Riser motions (Wang et al., 2016a)

Case	Amp (m)	T (s)	f (Hz)	KC_{top}
1	0.051	1.1	0.91	11
2	0.28	5.52	0.18	61

4.4.1 Results and discussion

The results from the validation study are presented below. The eigen frequencies of the riser in still water for the first 10 modes are presented in Figure 4.9. Figure 4.10 shows the normalized mode shapes for the first 5 modes.

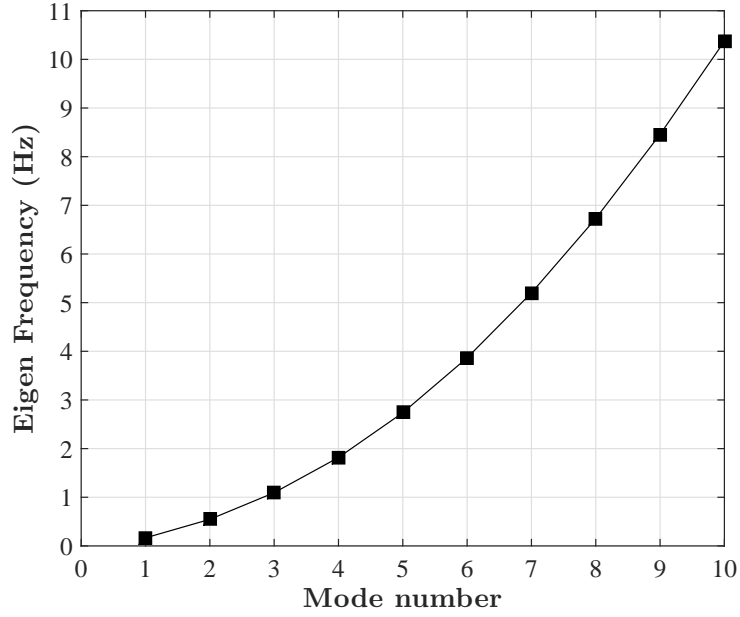


Figure 4.9 Eigen modes and Eigen frequencies of the free hanging riser model

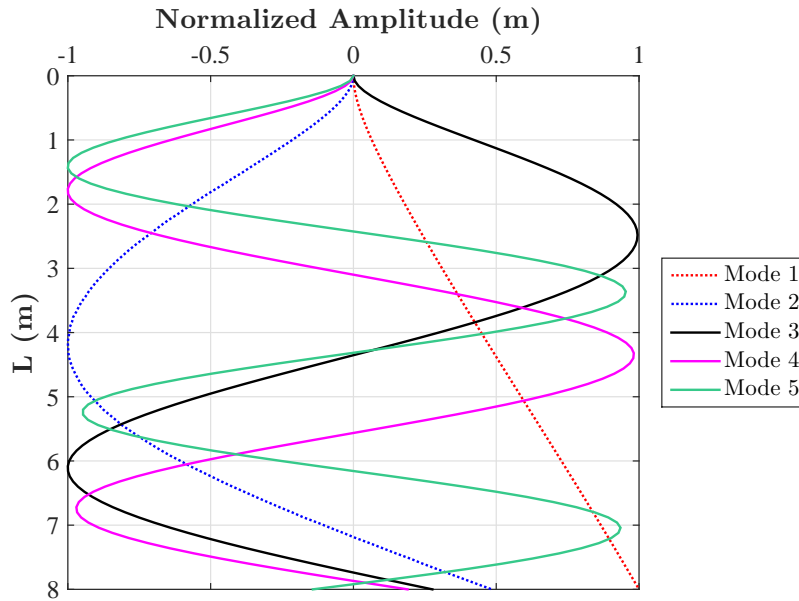


Figure 4.10 Normalized mode shapes for the free hanging riser model

4.4.1.1 Case 1

The top KC number for this case is 11. The equivalent current profile is as shown in Figure 4.11. It can be seen that the maximum velocity occurs not at the top, but at a point 4.5 m from the top.

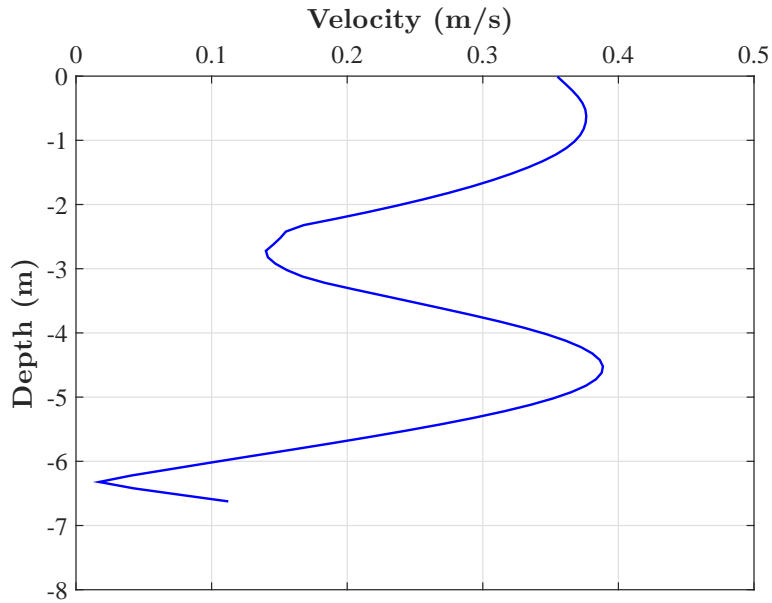


Figure 4.11 Equivalent current profile for Case 1

A look at the KC number distribution from Figure 4.12 confirms that the major part of the riser experiences a KC higher than 8. Hence, we can choose $N=2$ for this case, i.e., the dominant response is expected to be at twice the frequency of imposed motion.

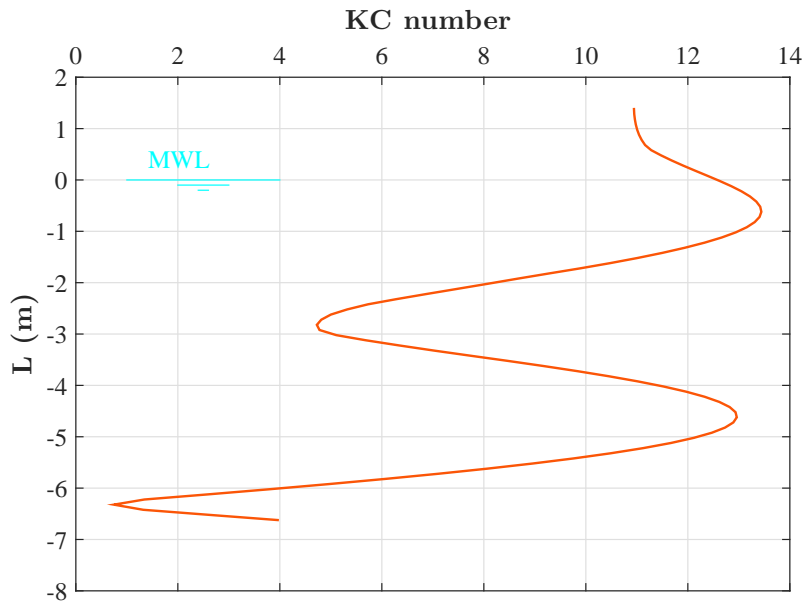


Figure 4.12 KC number distribution for Case1

Figure 4.13 shows the frequency plot of the CF response from the experiment. It can be seen that the responses are with a frequency of 1.8 Hz, which is twice that of the frequency

of imposed motion. Figure 4.14 shows the excitation frequencies from the VIVANA analysis

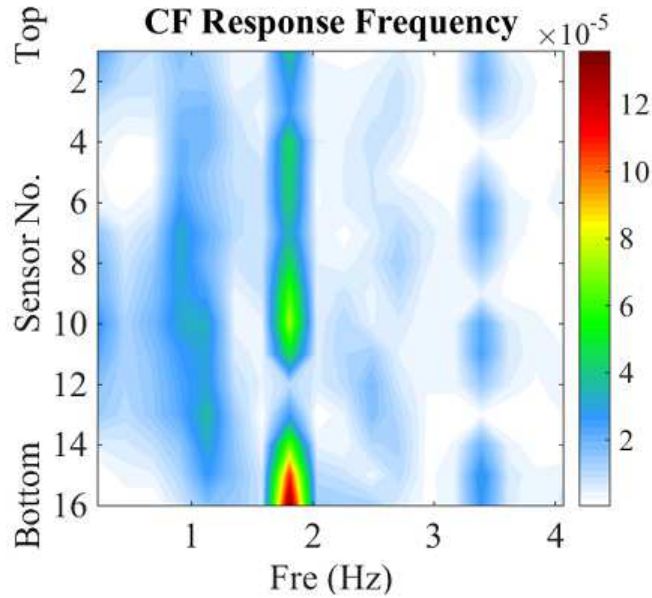


Figure 4.13 Response freq. along riser for Case 1 from experiment (Wang et al., 2016a)

using the proposed empirical model. The value of St^* used here is 0.174. The dominant response frequency from VIVANA is also 1.8 Hz and it is good agreement with the response frequency from the experiment. This frequency corresponds to the 4th eigen mode of the riser.

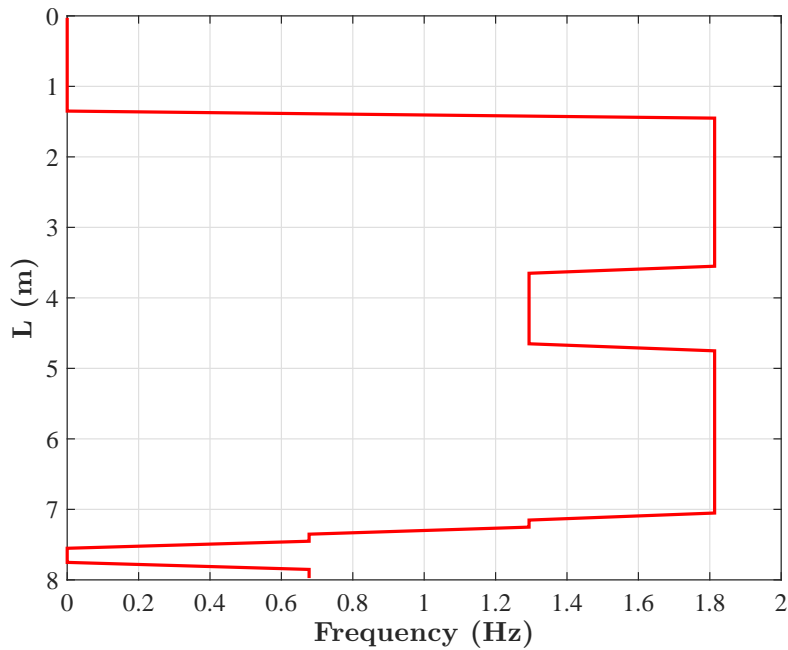


Figure 4.14 Excitation frequencies from VIVANA for Case 1

Figure 4.15 shows the strains obtained from the analysis. This can be compared with the maximum strain values from the time varying strain responses from the experiment presented in Figure 4.16.

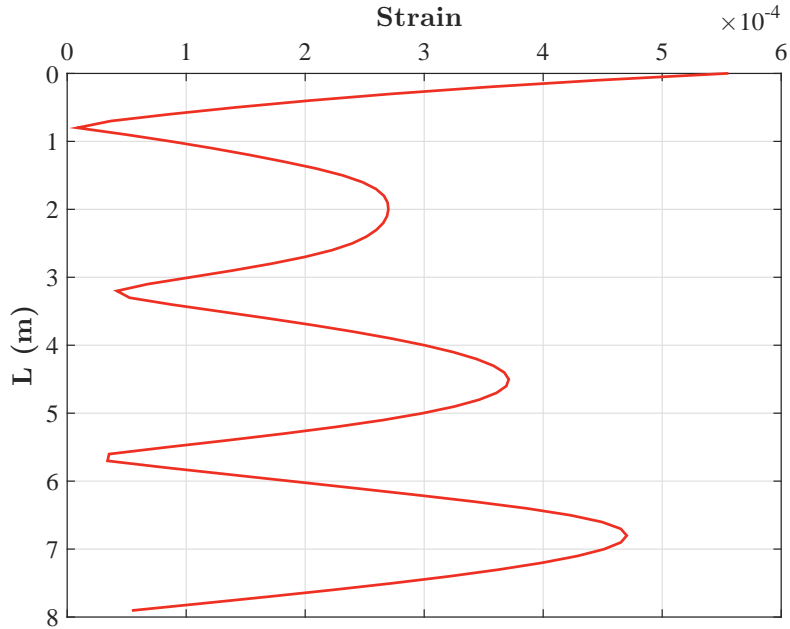


Figure 4.15 Strain values for Case 1

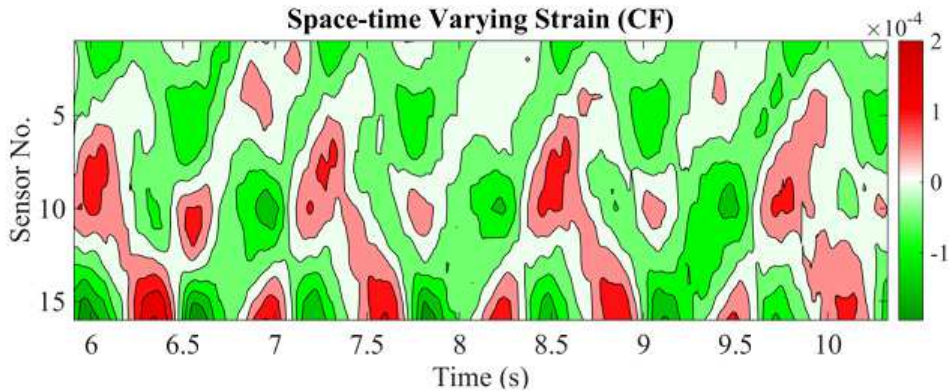


Figure 4.16 Time varying strain from experiment for Case 1 (Wang et al., 2016a)

It can be seen that the maximum value of strain at the midpoint of the riser (Sensor no. 10) is around 0.5×10^{-4} to 1×10^{-4} . The value obtained from analysis is higher than the one from experiments, but it is evident that the frequency and the mode of vibration matches well with experiment data.

4.4.1.2 Case 2

The top KC number in this case is 61. Even though the dominant response frequency is not necessarily influenced by the imposed motion as in the case of low KC numbers, the proposed empirical model can still be applied to the case. The equivalent current profile is illustrated in Figure 4.17.

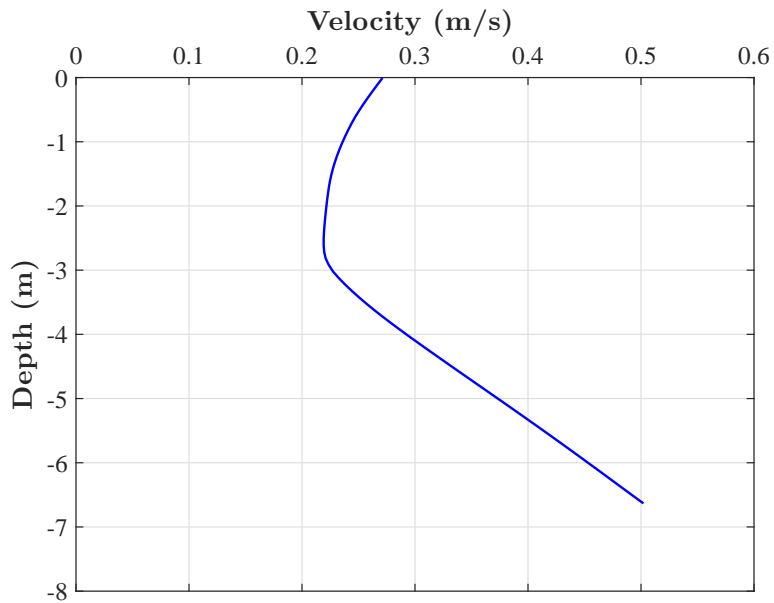


Figure 4.17 Equivalent current profile for Case 2

The KC number distribution is shown in Figure 4.18. It is evident that the value of KC changes drastically along the length of the riser. In order to predict the response frequency using the empirical model, it is important to define a particular representative KC number that best describes the case. This KC is in turn used to select the value of N . In the present case, we use the method described in section 3.2.2 to describe the representative KC. Hence, in this case the representative KC number is taken as the midpoint of the distribution and is equal to 78. It is to be noted that the same applies to Case 1 as well, but since the variation in values is not as large as in this case, we could easily judge the representative KC.

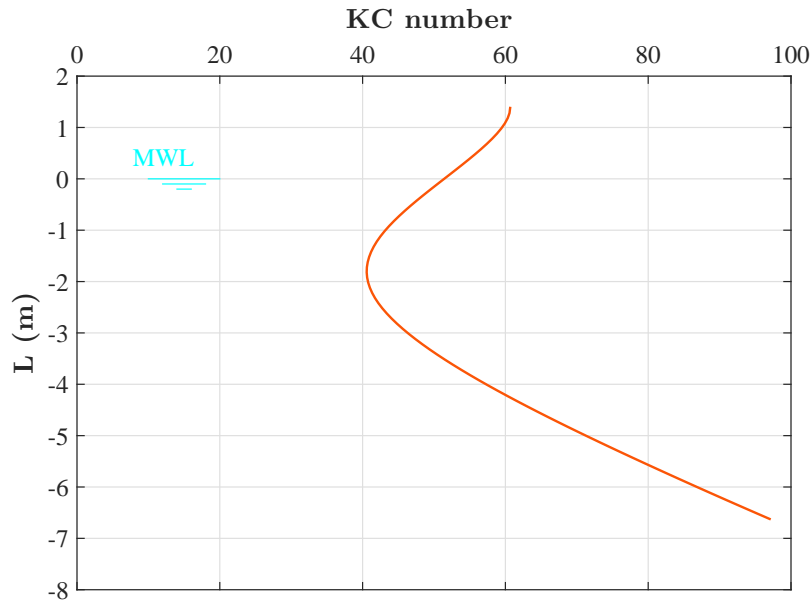


Figure 4.18 KC number distribution for Case 2

According to Sumer and Fredsøe (2006), the value of N is increased by 1 with an increase of 8 in KC number. Therefore, this case should belong to a KC regime with $N=10$. Figure 4.19 shows the frequency of CF response from the experiment. The dominant response is with a frequency of about 1.8 Hz. Here, the frequency of imposed motion is 0.18 Hz, hence as per the empirical model the response frequency should be 1.8 Hz.

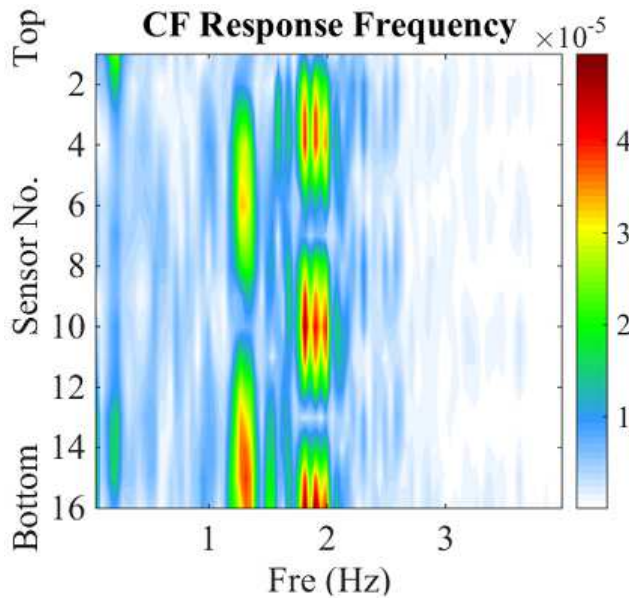


Figure 4.19 Response freq. along riser for Case 2 from experiment (Wang et al., 2016a)

Figure 4.20 shows the excitation frequencies along the riser from VIVANA analysis. It can be seen that the frequency predicted using the model agrees well with that from the experiment. Also, the value of St^* used here is 0.18. This value of St^* is similar to the actual value of St for this case based on the Re value and surface roughness. Hence, even if the proposed model is not followed here, we could get similar response frequency for this case. This proves our theory that for higher KC numbers, the proposed model will still be applicable even though not necessarily required.

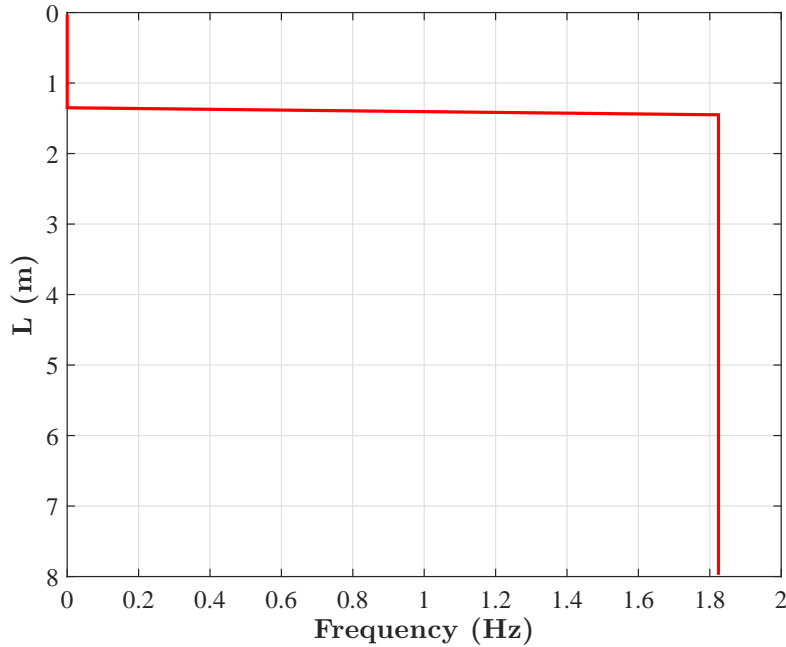


Figure 4.20 Excitation frequencies from VIVANA for Case 2

From Figure 4.19, it can be seen that more than one mode participate in the response in this case. One equivalent current profile will not be able to predict all the responses. As such in this case the multiple time window profile proposed by Wu et al. (2015) (Equivalent Current Profile 3) comes into significance.

The maximum strains along the riser from analysis is plotted in Figure 4.21. Figure 4.22 shows the time varying strains from the experiment. The maximum value of strain from the experimental data is in the range of 1×10^{-4} to 2×10^{-4} . The values obtained from analysis agree well in this regard.

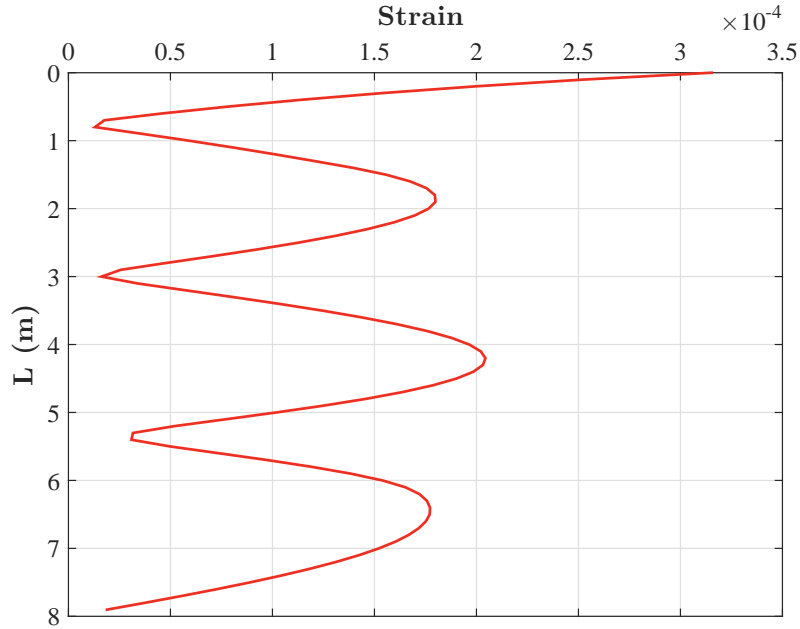


Figure 4.21 Strain values for Case 2

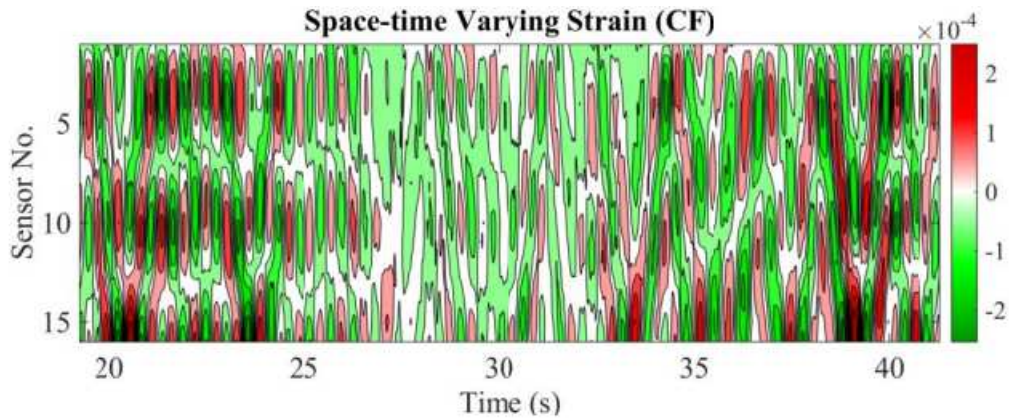


Figure 4.22 Time varying strain from experiment for Case 2 (Wang et al., 2016a)

4.5 Discussion

The model validation studies provided good results considering the various constraints like correctness of the input data, experimental and modelling errors, etc. The main aim of validation studies was to prove the feasibility and accuracy of the proposed response frequency prediction model for vessel motion-induced VIV at low KC number cases. The model was able to successfully predict the dominant response frequency of all the cases. A case of KC

number higher than 40 was considered and the model could predict the response for that particular case. This also proves that the model is generic in character and can be applied regardless of the KC number range. The model has its significance in lower KC number range since the Strouhal relation, using constant Strouhal number as 0.18, fails to predict the VIV response in that range.

Chapter 5

Empirical Model Validation: Against Full-scale Measurements

5.1 Introduction

In the previous chapter, model validation using small scale model test data was discussed. Before extending the application of the empirical model to an ultra-long riser, it is necessary to investigate how the model works in case of an actual long riser. In this chapter, the empirical model is applied to an actual full-scale drilling riser and the results are compared with the field measurements. These measurements of the full-scale drilling riser were performed by British Petroleum during a drilling campaign in the Gulf of Mexico between 13th April 2007 and 11th July 2007. The dataset is donated to the VIV Data Repository hosted by Center for Ocean Engineering, MIT for the purpose of calibration and benchmarking of VIV softwares (BP and 2H Offshore, 2008) and is publicly accessible. The main parameter in the data set is the accelerations measured by accelerometers at various points along the length of the riser. One of the main issues pertaining to the application of the empirical model to the riser is the identification of the vessel motion-induced VIV from the acceleration measurements. Absence of any details regarding the vessel or the wave data makes this task even more difficult. Nevertheless, a conscious effort has been made to identify vessel motion-induced

VIV from available data and apply the empirical model to the riser. As has been the case in the previous validation study, the goal is not to obtain the exact amplitudes of vibration or stresses, but to predict the response frequency and the dominant mode with reasonable accuracy. It is to be noted that the full-scale measurements corresponds to the cases with irregular vessel motions.

5.2 Full-scale Data Information

The dataset contains the following:

1. Riser configuration, dimensions and riser weight.
2. Tension and mud weight data.
3. Current data at the location.
4. Acceleration data from accelerometers at various points on the riser.

5.2.1 Riser configuration

Two wells were drilled during the drilling period. The configuration of the riser during drilling of well-1 is illustrated in Figure 5.1. The measurement loggers are named as S01, S02, ..., S13 with S01 situated on the drill floor. Their locations are indicated by the red squares in the figure. It can be seen that the majority of the loggers are concentrated towards the lower end of the riser. Such an arrangement is to capture all the expected modes with minimum possible number of loggers. An optimum placement of loggers should capture atleast the quarter wavelength of the lowest mode expected (Natarajan et al., 2006).

The riser material is steel with a density of 7850 kg/m^3 and modulus of elasticity of $2.07 \times 10^{11} \text{ N/m}^2$. The outer diameter is 21 inches.

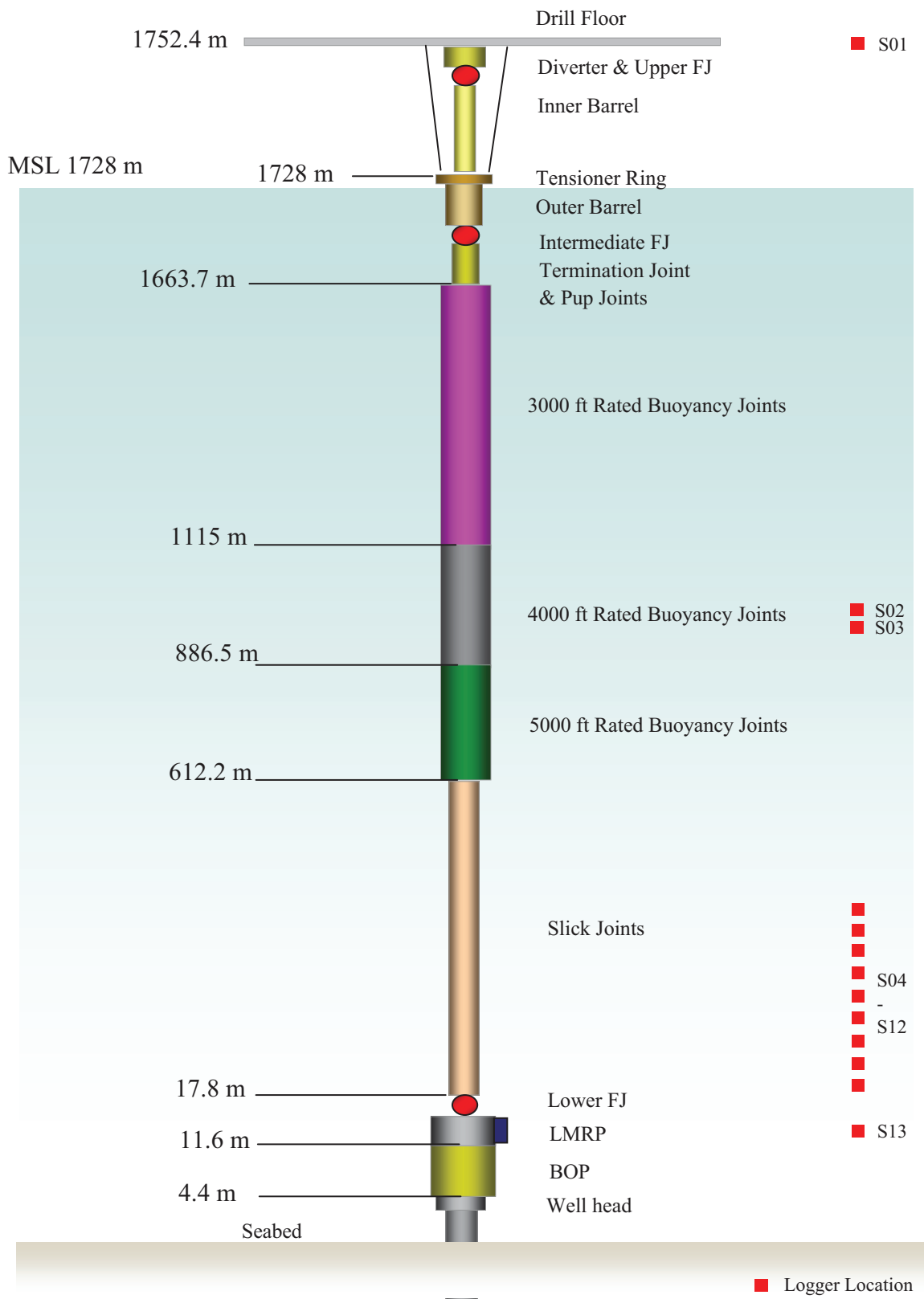


Figure 5.1 Configuration of the drilling riser (BP and 2H Offshore, 2008)

Table 5.1 shows the distances from the drill floor at which the loggers are located on the riser.

Table 5.1 Locations of the loggers

Logger ID	Distance from the drill floor (m)
S01	0
S02	775
S03	798
S04	1436
S05	1458.8
S06	1481.7
S07	1504.5
S08	1550.2
S09	1596
S10	1641.7
S11	1687.4
S12	1733
S13	1739

Figure 5.2 shows the top tension of the riser and the density of mud used during the drilling period.

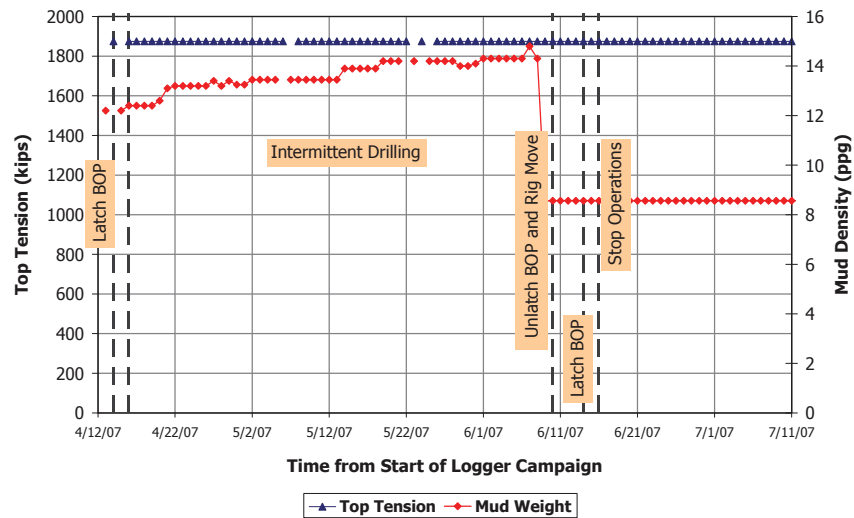


Figure 5.2 Riser tension and mud density (BP and 2H Offshore, 2008)

5.2.2 Environment and current data

The water depth at the location of well-1 is 1728 m and well-2 is 1729 m. The current at the location was measured using three ADCPs (Acoustic Doppler Current Profiler), two of which are mounted on the vessel. A 300 kHz horizontal ADCP measures the current at 36 m below MSL and a downward looking 38 kHz ADCP covers depths from 72 m to 1128 m below MSL. An upward looking 75 kHz ADCP measures current between 26 m and 586 m above the seabed. The current is sampled at every 10 minutes and averaged (BP and 2H Offshore, 2008). A constant density of 1025 kg/m^3 is assumed for the sea water.

5.2.3 Instrumentation

The instrumentation consists of 13 standalone loggers. One of the loggers is located on the drill floor and measures the vessel acceleration. The other loggers are placed at various locations on the riser. The logger contains the sensors, batteries, memory card and all the associated electronics encased within a cylindrical casing (BP and 2H Offshore, 2008). The loggers are then strapped to the structure. Typically, motion sensors in the logger are made of tri-axial accelerometers and tri-planar angular rate sensors (Thethi et al., 2005), but the angular rate sensors are not active in this experiment.

5.2.4 Accelerations and events

The accelerometer measures the acceleration at the location in three axes. The data is measured continuously for a duration of 15 minutes at each 2 hour interval. This limited time of measurement is because of the fact that the loggers have a limited battery life and it has to be conserved for the whole drilling period. The sampling frequency is 10 Hz. Each 15 minute period of measurement is termed as *an event*. There are a total of 1078 events captured during the drilling period. These events are spread over 3 operational cases - (1) drilling of well-1, (2) hang-off and transport and (3) drilling of well-2.

5.2.5 Limitations

Following are some of the known limitations of the measurements:

1. The accelerometers are standalone and exact time synchronization may not be possible.
2. The alignment of logger X and Y axes with the global X and Y axes is not guaranteed.
3. Some of current data are missing due to the unavailability of ADCPs during that period.
4. The accuracy of accelerometers at low frequencies is not guaranteed.
5. Most of the acceleration data are polluted and of poor quality. Poor quality data can provide misleading results. Figure 5.3 shows the time series of acceleration at a logger for a particular event. It can be seen that the acceleration readings appear to be truncated and is not continuous.

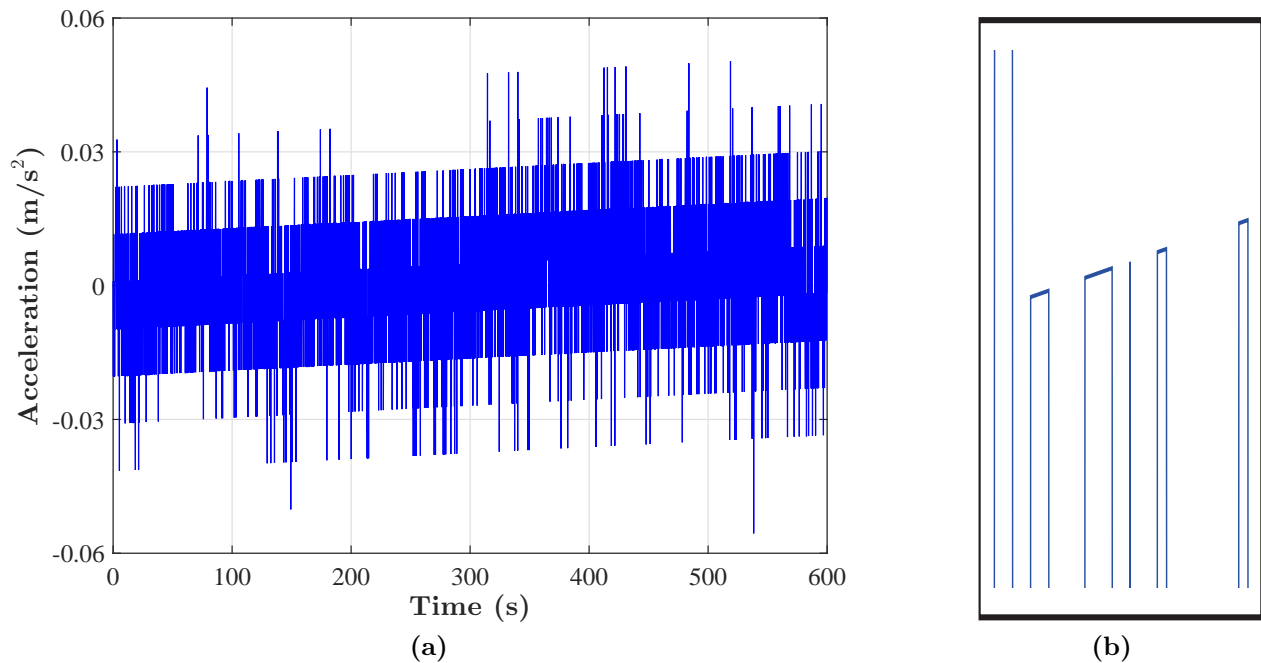


Figure 5.3 (a) Acceleration time series at a particular sensor showing poor quality data (b) Zoomed in picture showing discontinuity in data

One of the reasons for this may be that the accelerometers are of low precision and hence the adjacent readings appear to be the same. In the present analysis, data of poor

quality was identified and discarded. The criterion used here is that cases with similar adjacent readings amounting to more than 15 % of the total readings are classified to be poor quality data.

Figure 5.4 shows an example of the acceleration time series which can be considered as acceptable for the analysis.

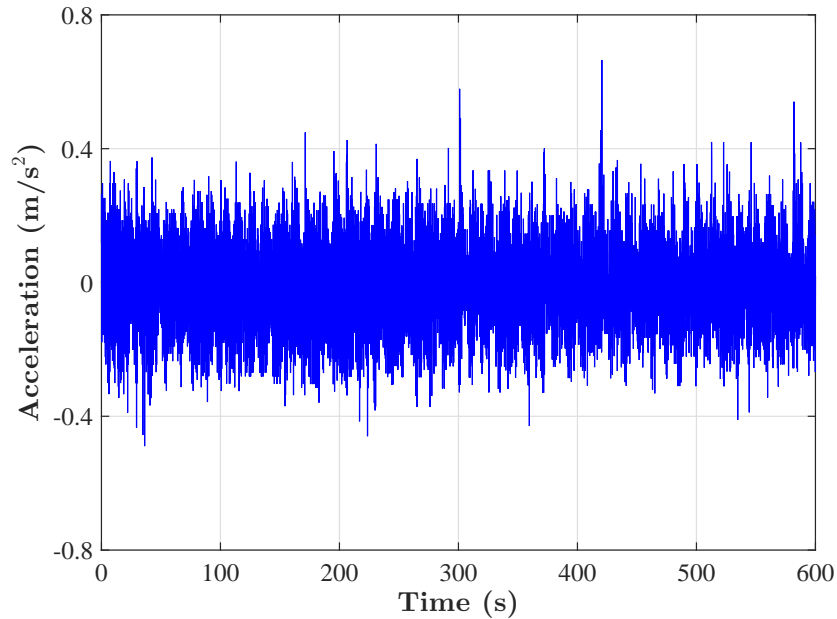


Figure 5.4 Acceptable acceleration time series at a particular sensor

5.3 Data Analysis

The accelerations in X, Y and Z axes are available for all the events during the drilling period. Along with these, the current speed and direction are also available. The main task is to identify current-induced VIV and vessel motion-induced VIV from these data for the various events.

The VIV and the response frequency can be identified by performing a spectral analysis of the accelerations or displacements at each logger location. The peak frequencies of the spectrum, which fall within the VIV frequency range, across all loggers can be identified and correlated. The shedding frequencies based on the current velocity can be calculated and compared with

the response frequencies identified from the spectrum. In case of current-induced VIV, the response frequency is expected to be in agreement with the shedding frequencies calculated from current velocities. In this way we can identify the current-induced VIV from vessel motion-induced VIV. The logger S01 placed on the vessel measures the vessel acceleration. The frequency of the vessel motion can be found by a spectrum analysis at this logger.

The velocities are obtained by the integration of the accelerations. Further integration provides the displacements at various logger locations. Once the velocities along the riser are known, the equivalent current profile can be generated and this can be used for the VIVANA analysis. The empirical model is then applied to the case to predict the response frequency. It should be noted that the vessel motions in this case need not necessarily be limited to low KC numbers. Nevertheless, the empirical model is applied and validated based on the theory that the model holds true for higher KC numbers as well.

The accelerations are passed through a low pass filter to filter out frequencies less than 0.5 Hz, which are of our interest. This will eliminate the vibrations of high frequencies, especially that caused by the drill string. Typically to identify the VIV, it is sufficient to filter out only the frequencies in the VIV range. Since we are also interested in the vessel motion, which can occur at very low frequencies, we have to consider those as well.

A typical acceleration spectrum from one of the loggers located on the riser is presented in Figure 5.5. The spectrum gives a glimpse of the various frequency contributions to the riser response. The vessel motion occur at very low frequencies and can be easily identified from a displacement spectrum. The displacement spectrum gives a very large peak for the vessel motion frequency at all the loggers. This can be correlated with logger S01 which purely measures the vessel acceleration and hence vessel motion frequency can be singled out.

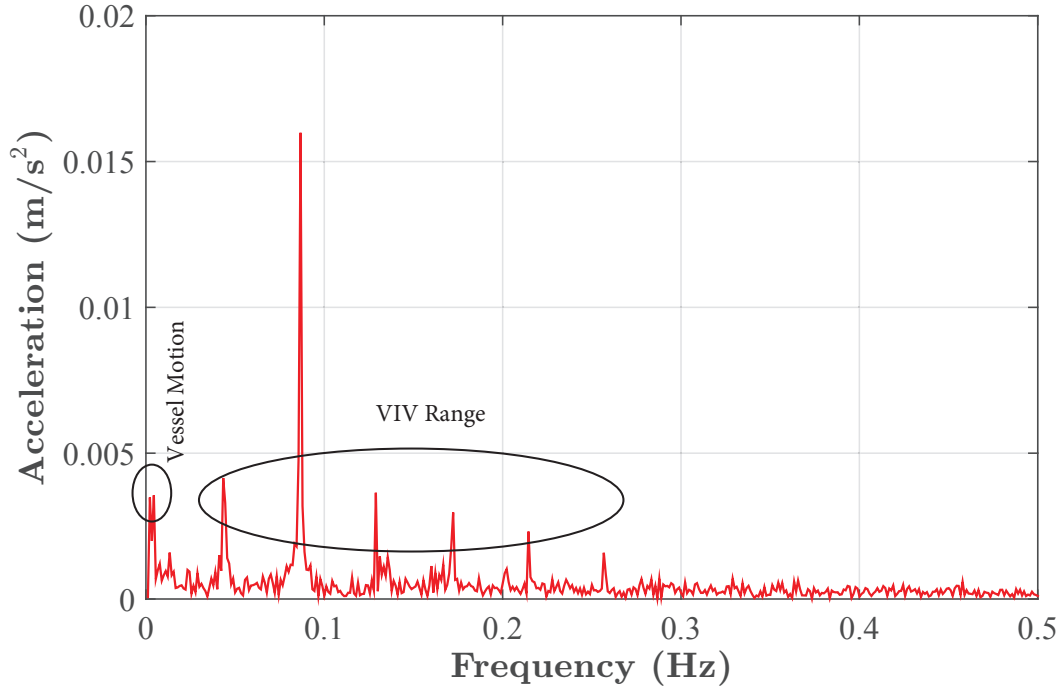


Figure 5.5 An example of acceleration spectrum showing the contributions from various excitation sources

5.4 Methodology

The methodology followed for the numerical analysis is summarized as follows:

- Obtain the velocity time series at each logger location. Generate the equivalent current profile based on the Equation 3.3.
- Obtain the KC number distribution along the riser from the displacements derived at each logger location.
- Choose the appropriate value of N from Table 3.1 based on the KC distribution.
- Estimate f_{resp} from the value of f_{im} and N .
- Calculate initial St^* and perform VIVANA analysis, iterate St^* to obtain $f_{dom} = f_{resp}$

5.5 Results and Discussion

In this section four representative events are identified and analysed. All these four events belong to the operational case of drilling of well-1 and are presented in Table 5.2. The empirical model is validated against the measured responses of the riser. In the validation studies, emphasis is given to the prediction of response frequency. The eigen frequencies for the first 10 modes and the normalized mode shapes for the first 5 modes are presented in Figures 5.6 and 5.7 respectively.

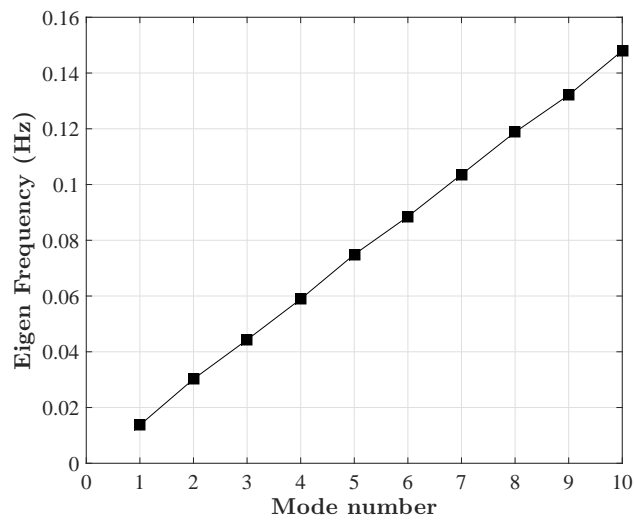


Figure 5.6 Eigen modes and eigen frequencies for the drilling riser

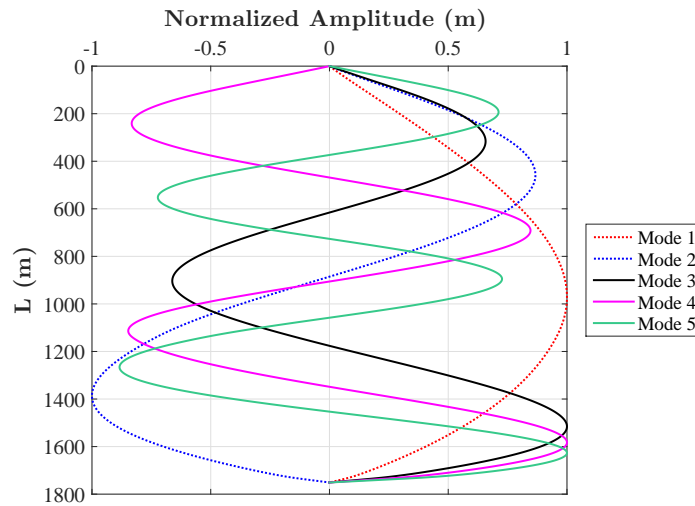


Figure 5.7 Normalized mode shapes for the drilling riser

Table 5.2 Events considered for analysis

Event	Time stamp	Remarks
58	17/04/2007 1800 hrs	Vessel motion-induced VIV dominant
612	02/06/2007 0200 hrs	Vessel motion-induced VIV dominant
413	17/05/2007 0800 hrs	Vessel motion-induced VIV dominant
434	19/05/2007 0200 hrs	Current-induced VIV dominant

5.5.1 Vessel motion-induced VIV dominant cases

5.5.1.1 Event 58

Event 58 corresponds to a very low current velocity case. In Figure 5.8, the ocean current is compared with the equivalent current profile generated based on the velocities derived from the accelerations. It can be seen that the ocean current velocities are very low compared with the velocities from vessel motion. The shedding frequency due to ocean current has a maximum value of 0.043 Hz.

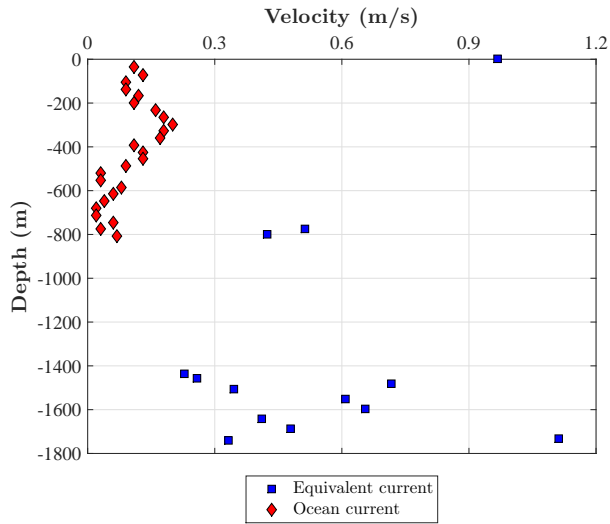


Figure 5.8 Generated equivalent current profile and the ocean current profile (Event 58)

Figure 5.16 and Figure 5.17 represent the spectra of accelerations in X and Y directions respectively across all the 13 loggers. It can be seen that all the loggers except S01 (S01 measures vessel acceleration) have a peak response at a frequency of 0.0866 Hz (highlighted by the blue square). This is identified to be the response frequency of the VIV.

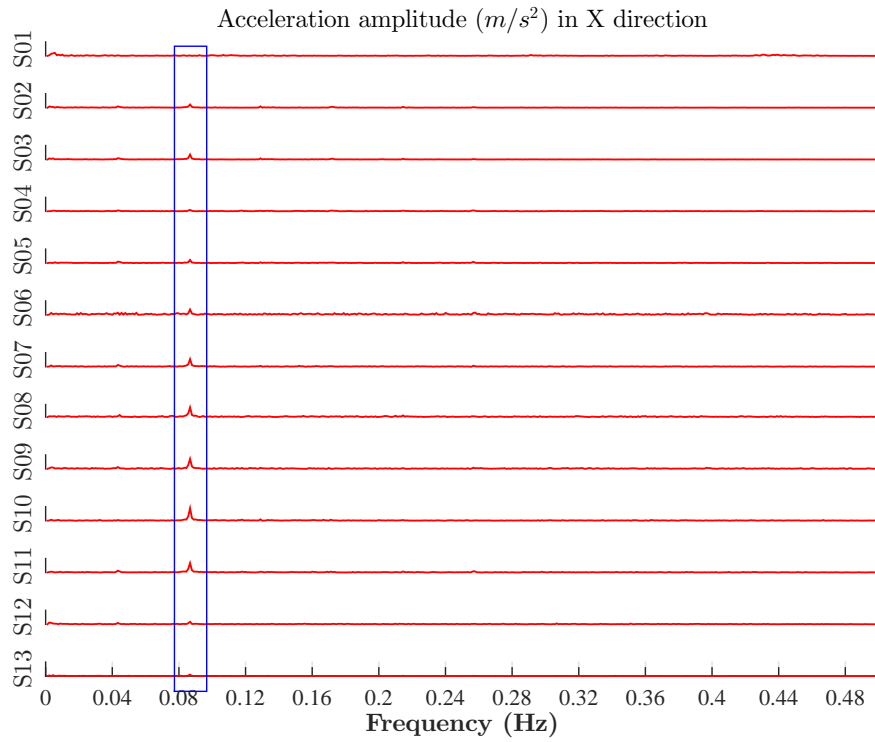


Figure 5.9 Spectra of acceleration in X direction across all loggers (Event 58)

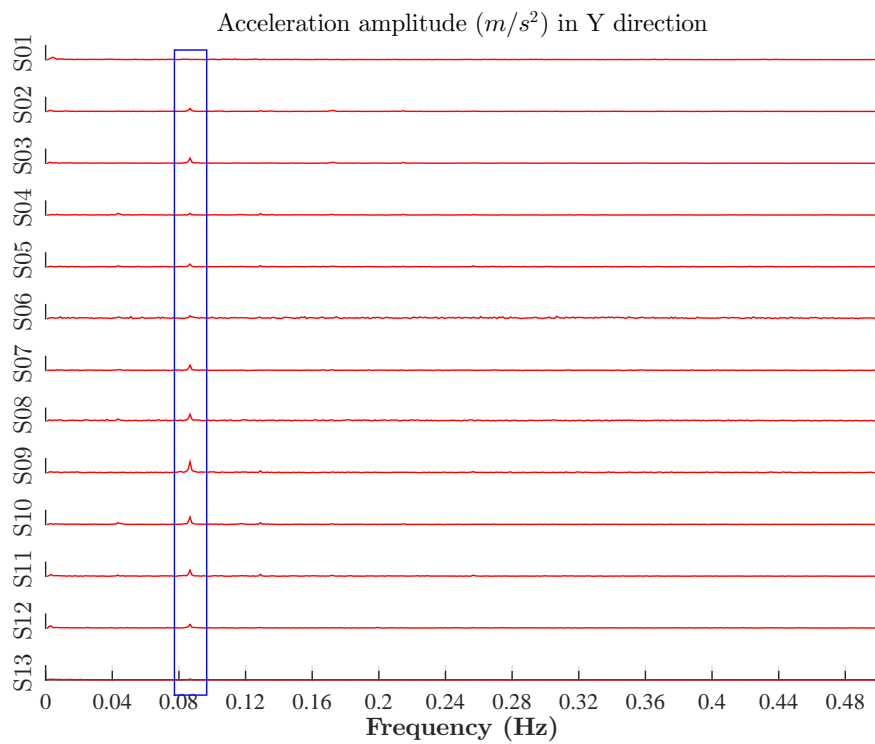


Figure 5.10 Spectra of acceleration in Y direction across all loggers (Event 58)

In order to predict the VIV response due to vessel motions, it is necessary to identify the vessel motion frequency (f_{im}) and the KC number distribution along the riser. As per the proposed model, these parameters determine the response frequency (f_{resp}). Figure 5.11 shows the displacement amplitude spectrum of logger S01 which is attached to the vessel. Since it measures purely the motion of the vessel and not the VIV, the peak of the spectrum should provide us with the frequency of the vessel motion. From the figure $f_{im}=0.0033$ Hz, which is reasonable for a MODU's slow varying motion due to the second order differential frequency loads.

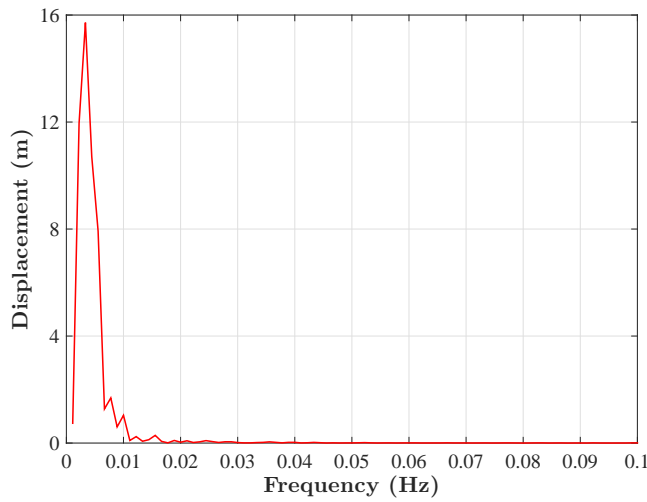


Figure 5.11 Displacement spectrum of logger S01 (Event 58)

Figure 5.12 shows the KC number distribution along the riser. As expected, since the vessel drift is of a larger amplitude, we have very high KC numbers. In order to apply the model and to predict the response with reasonable accuracy, it is necessary to define the representative KC number from the given distribution. This will define the value of N and in turn the predicted value of f_{resp} . As discussed in section 3.2.2, we take the midpoint of distribution as the representative KC. In this case we take it to be 203. Following the findings of Sumer and Fredsøe (2006), we get the value of N to be 26. Applying Equation 3.1, the value of f_{resp} is equal to 0.08668 Hz. This is the peak frequency that was found from the spectrum. Hence, it is possible to predict the response frequency of a full-scale riser using the empirical model.

Figure 5.13 shows the excitation frequencies from VIVANA compared with the peak frequency

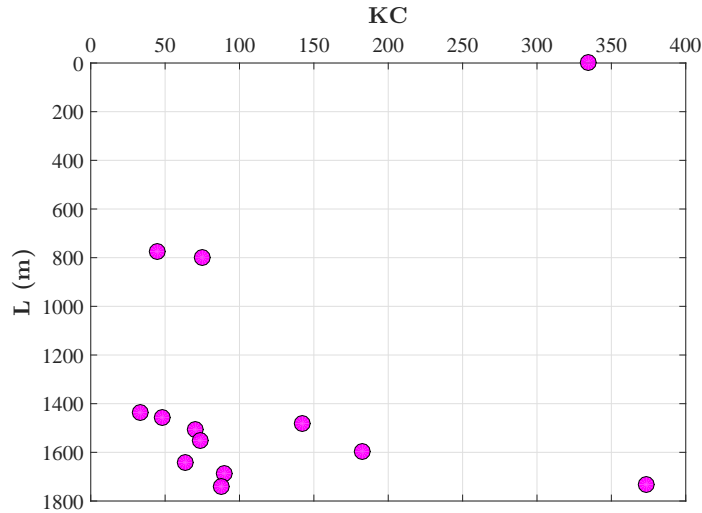


Figure 5.12 KC number distribution along the riser (Event 58)

from the displacement amplitude spectrum of logger S07. The frequencies are presented above 0.04 Hz in the spectrum as the peak at lower frequencies is very large because of the vessel displacement and here only the frequencies in VIV range are of interest. A very good agreement is achieved with the analysis and measurements. The dominant mode here is the 6th mode. A peak can be seen at 0.045 Hz. This falls in the wave-frequency range of 0.04-0.2 Hz and thus could be the response from wave induced motion.

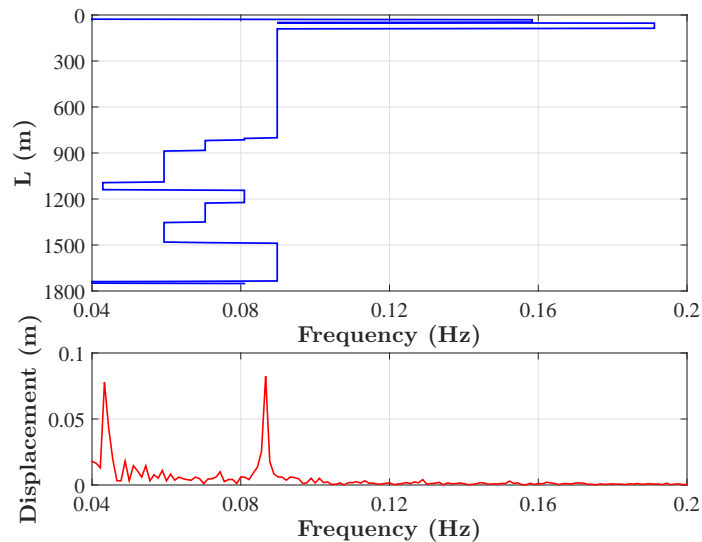


Figure 5.13 Excitation frequencies along the riser compared with displacement spectrum at logger S07 (Event 58)

Figure 5.14 shows the RMS A/D of the riser due to VIV. On comparing the RMS A/D

from the measurements and the numerical analysis at the lower part where the loggers are concentrated and measurements are available for comparison, we can see that the mode shape from the predicted response agrees well with the mode shape from the measurements. It is to be noted that the amplitudes of vibration from the numerical analysis is reduced by 60% based on the findings in case of irregular waves (Sumer and Fredsøe, 2006, p. 441-442).

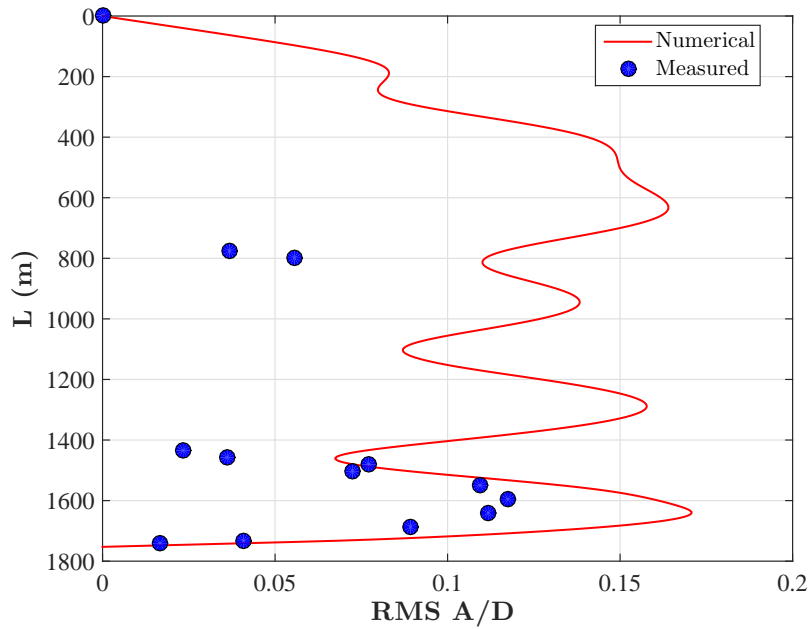


Figure 5.14 Comparison of RMS A/D along the riser (Event 58)

As mentioned before, the major goal of the validation was to prove that the empirical model could predict the response frequency and the associated mode with reasonable accuracy. In this case, it could predict the response frequency accurately. The mode shape also matches well with the mode shape from the measurements although we could not get a good agreement in terms of amplitudes.

5.5.1.2 Event 612

Event 612 is also a low current case like the previous one. Figure 5.15 shows the comparison of equivalent current profile generated from the acceleration measurements and the ocean current profile. The shedding frequency due to ocean current has a maximum of 0.1 Hz at the point of maximum current velocity, but otherwise ranges from 0.002-0.05 Hz.

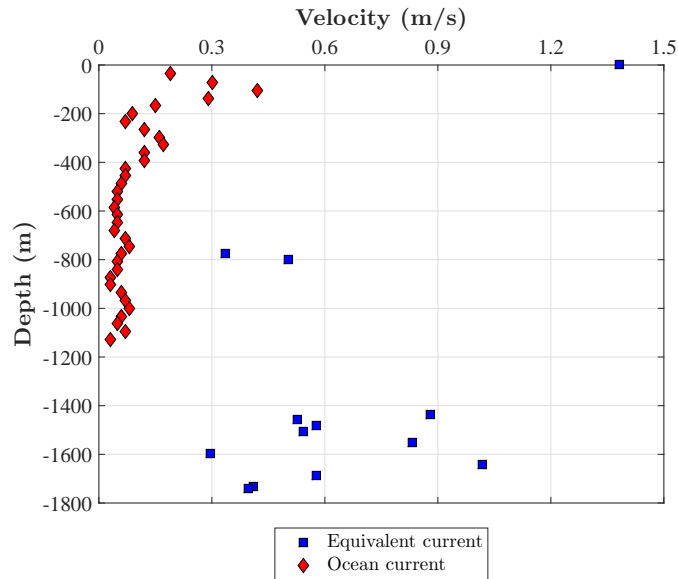


Figure 5.15 Generated equivalent current profile and the ocean current profile (Event 612)

Figures 5.16 and 5.17 show the acceleration amplitude spectra in X and Y directions respectively. It can be seen that the dominant response occur at frequencies of 0.054 Hz, 0.063 Hz and 0.1122 Hz.

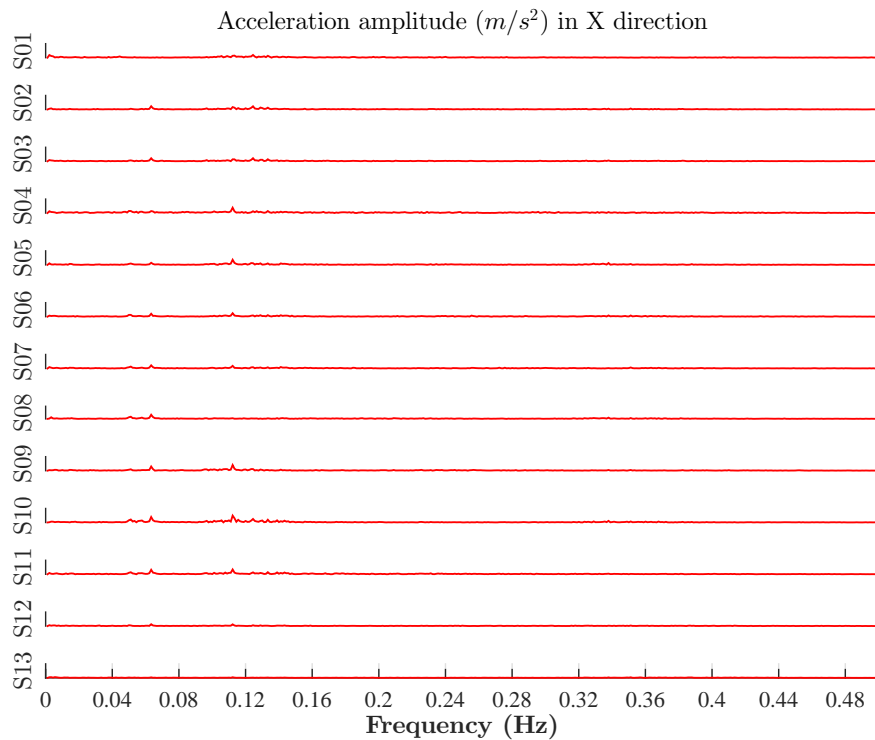


Figure 5.16 Spectra of acceleration in X direction across all loggers (Event 612)

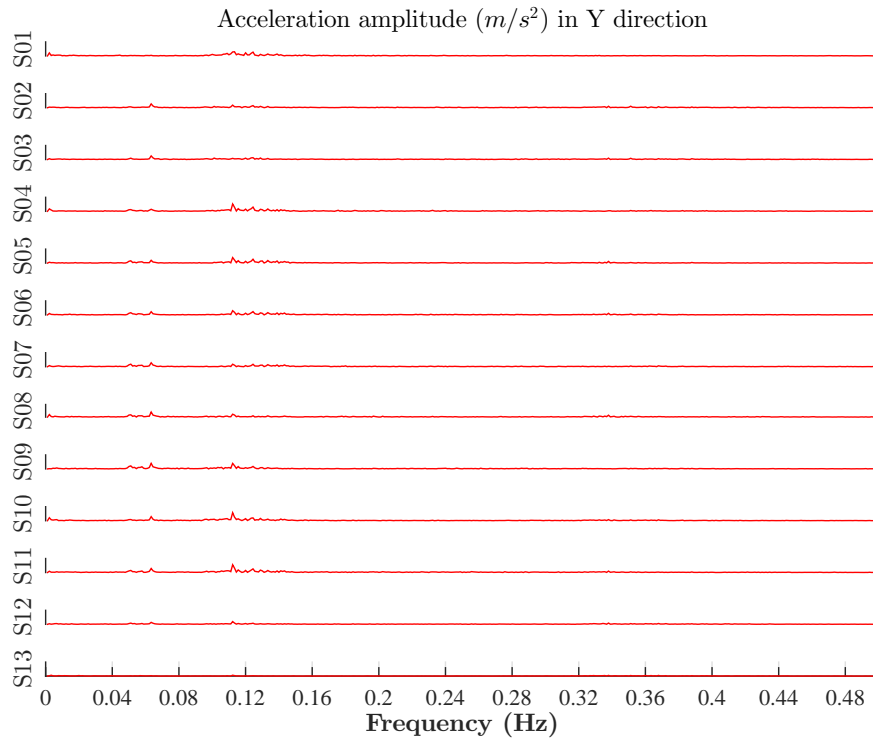


Figure 5.17 Spectra of acceleration in Y direction across all loggers (Event 612)

Figure 5.11 shows the displacement amplitude spectrum of logger S01. From the plot, the frequency of vessel motion in this case is found to be 0.0022 Hz.

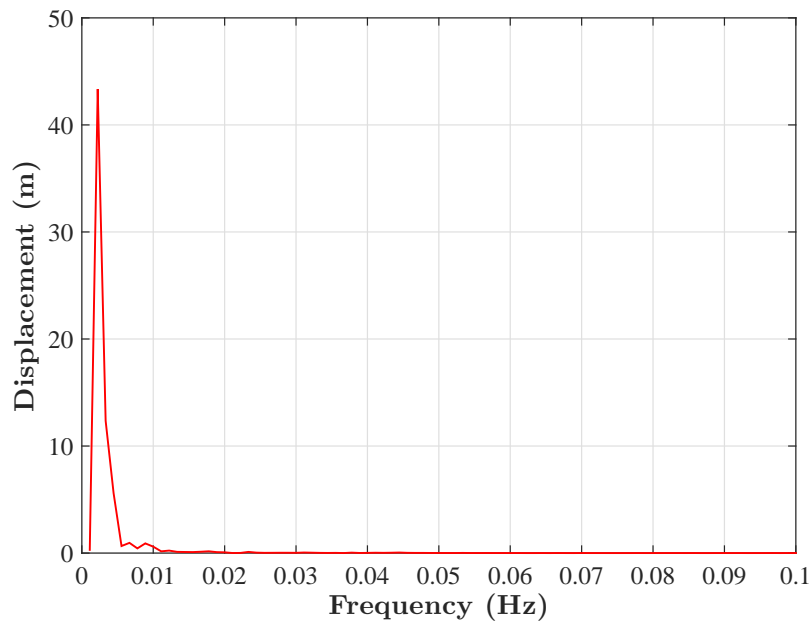


Figure 5.18 Displacement spectrum of logger S01 (Event 612)

The KC number distribution is shown in Figure 5.19. The representative KC in this case is also taken to be the midpoint of the distribution (refer section 3.2.2). Here, the KC number considered for the empirical model is 408, which means the value of N is 51. Hence, as per the model, the response frequency predicted is 0.1133 Hz. This frequency is close to one of the peaks of the spectrum. Thus it can be inferred that based on the KC distribution and empirical model, the dominant response is 0.1133 Hz.

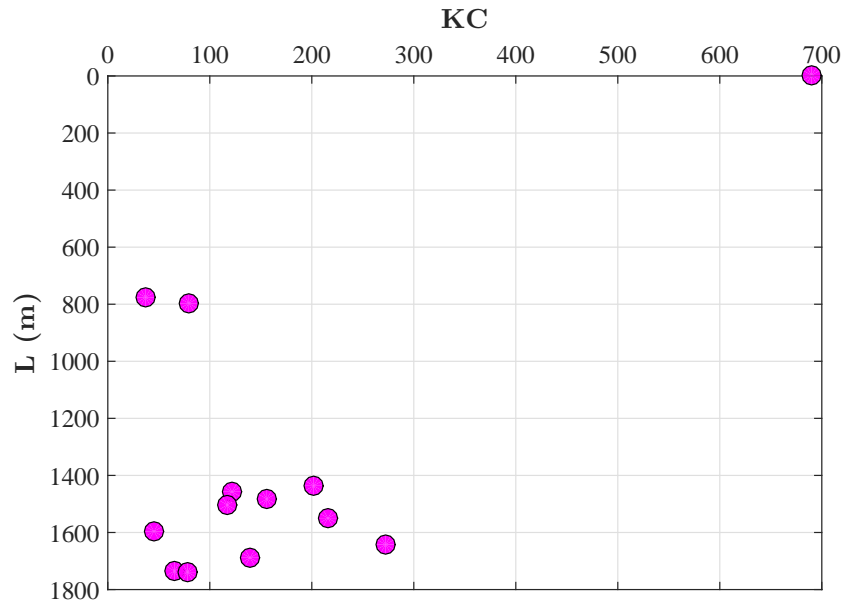


Figure 5.19 KC number distribution along the riser (Event 612)

In Figure 5.20, the excitation frequencies from numerical analysis is compared with the displacement spectrum of logger S05. The dominant response frequency from analysis matches with the peak frequency from the measurements. The dominant mode here is the 7th mode. The empirical model was able to predict the response based on the KC number distribution and vessel motion frequency. It should be noted that there were three peaks in the spectrum and from the model it is identified that 0.1122 Hz is the one causing the vessel motion-induced VIV. This is proved from the mode shape obtained from the measurements (refer Figure 5.21), which corresponds to the above mentioned frequency. The other two peak frequencies fall in wave-frequency range and could be the response from wave induced motion.

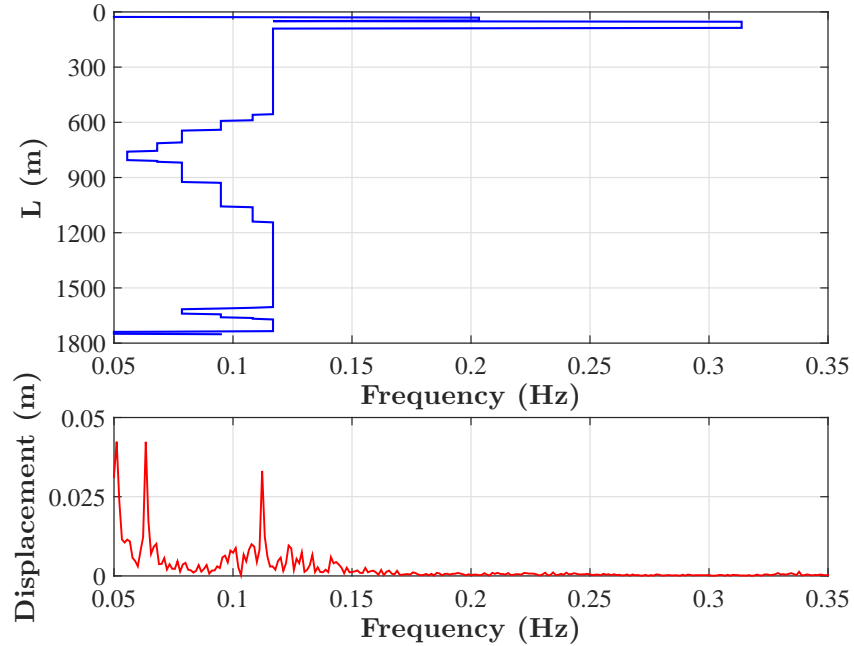


Figure 5.20 Excitation frequencies along the riser compared with displacement spectrum at logger S05 (Event 612)

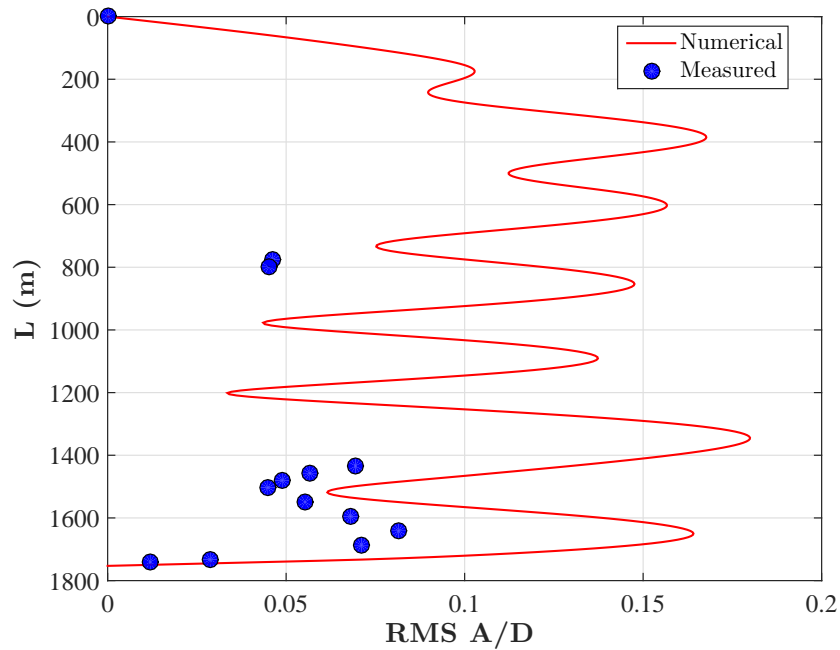


Figure 5.21 Comparison of RMS A/D along the riser (Event 612)

The comparison of RMS A/D from the analysis and measurements are presented in Figure 5.21. It can be seen, at the bottom part where measurements are available, that the mode

shape from the two is in good agreement. As in the previous case, the amplitudes from the analysis are reduced by 60% since this is caused by irregular motion. Although the amplitudes from the analysis and the measurements do not match, the main goal of predicting the correct mode has been achieved.

5.5.1.3 Event 413

Figure 5.22 shows the comparison of equivalent current from the vessel motion and the ocean current for Event 413.

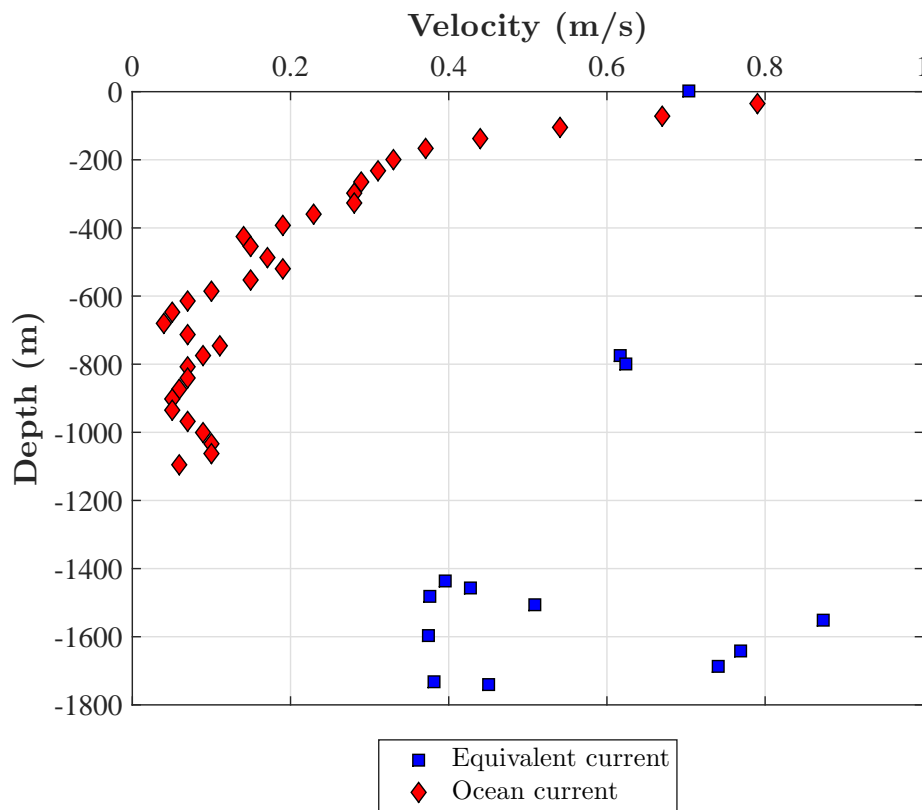


Figure 5.22 Generated equivalent current profile and the ocean current profile (Event 413)

It can be seen that the maximum velocity of ocean current is almost similar in magnitude to the velocity of vessel motion. As such, this case cannot be adjudged as a case of pure vessel motion-induced VIV or of pure current-induced VIV. A look at Figure 5.23, which compares the vortex shedding frequencies, reveals that both the current profiles can excite similar frequencies of vibration.

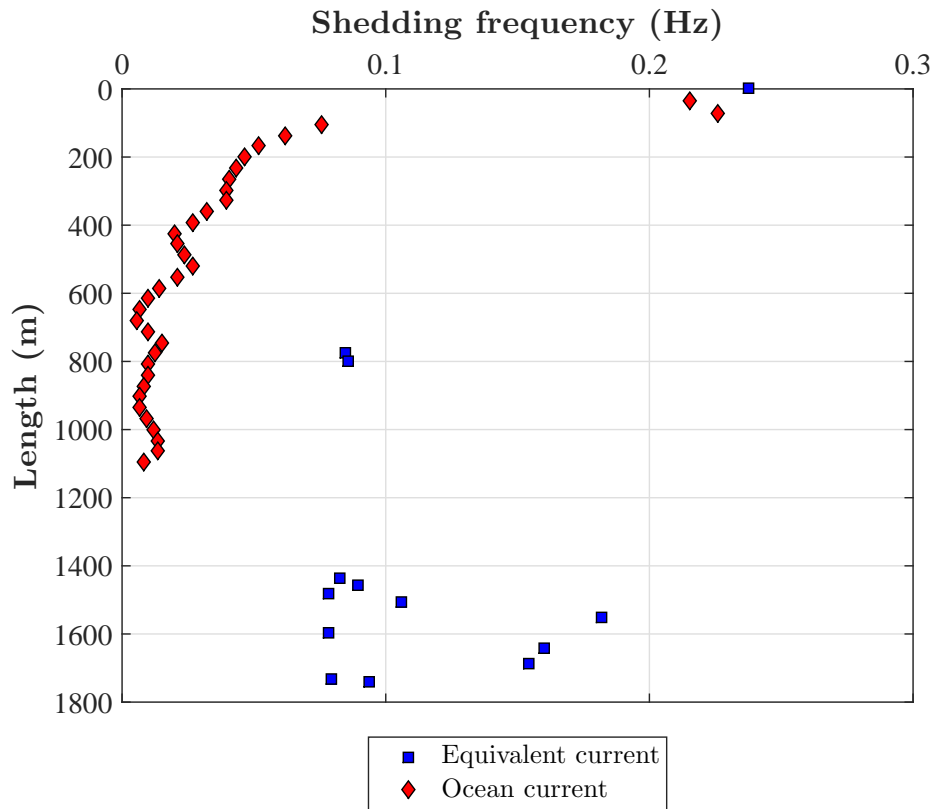


Figure 5.23 Comparison of shedding frequencies (Event 413)

Figures 5.24 and 5.25 presents the spectra of accelerations in X and Y directions. Peaks could be identified at 0.0833 Hz, 0.068 Hz and at some frequencies in the lower range.

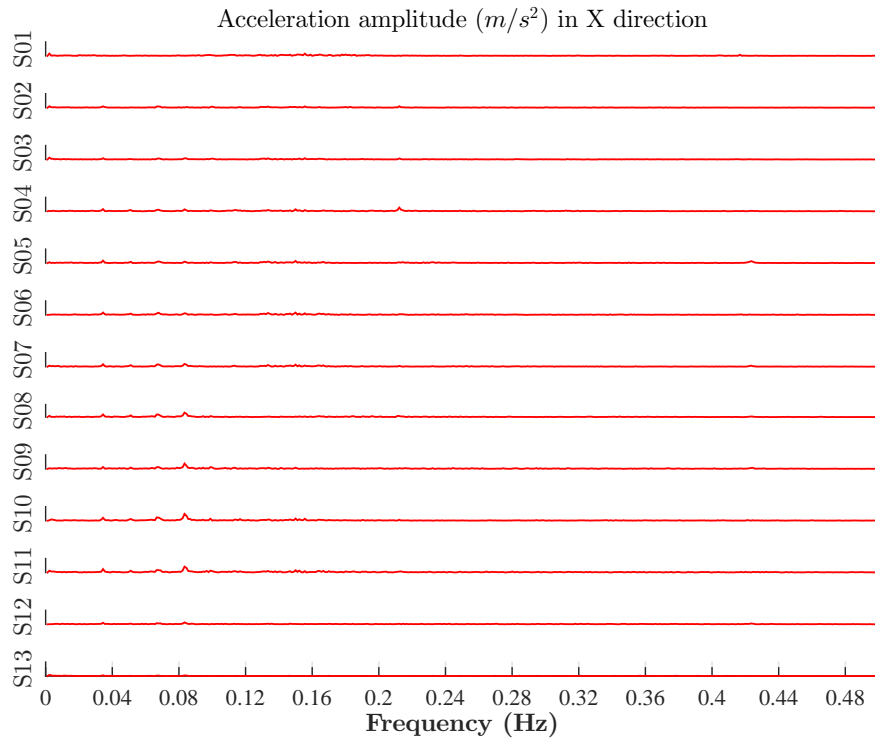


Figure 5.24 Spectra of acceleration in X direction across all loggers (Event 413)

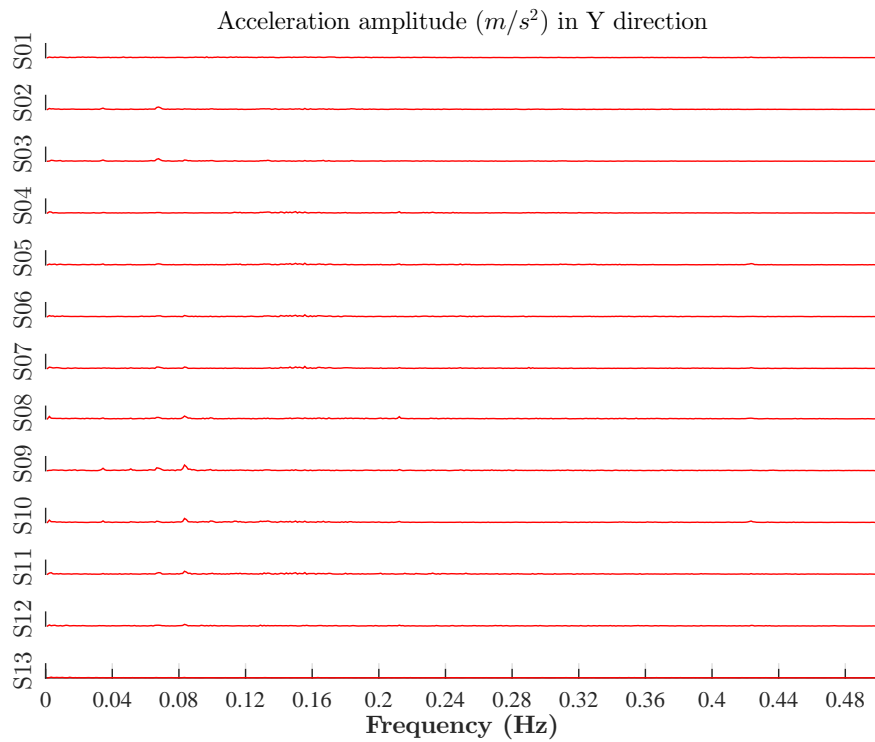


Figure 5.25 Spectra of acceleration in Y direction across all loggers (Event 413)

The empirical model is applied to the event to predict the response and is compared with the response frequencies from the measurements. Figure 5.26 represents the displacement amplitude spectrum from the logger S01. Vessel motion is identified to be with a frequency of 0.00223 Hz.

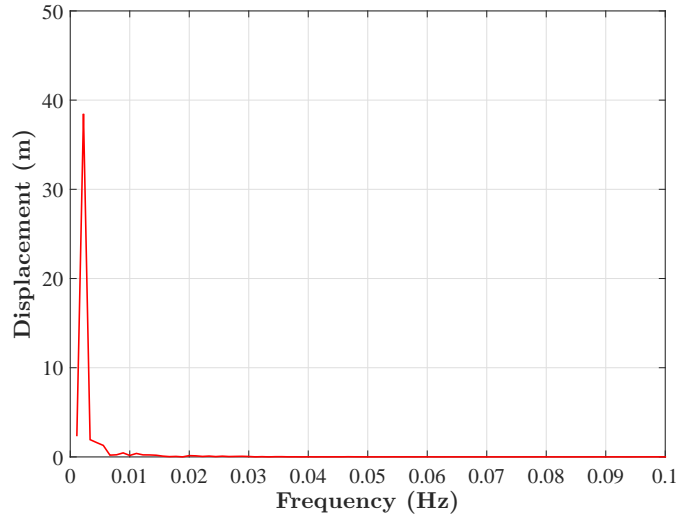


Figure 5.26 Displacement spectrum of logger S01 (Event 413)

The KC number distribution is shown in Figure 5.27. We take the representative KC to be the midpoint value as discussed in section 3.2.2. The midpoint value here is 319 which leads to a value of 40 for the ratio N . Hence, the response frequency can be estimated to be 0.0889 Hz.

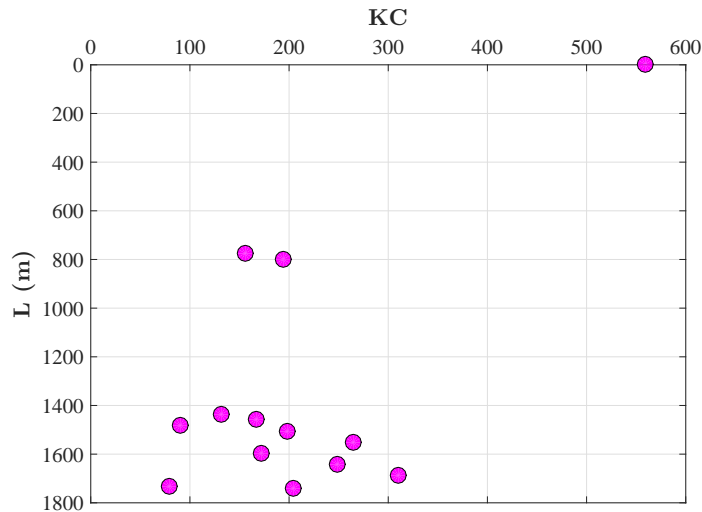


Figure 5.27 KC number distribution along the riser (Event 413)

The excitation frequencies are presented in Figure 5.28 and is compared with the displacement spectrum of logger S09. The response predicted using the model is in close agreement with the peak response from the accelerations. The dominant mode here is the 6th mode.

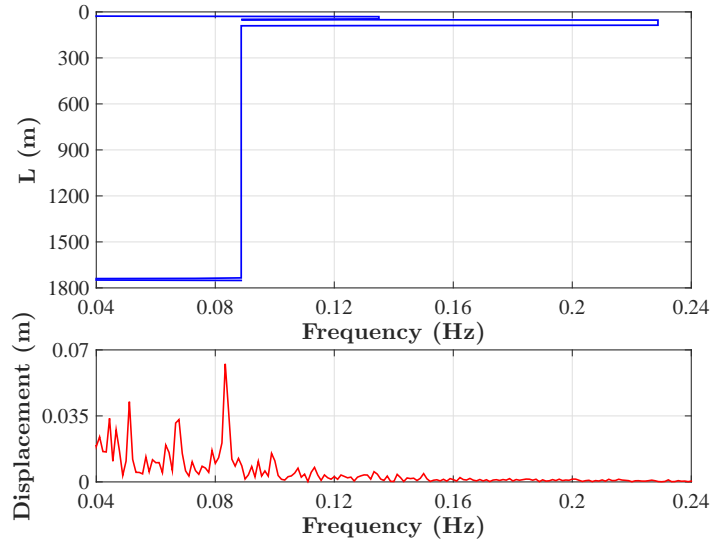


Figure 5.28 Excitation frequencies along the riser compared with displacement spectrum at logger S09 (Event 413)

The comparison of RMS A/D in Figure 5.29 shows that the mode shape from analysis agrees well with that obtained from the measurements.

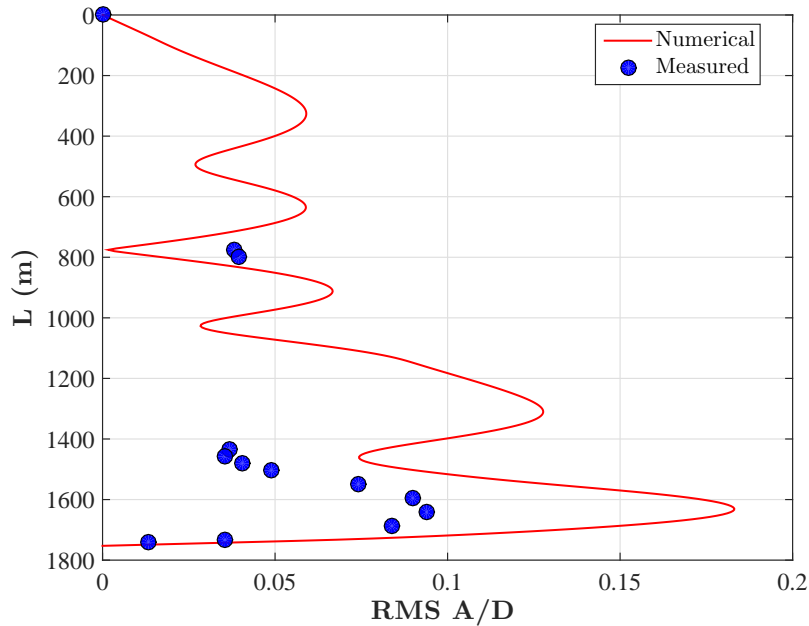


Figure 5.29 Comparison of RMS A/D along the riser (Event 413)

A good agreement is achieved with the response predicted by the numerical analysis and the one obtained from the measured data. Here both the ocean current and the vessel motion could induce VIV with a frequency close to the one obtained from data. The proposed empirical model was able to predict the frequency of vessel motion-induced VIV which is validated by the measured results. Though it is uncertain whether the current or the vessel motion causes VIV here, we were able to predict the response due to one of the contributing factor.

5.5.2 Ocean current-induced VIV dominant cases

5.5.2.1 Event 434

Event 434 is a high current case with a very low velocity of vessel motion. Figure 5.30 shows the comparison of current velocities for equivalent current and ocean current. Here, the equivalent current due to vessel motion is very less compared to the ocean current. Hence, in this case the VIV could be purely due to the current.

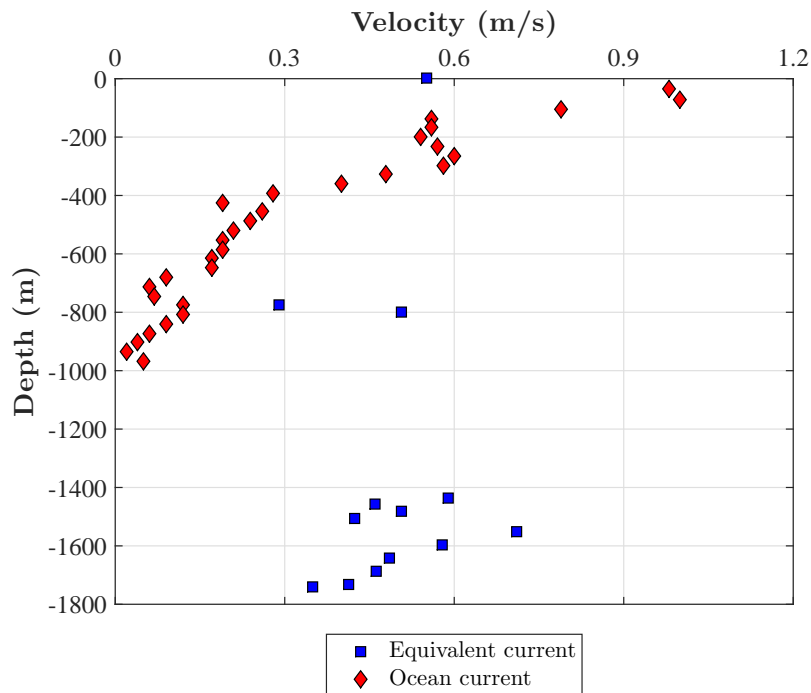


Figure 5.30 Generated equivalent current profile and the ocean current profile (Event 434)

Figures 5.31 and 5.32 shows the acceleration spectrum across the loggers in X and Y direction respectively. The peak response can be found at a frequency of 0.084 Hz.

Since vessel motion is not the cause of VIV here, this can be analysed based on the ocean current velocity. The ocean current profile is used with an St value of 0.2 to predict the VIV. Figure 5.33 shows the excitation frequencies along the length of the riser due to the current. The displacement spectrum of the logger S03 is also presented to compare the dominant frequencies. The current, albeit of high velocity, is heavily sheared and reduces to negligible velocity after a depth of 600 m. Thus the dominant frequency is present at the top part of the riser as the rest of the riser encounters a very low velocity and shedding frequency. The dominant response frequency from the analysis corresponds well with the response frequency found from the measurements.

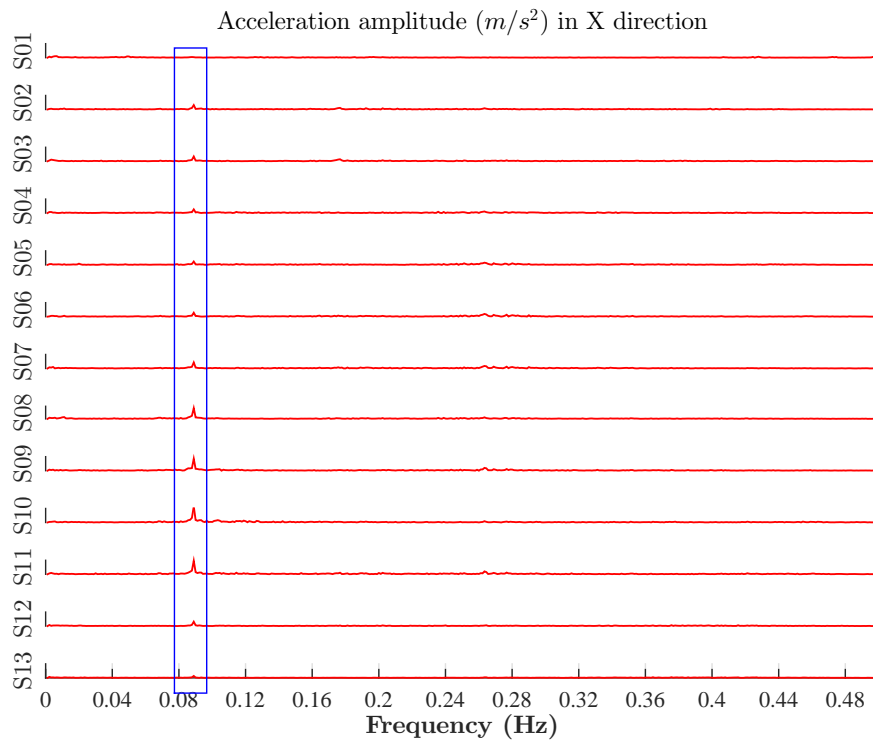


Figure 5.31 Spectra of acceleration in X direction across all loggers (Event 434)

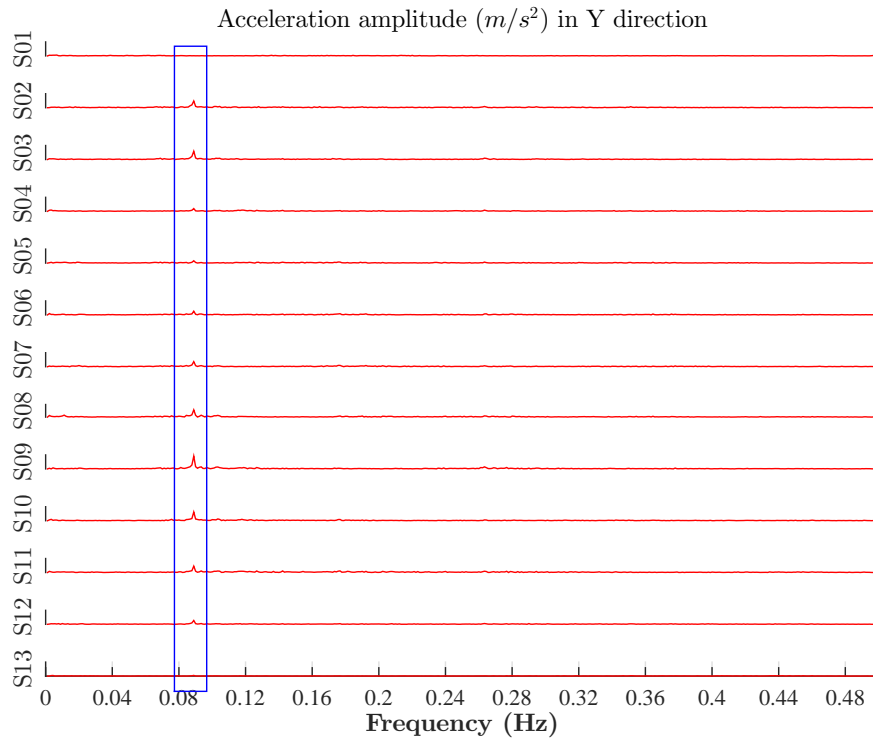


Figure 5.32 Spectra of acceleration in Y direction across all loggers (Event 434)

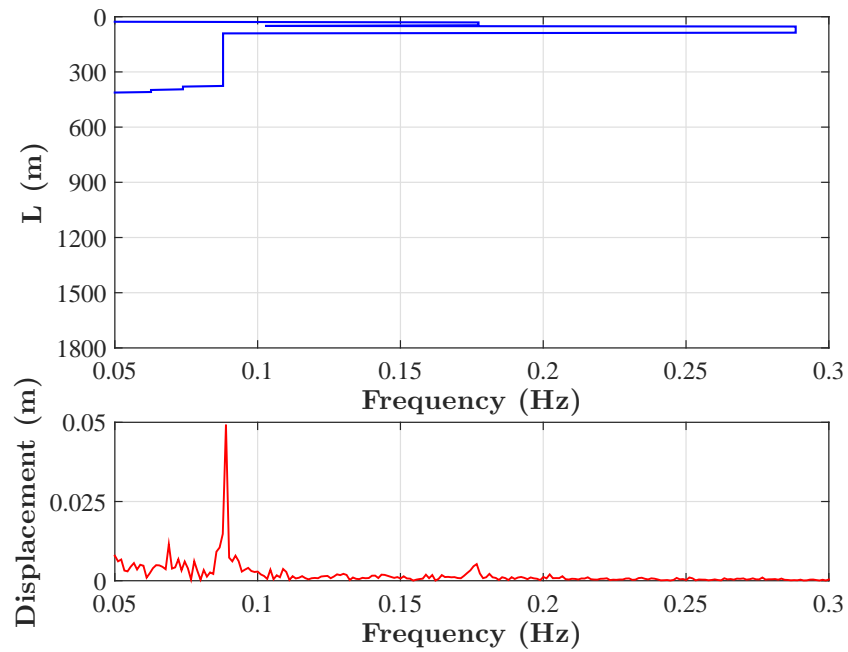


Figure 5.33 Excitation frequencies along the riser compared with displacement spectrum at logger S03 (Event 434)

Figure 5.34 presents the comparison of RMS A/D from the measurements and the analysis.

Though the amplitude is not equal, the mode shape from both cases is similar to each other which is evident when comparing the lower part of the riser.

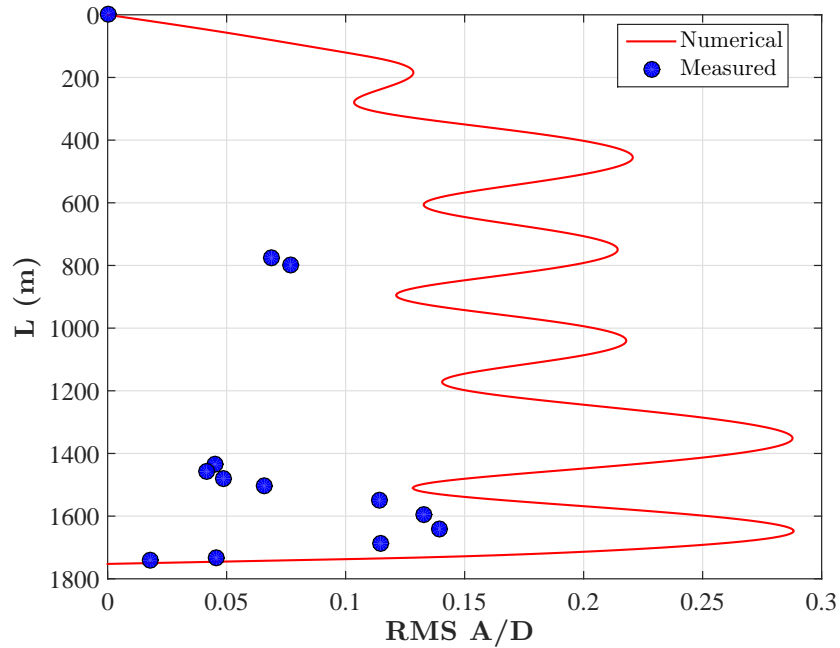


Figure 5.34 Comparison of RMS A/D along the riser (Event 434)

5.5.3 Discussion

Vessel motion-induced VIV during a full-scale drilling scenario is firstly identified. The validation of the proposed empirical model using the full-scale drilling riser measurements was performed and the results point out that the model can be extended to a long riser in its actual operational environment. Although the full-scale riser under study was subjected to flow of high KC numbers, the model was applied and validated as it is generic and applicable in all KC ranges. The vessel motion-induced VIV could be identified in the some cases and response frequencies were predicted using the model. In all cases, the response frequencies and the mode shape from the measurements were in good agreement with the ones predicted using the empirical model.

A major uncertainty here is in the identification of the vessel motion frequency. The frequency resolution of the measurements is 0.001 Hz. Due to lack of vessel data or mooring details,

it was difficult to ascertain the reasonableness of the obtained vessel motion frequencies. Also the fact that the duration of measurements is only 15 mins adds to uncertainty in the obtained results. Prior works by Tognarelli et al. (2008) and Thethi et al. (2005) based on riser monitoring data were focussed only on finding the response in the VIV frequency range. Typically, the accelerometers are not accurate in low frequencies, but the vessel displacements obtained by integration is within the range of typical vessel drifts.

Chapter 6

Numerical VIV Prediction of Deep Sea Mining Riser

6.1 Introduction

In the previous chapters, the proposed empirical model was validated against small-scale model tests and full-scale riser measurements. The results obtained gives confidence to apply the procedure to predict the vessel motion-induced VIV of an ultra-long deep sea mining riser. As mentioned in Chapter 1, the VIV is a major concern for the free-hanging mining riser. With the mining industry targeting deeper waters in the world's oceans, focus on improving the existing technology to prevent such concerns is vital. In this chapter, the empirical model is applied to a 5,000 m long deep sea mining riser. The configuration of the riser is adopted from the at-sea experiments conducted in the North Pacific Ocean in the 1970s (Chung, 2010). The focus is mainly on vessel motions in low KC number ranges where the empirical model holds high significance. The surge and sway motions of the support vessel depends largely on the type of sea-keeping used. For deep sea mining support vessels, dynamic positioning is more practical and hence low KC number scenarios are possible.

6.2 Riser Configuration

The riser is deployed from the moon pool of a production support vessel. The riser is pinned at the top with rotation around the longitudinal axis restricted. The bottom end is free and a buffer weight is placed at the bottom of the riser for stability. The buffer usually contains the pumping equipment and typical weight of the buffer is obtained from literature (Chung et al., 1994). The resistance offered by the flexible hoses connected to the SPTs is quite minimal and is neglected here. Figure 6.1 shows the configuration of the riser.

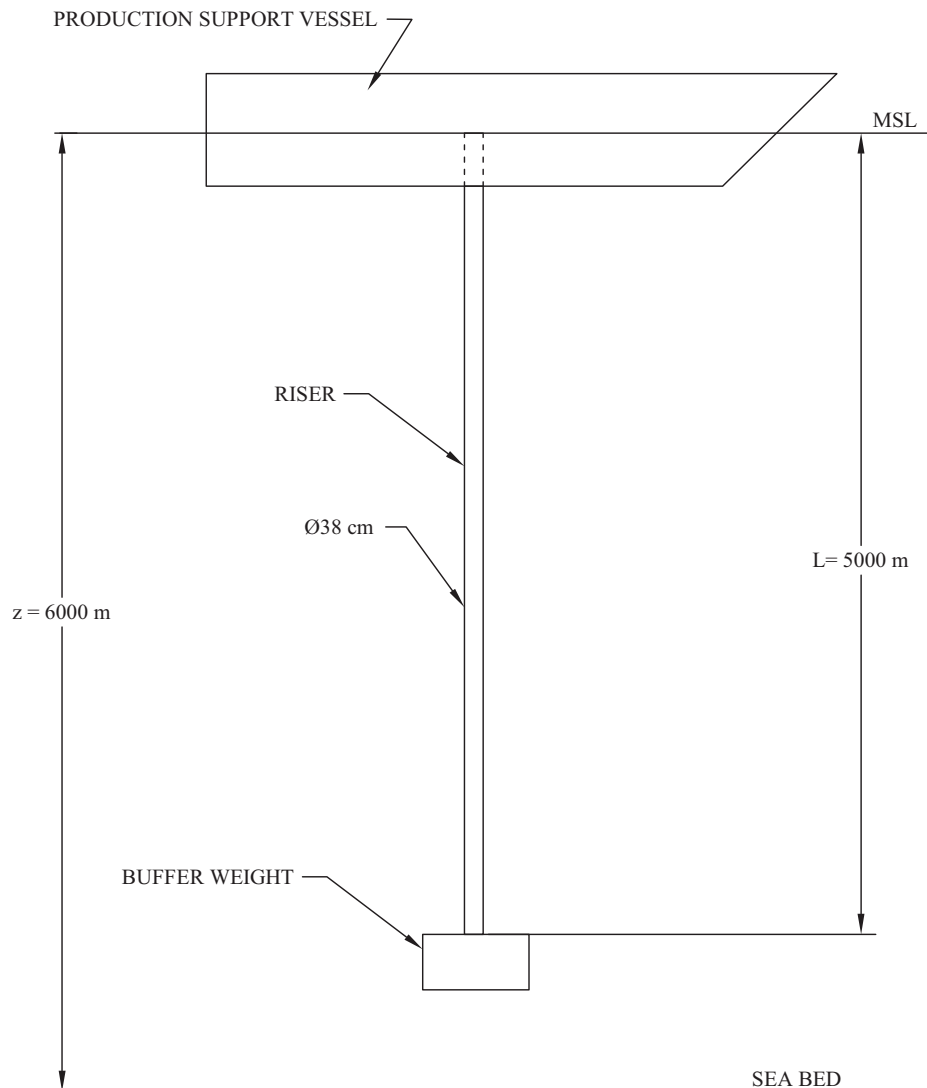


Figure 6.1 Configuration of the riser

The dimensions and properties of the riser are given in Table 6.1.

Table 6.1 Properties of the riser

Item	Value	Unit
Length	5000	m
Outer diameter	0.38	m
Inner diameter	0.19	m
Cross-sectional area, A	0.085	m ²
Modulus of elasticity, E	2.07×10^{11}	N/m ²
Bending stiffness, EI	1.98×10^8	Nm ²
Tensioning stiffness, EA	1.76×10^{10}	N
Mass/unit length in air	667.7	kg/m
Mass of buffer in air	203.2	tons

6.3 Simplifications and Assumptions

Following simplifications and assumptions are used in the analysis:

1. In real cases, the riser has an asymmetry because of cables running along its length and pumps installed off-center of the riser (Chung and Tsurusaki, 1994). In the analysis, the effect of asymmetry is not considered and riser is assumed to be symmetric along its axis.
2. The top end of the riser is assumed to be at the still water level and the whole length is submerged in water.
3. IL VIV is not considered in the analysis. IL responses, apart from being smaller in magnitude compared to CF VIV, are in the direction of the vessel motion. The frequency of vessel motion is dominant and thus IL frequency can be neglected. Hence, only CF VIV is of interest in the present analysis.

6.4 Case Studies

In the analysis, the riser is subjected to various imposed motions - both regular and irregular. Low KC number cases are being considered here and as such the vessel drift in all cases are quite small. Three cases of simple harmonic surge motion at different frequencies are studied along with a low frequency irregular motion case. Finally, the VIV due to pure current is investigated to compare the stresses and fatigue caused by vessel motion-induced VIV with that of current-induced VIV.

The methodology followed for the analysis is similar to the one followed in Chapter 4. The dynamic analysis of the modelled riser is conducted in RIFLEX to obtain the displacements at each node of the riser. The velocity time series are then derived at each node. Then, the equivalent current profile is generated based on Equation 3.3. Finally, the proposed empirical model is followed to predict the VIV response in VIVANA(refer Figure 3.6). The midpoint of the KC distribution is taken to be the representative KC range.

The eigen frequencies of the riser and the normalized mode shapes are presented in Figures 6.2 and 6.3 respectively.

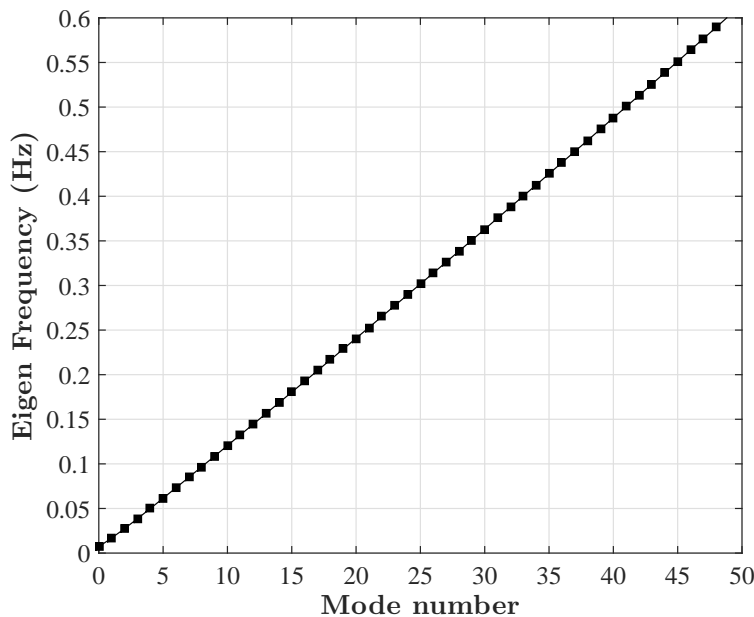


Figure 6.2 Eigenmodes and eigen frequencies for the deep sea mining riser

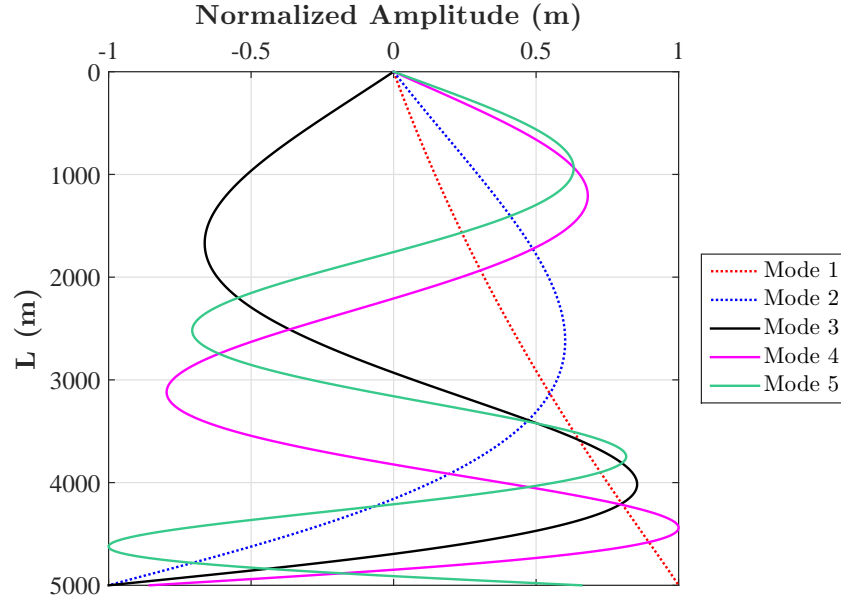


Figure 6.3 Normalized mode shapes for the deep sea mining riser

6.4.1 Regular motion case with $A=1.5$ m

In this case study, we consider harmonic surge motion of the vessel with an amplitude of 1.5 m. The KC number at the top is thus found to be 24.8. Two periods of motion are studied in the case - with 6 s and with 12 s. The details of the vessel motion are presented in Table 6.2.

Table 6.2 Vessel motions for regular motion case with $A=1.5$ m

Amp (m)	T (s)	f (Hz)	KC_{top}
1.5	6	0.1667	24.8
	12	0.0833	

The generated equivalent current profiles for both the frequencies are shown in Figure 6.4. The motion with higher frequency has the higher velocities.

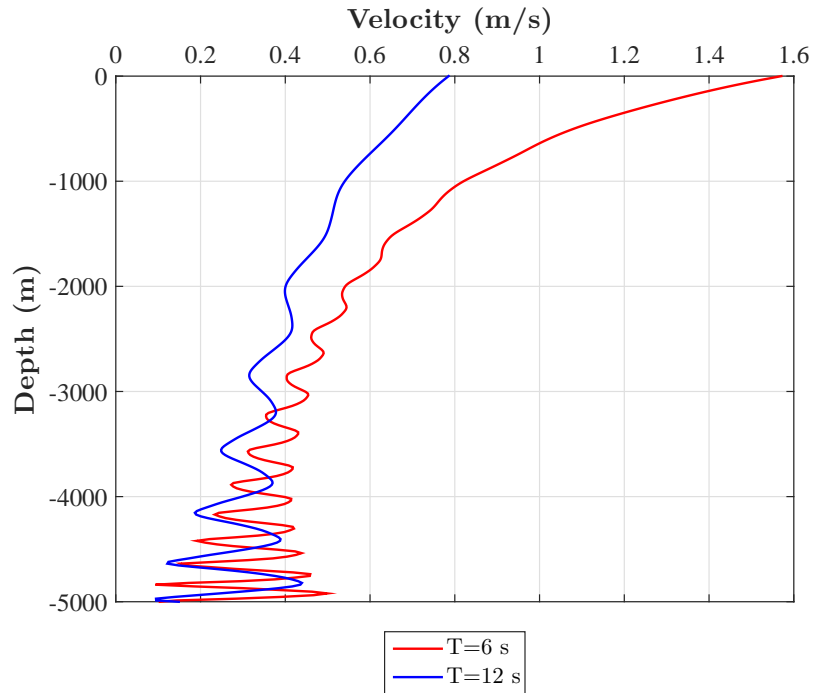


Figure 6.4 Equivalent current profile (regular motion case with $A=1.5$ m)

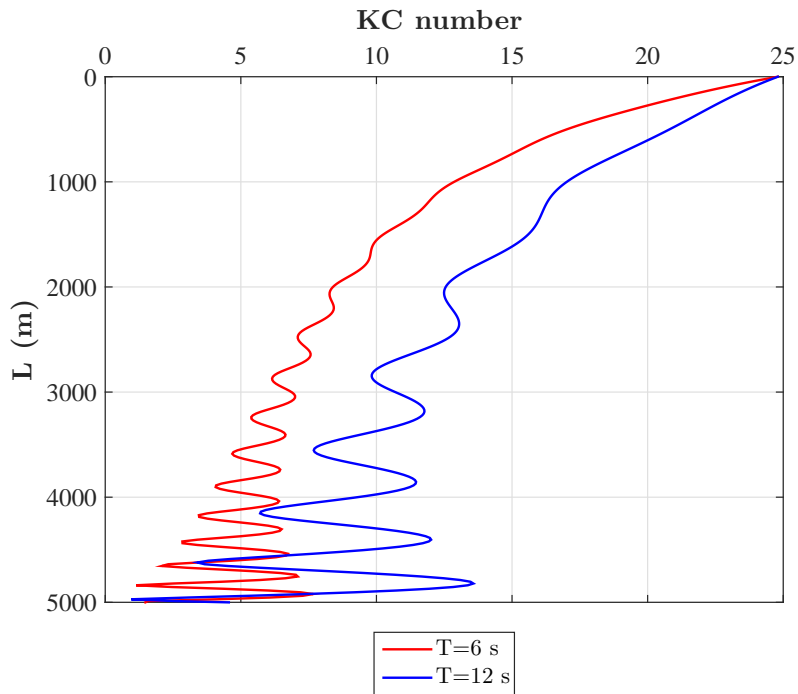


Figure 6.5 KC number distribution (regular motion case with $A=1.5$ m)

Figure 6.5 compares the KC number distribution along the riser due to both the frequencies. Although the top KC number is same, variation in KC is different for both the cases since

in the lower frequency case the riser is displaced more than the higher frequency case. The midpoint of both KC distribution fall in the range of 7-15 and hence, we select $N=2$ from Table 3.1.

Applying Equation 3.1, we get:

For $T=6$ s, $f_{resp} = 0.33$ Hz, and

For $T=12$ s, $f_{resp} = 0.17$ Hz

The value of St^* calculated for the response is 0.12 in this case study.

Figure 6.6 presents the excitation frequencies along the riser obtained from the VIVANA analysis. The dominant response frequencies are the ones predicted using the model. Heavy shear in the current profile for the case with $T=6$ s resulted in the lower shedding frequencies at the lower part of the riser. As such the dominant response frequency is allocated a zone at the top part of the riser.

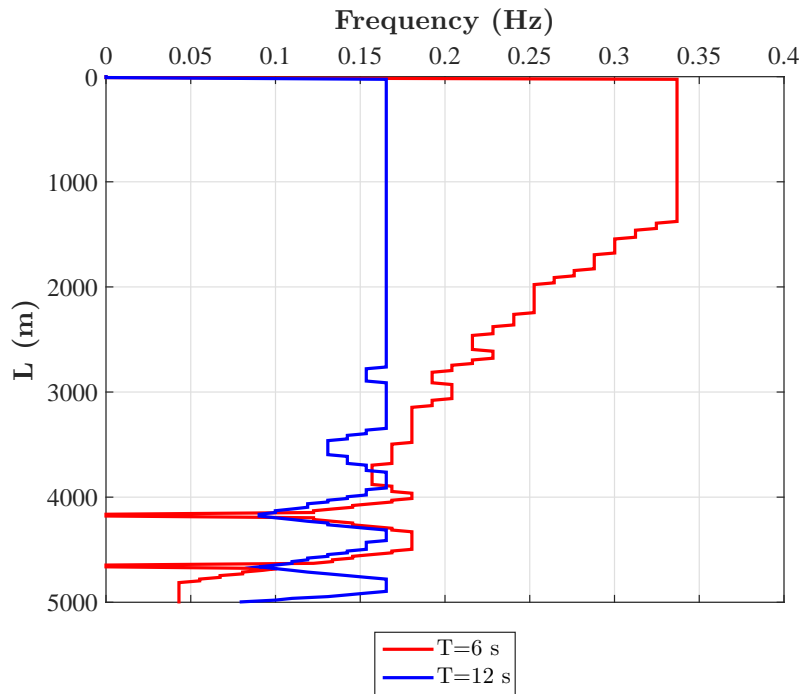


Figure 6.6 Excitation frequencies (regular motion case with $A=1.5$ m)

The RMS A/D of the riser is shown in Figure 6.7. The higher frequency motion has a comparatively lower amplitude of vibration than the lower frequency motion. Large variations in amplitudes can be seen at the bottom of the riser, which is free to move.

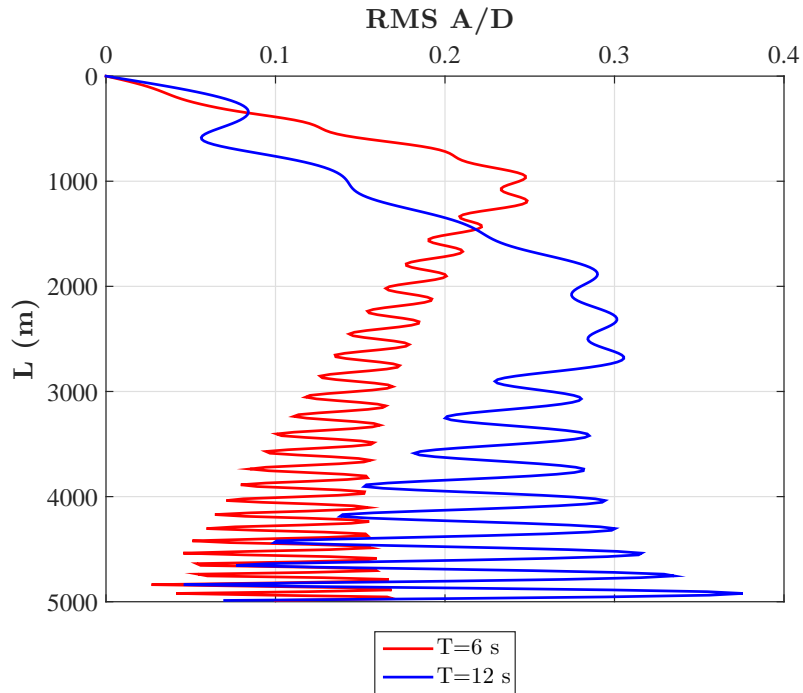


Figure 6.7 RMS A/D along the riser (regular motion case with A=1.5 m)

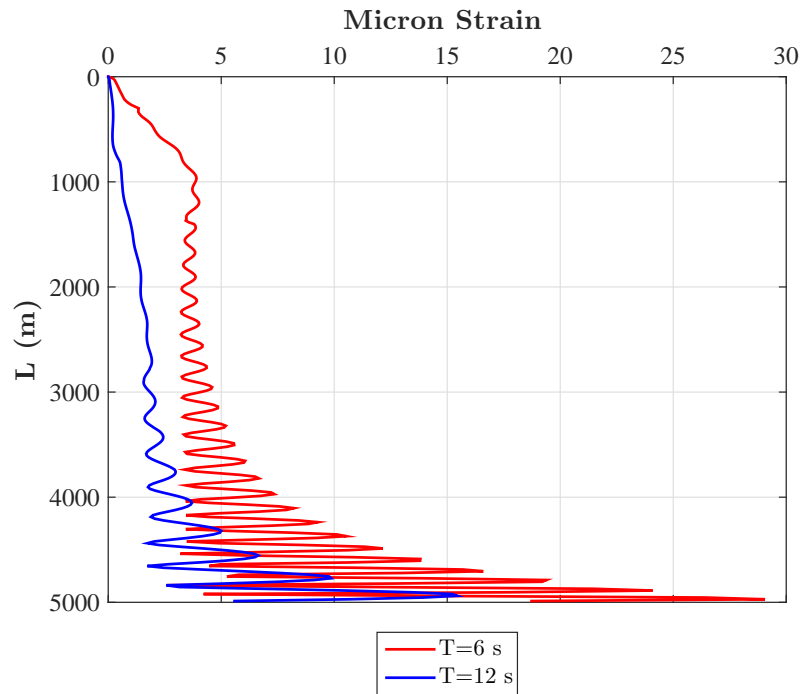


Figure 6.8 Strain along the riser (regular motion case with A=1.5 m)

The strain distribution along the length of the riser is presented in Figure 6.8. The value remains nearly a constant for almost the initial 3000 m of the riser, but experiences a sharp

increase at the bottom part. For both $T=6$ s and $T=12$ s, the highest value of strain is obtained at the bottom most part of the riser, which experiences a large variation in amplitude. This variation causes the curvature, which is the double differential of amplitude, to be high and results in high strains.

The fatigue analysis of the riser was conducted and the fatigue damage along the riser is shown in Figure 6.9. The fatigue is calculated using the DNV SN curve B1 (DNV RP C203, 2010) for structure in seawater with free corrosion. The values used in the SN curve are:

- Negative inverse slope of the SN curve, $m = 3.0$
- Intercept of log N axis, $\log \bar{a} = 12.436$

The minimum fatigue life occurs at the bottom of the riser, which is subjected to the maximum strain. The minimum fatigue life at the bottom portion is 117.7 years for $T=6$ s and 1603.1 years for $T=12$ s.

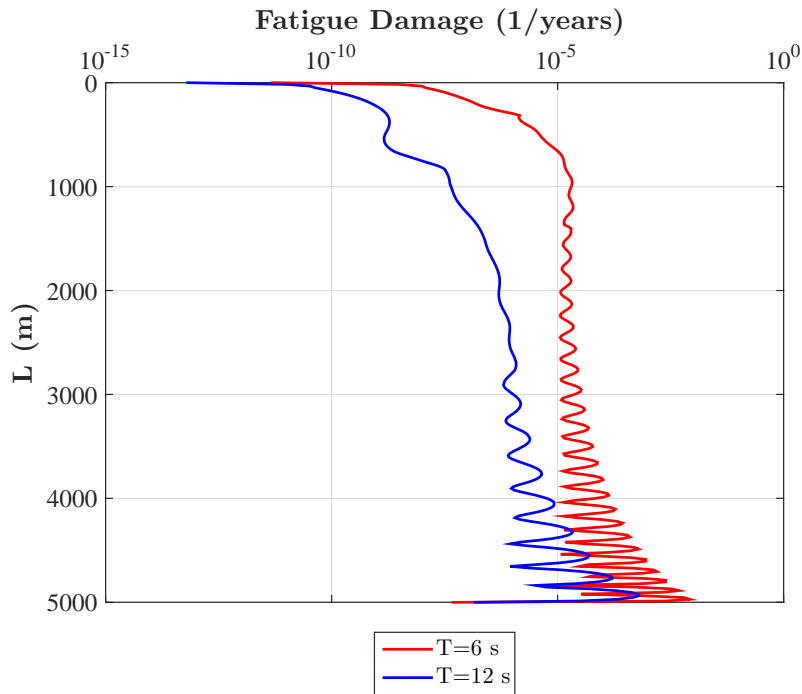


Figure 6.9 Fatigue damage along the riser (regular motion case with $A=1.5$ m)

6.4.2 Regular motion case with $A=2.5$ m

In this case study, we consider harmonic surge motion of the vessel with an amplitude of 2.5 m. This will result in a top KC number of 41.3. Similar to the previous case study, two periods of motion are studied - with 6 s and with 12 s. The details of the vessel motion are presented in Table 6.3.

Table 6.3 Vessel motions for regular motion case with $A=2.5$ m

Amp (m)	T (s)	f (Hz)	KC_{top}
2.5	6	0.1667	41.3
	12	0.0833	

Figure 6.10 shows the comparison of equivalent current profiles from both frequencies.

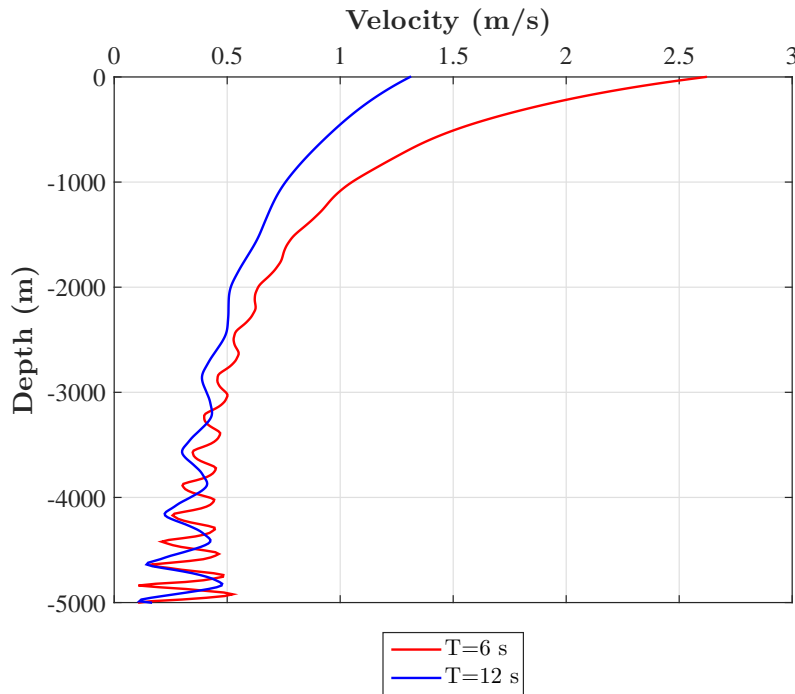


Figure 6.10 Equivalent current profile (regular motion case with $A=2.5$ m)

The KC number distribution is presented in Figure 6.11. Even though the top KC is above 40, the midpoint of the distribution falls in the range of 15-24 and hence this case qualifies as a case of low KC number. We select $N=3$ from Table 3.1.

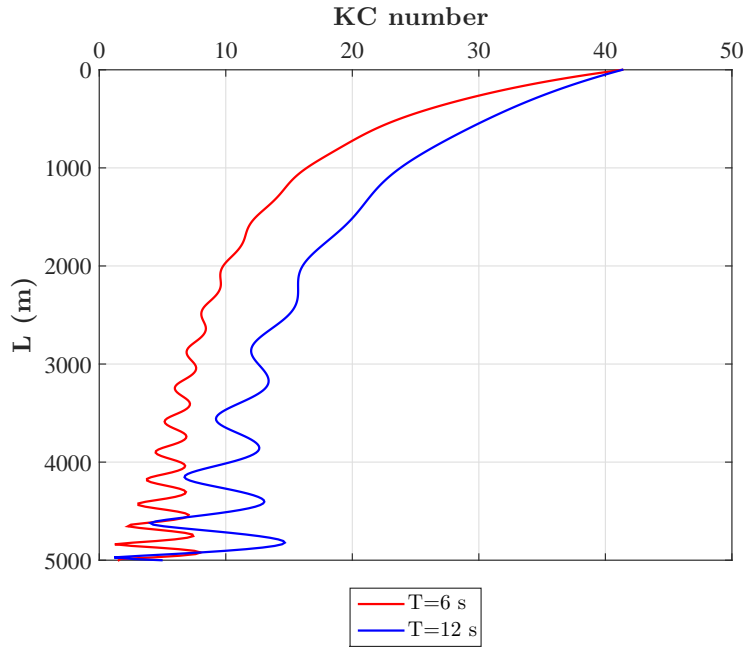


Figure 6.11 KC number distribution (regular motion case with $A=2.5$ m)

Applying Equation 3.1, we get:

For $T=6$ s, $f_{resp} = 0.5$ Hz, and

For $T=12$ s, $f_{resp} = 0.25$ Hz

The value of St^* calculated for the response is 0.108 in this case study.

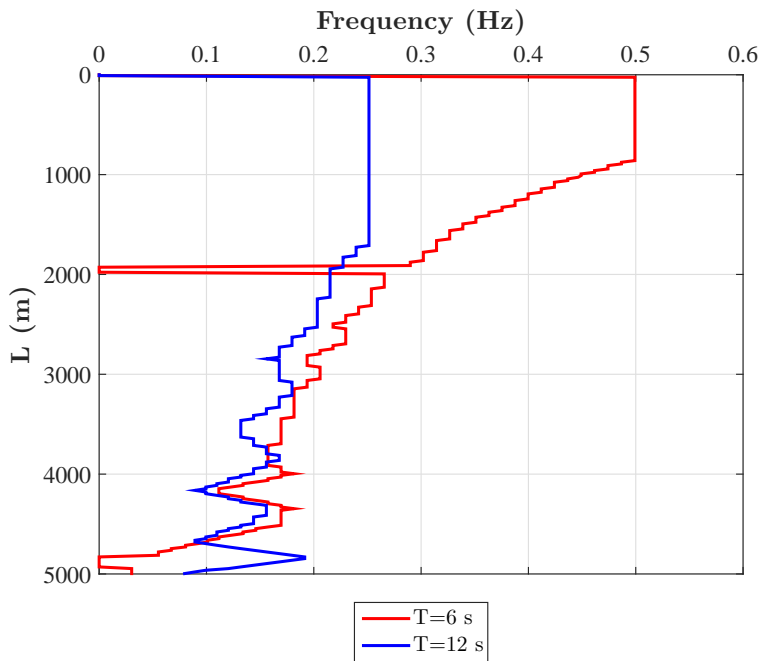


Figure 6.12 Excitation frequencies (regular motion case with $A=2.5$ m)

The excitation frequencies along the riser are shown in Figure 6.12. The response frequencies predicted using the empirical model is achieved in the analysis.

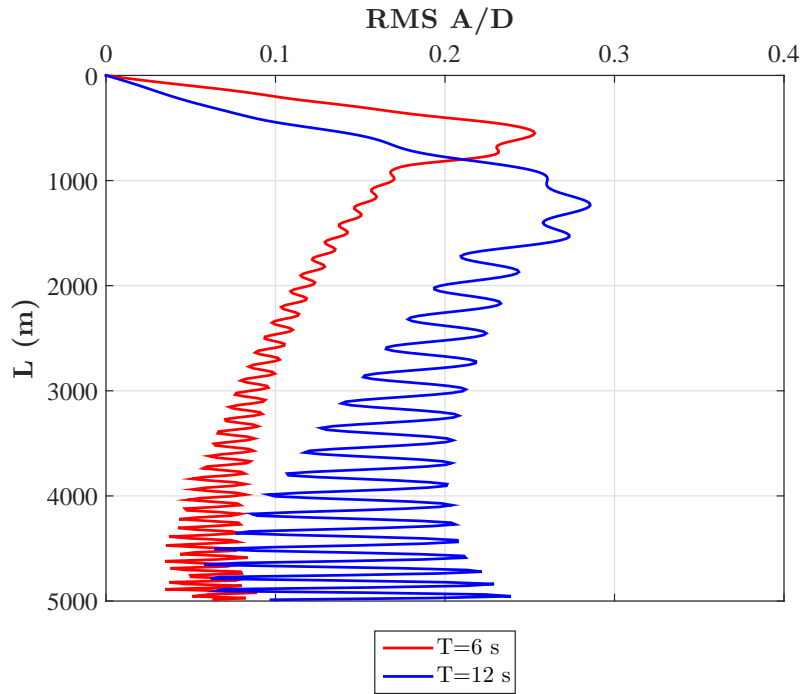


Figure 6.13 RMS A/D along the riser (regular motion case with $A=2.5$ m)

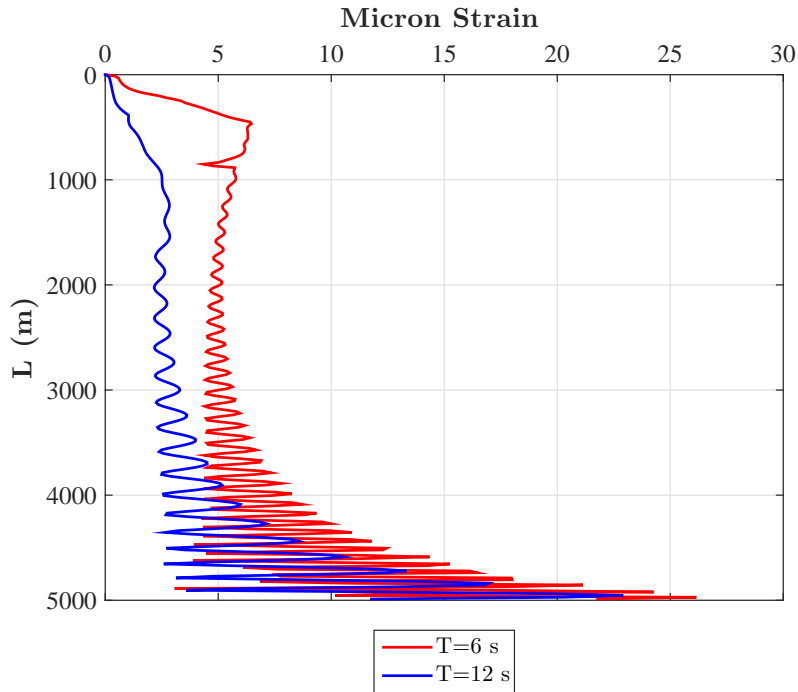


Figure 6.14 Strain along the riser (regular motion case with $A=2.5$ m)

The RMS A/D and the strains along the riser are presented in Figures 6.13 and 6.14 respectively. As expected the strains are maximum at the bottom of the riser where the variation in amplitude is quite high.

The fatigue damage is presented in Figure 6.15. The maximum fatigue damage occurs at the bottom of the riser. The minimum fatigue life in case of $T=6$ s is 111.4 years and $T=12$ s is 324.9 years.

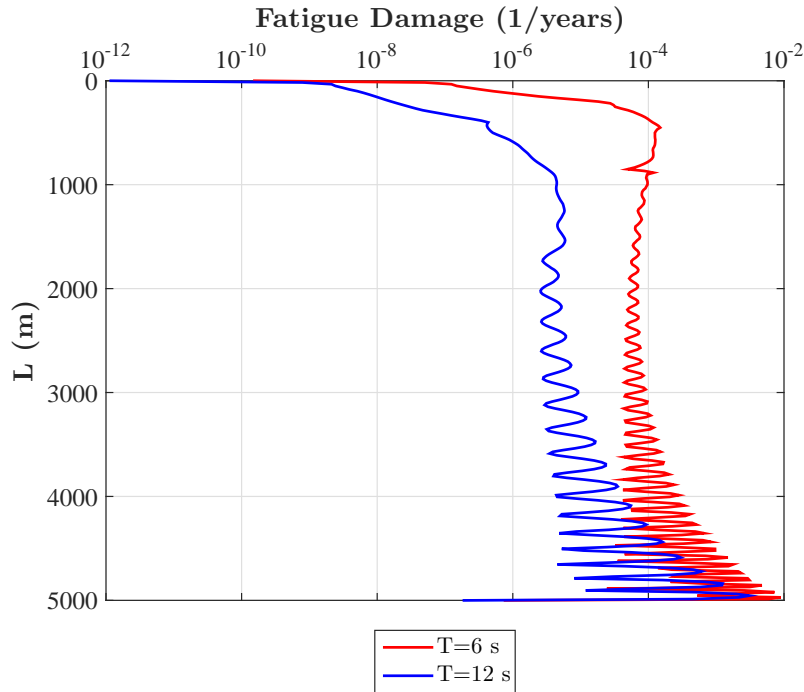


Figure 6.15 Fatigue damage along the riser (regular motion case with $A=2.5$ m)

6.4.3 Regular motion case with $A=5$ m

This case deals with harmonic motion with an amplitude of 5 m and periods of 10 s and 15 s. The top KC number in this case is 82.6. Table 6.4 summarizes the details of the vessel motion.

Table 6.4 Vessel motions for regular motion case with $A=5$ m

Amp (m)	T (s)	f (Hz)	KC_{top}
5	10	0.1	82.6
	15	0.067	

Figure 6.16 represents the equivalent current profiles for both the imposed motion frequencies. The KC number distribution is shown in Figure 6.17, in which it is clear that the representative KC number falls in the range of 32-40. Hence, we can select $N=5$ for this case from Table 3.1.

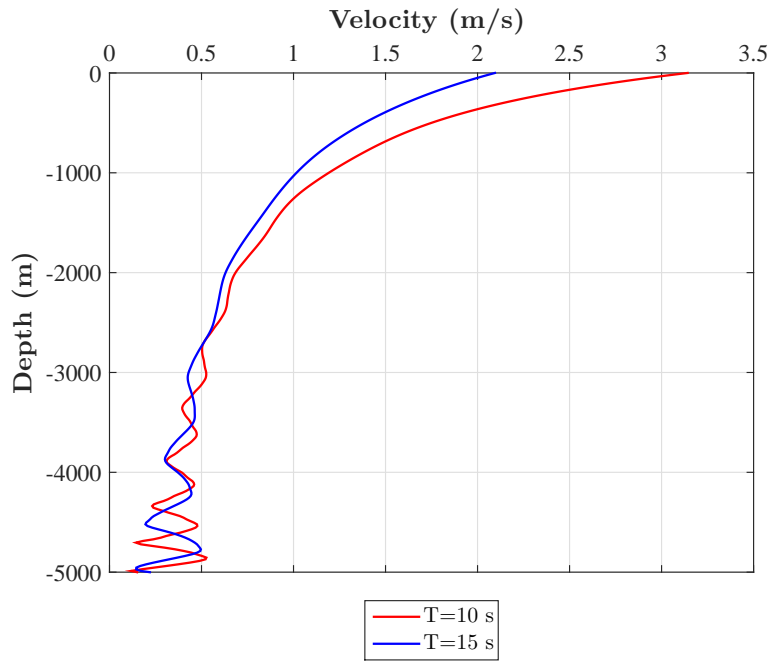


Figure 6.16 Equivalent current profile (regular motion case with $A=5$ m)

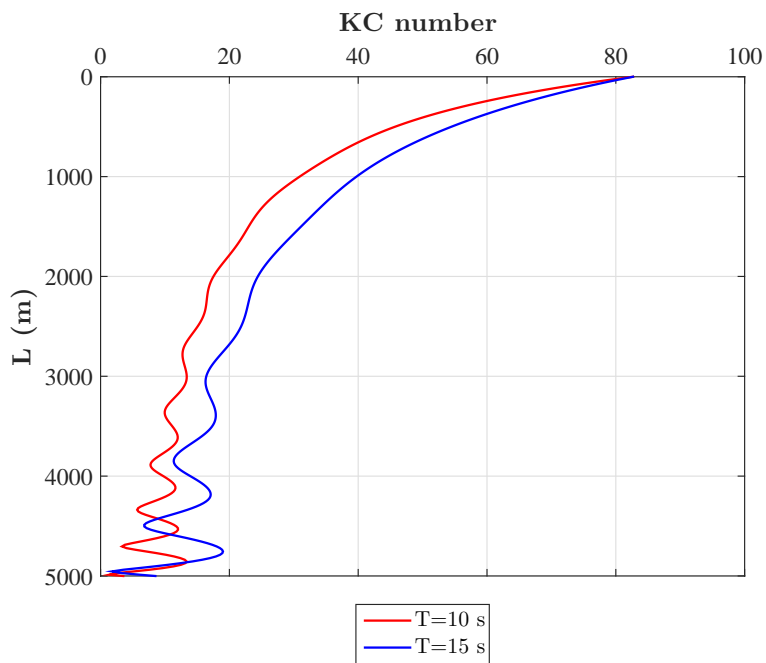


Figure 6.17 KC number distribution (regular motion case with $A=5$ m)

Applying Equation 3.1, we get:

For $T=10$ s, $f_{resp} = 0.5$ Hz, and

For $T=15$ s, $f_{resp} = 0.33$ Hz

The value of St^* calculated for the response is 0.09 in this case study.

Figure 6.18 shows the excitation frequencies along the riser. Drastically reducing current profiles in this case results in the dominant frequency to be present only on the top portion of the riser.

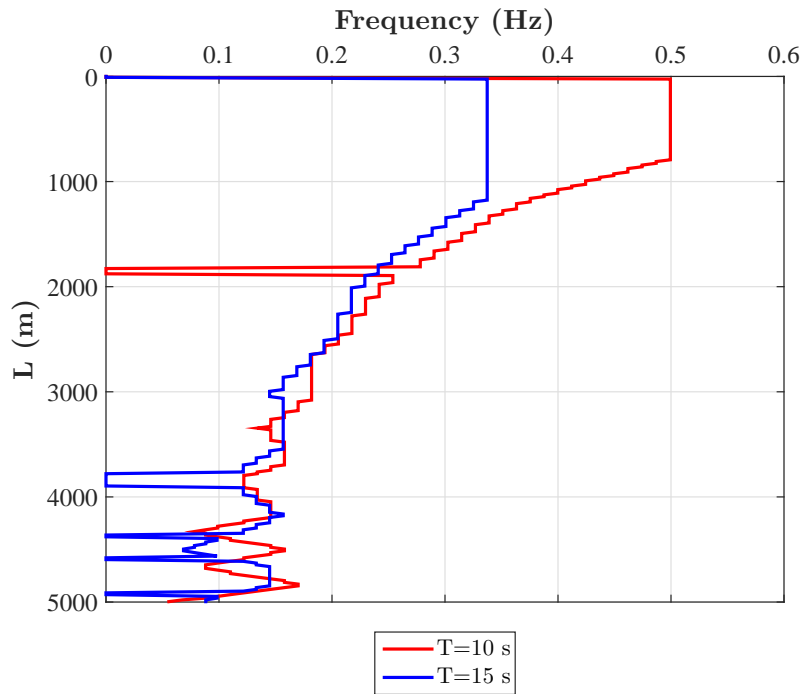


Figure 6.18 Excitation frequencies (regular motion case with $A=5$ m)

The RMS A/D and the strains along the riser are shown in Figures 6.19 and 6.20 respectively. It can be seen that the maximum values of RMS A/D for both the motion frequencies have their maxima at the top part of the riser. The variation in vibration amplitude is quite large at the bottom which results in large stresses and thus large strains at the bottom.

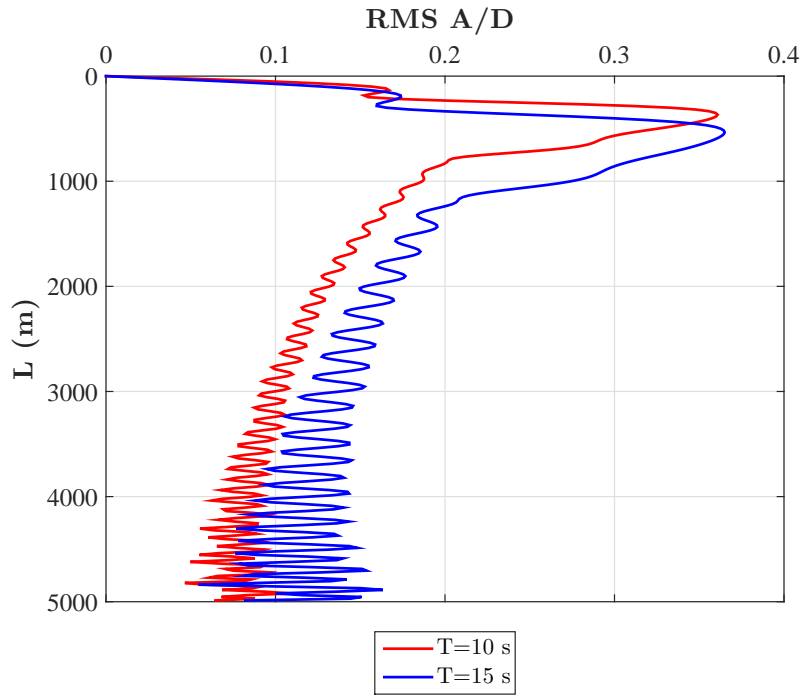


Figure 6.19 RMS A/D along the riser (regular motion case with $A=5$ m)

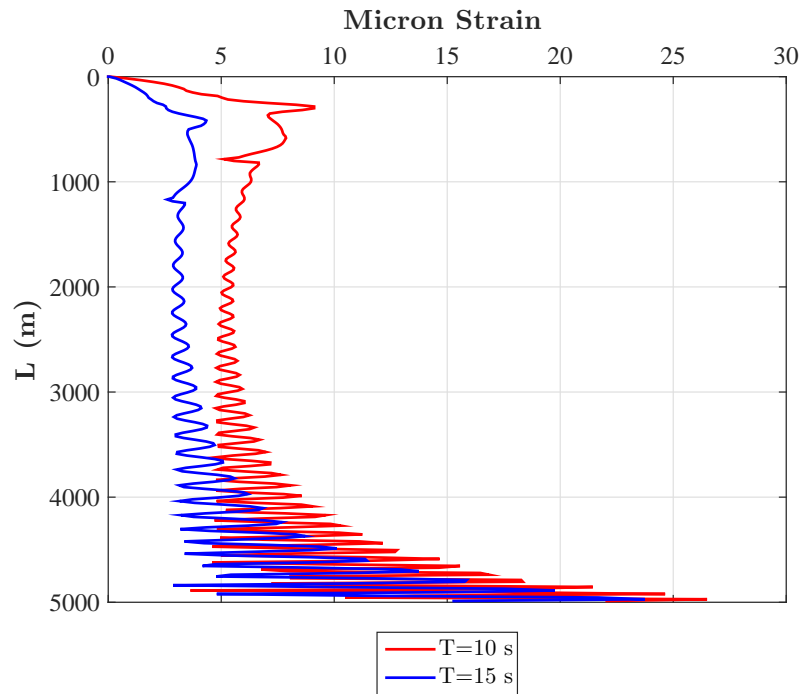


Figure 6.20 Strain along the riser (regular motion case with $A=5$ m)

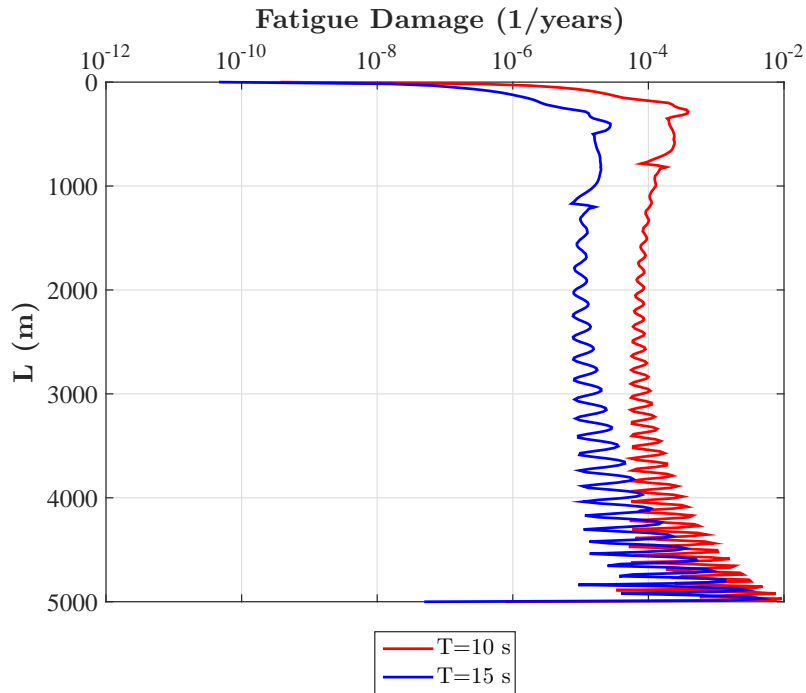


Figure 6.21 Fatigue damage along the riser (regular motion case with $A=5$ m)

The fatigue damage is presented in Figure 6.21. The maximum damage occur at the free bottom portion of the riser where the stresses are higher. The minimum fatigue life is 107.5 years for $T=10$ s and 215.93 years for $T=15$ s.

6.4.4 Irregular motion case

In this case study, an irregular vessel motion is considered. Typically, the vessel drifts are of low frequency irregular motions. Focus is given on low KC number case and hence we consider a motion with smaller amplitude. Figure 6.22 shows the displacement spectrum of the irregular motion. The peak frequency of the motion is 0.0105 Hz ($T=95$ s).

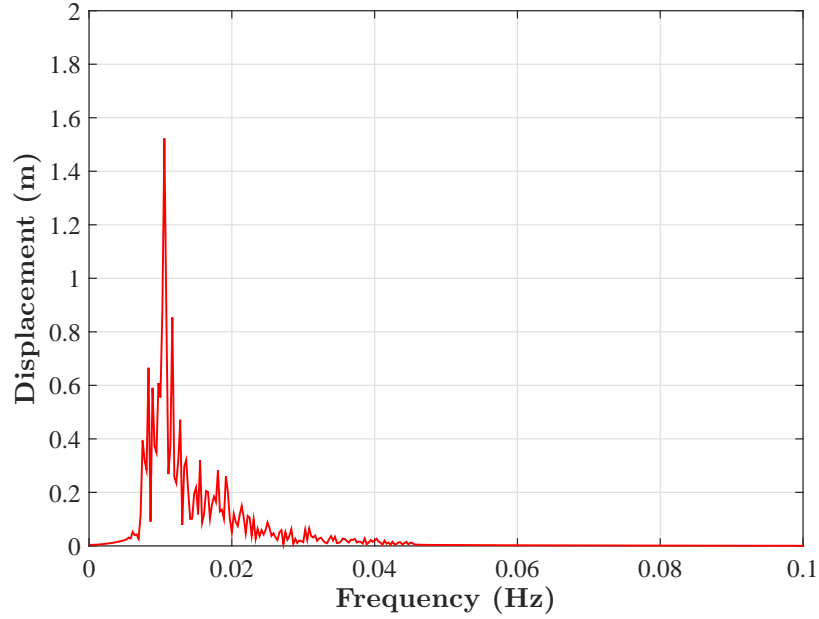


Figure 6.22 Displacement spectrum of the vessel motion (irregular motion case)

The equivalent current profile due to the motion is presented in Figure 6.23. As this is a low amplitude motion with a low frequency, the velocities are quite low as expected. The bottom part of the riser, which is free to move, have a velocity similar in magnitude to the top. This is also a consequence of the low amplitude low frequency motion.

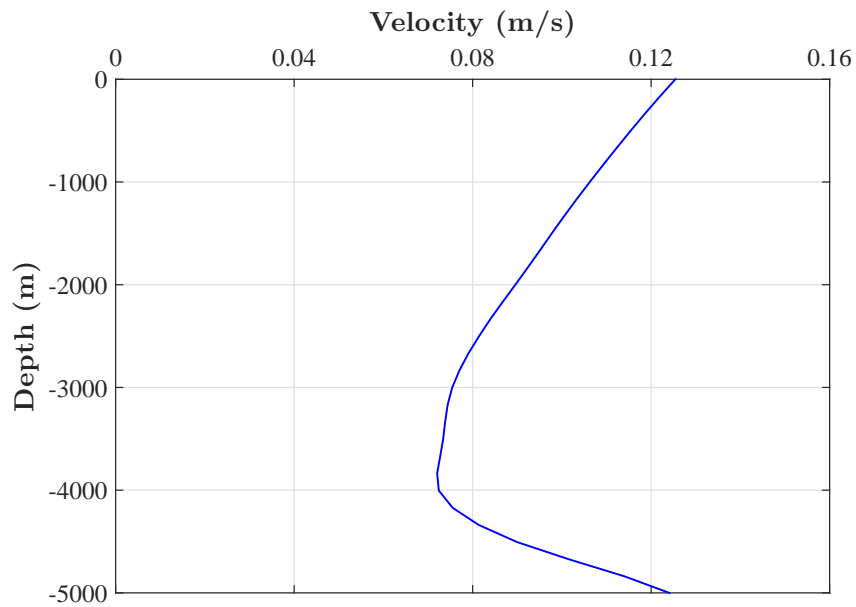


Figure 6.23 Equivalent current profile (irregular motion case)

The KC number distribution is shown in Figure 6.24. The representative KC can be taken as 24 which gives $N=4$. Hence, the f_{resp} is estimated to be 0.0422 Hz.

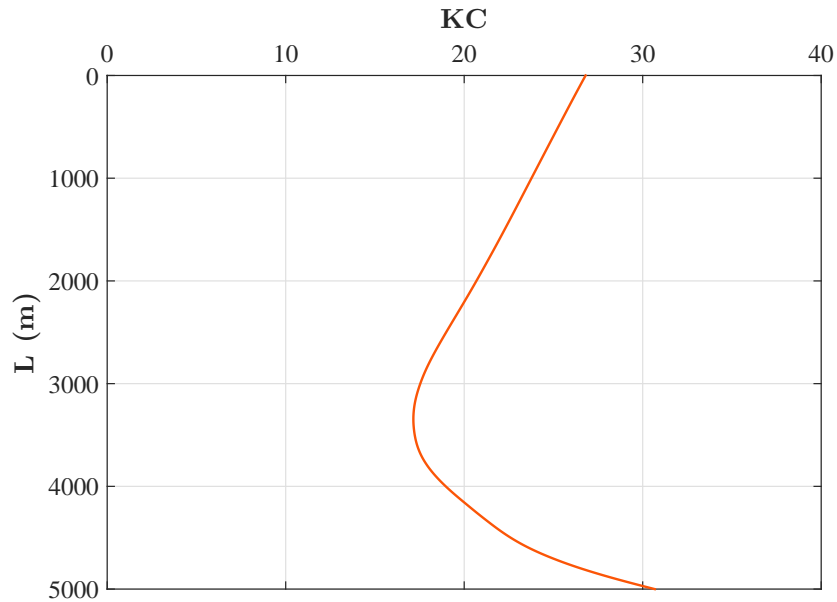


Figure 6.24 The KC number distribution along the riser (irregular motion case)

Figure 6.25 shows the response frequency along the riser. It can be seen that there is only one frequency excited along the whole length of the riser. This frequency, 0.048 Hz, is similar to the estimated f_{resp} and belongs to 5th mode of the riser. Since the velocity of equivalent current is quite low, the vortex shedding frequency is also low and resulted in the excitation of a lower mode.

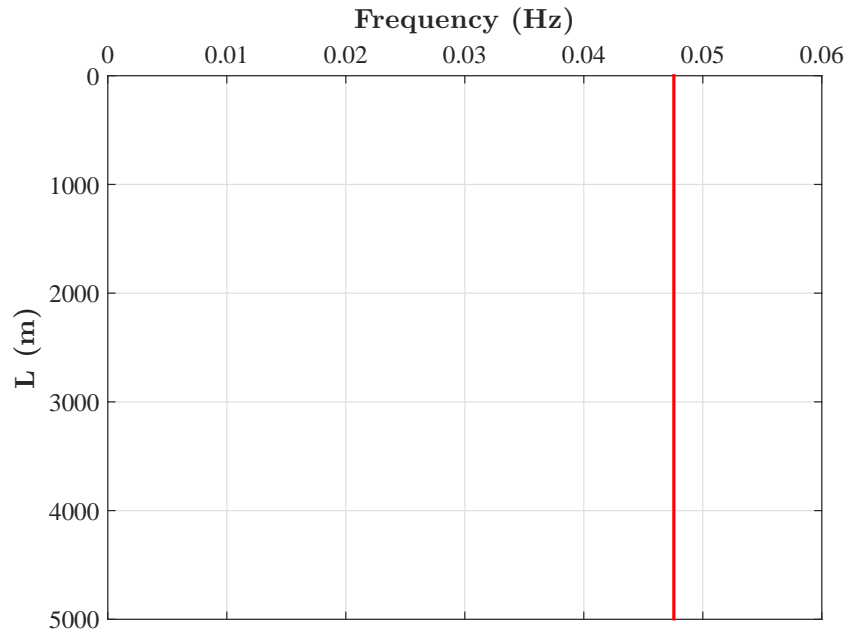


Figure 6.25 Excitation frequency along the riser (irregular motion case)

The RMS A/D and the strains along the riser are presented in Figures 6.26 and 6.27. The strains are very low in this case due to the curvature being very small. Still the maximum strain occurs at the bottom part which is free to move.

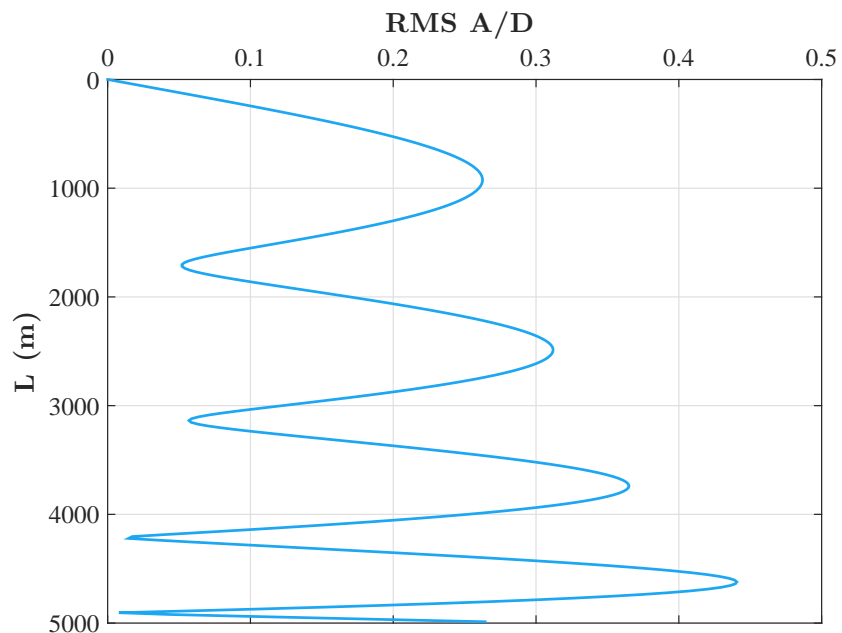


Figure 6.26 RMS A/D along the riser (irregular motion case)

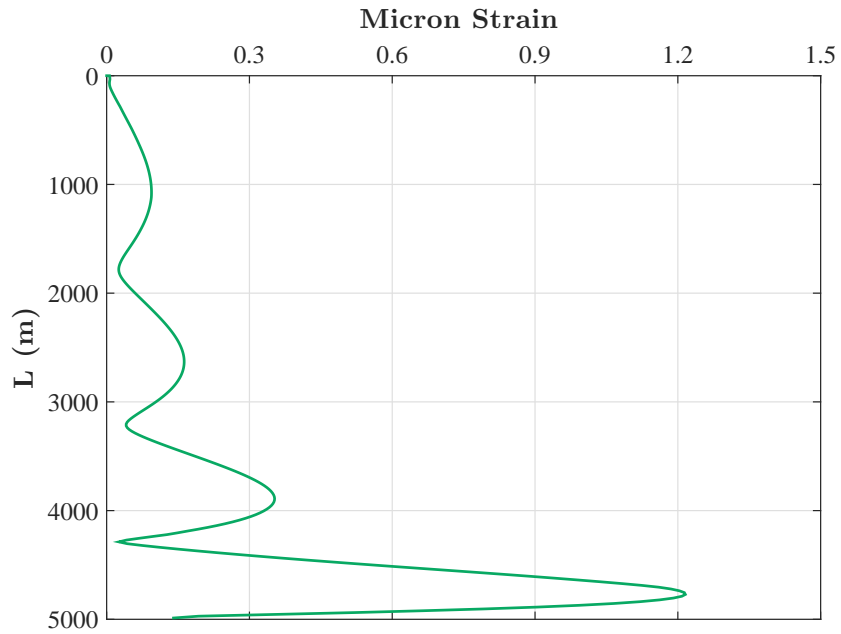


Figure 6.27 Strain along the riser (irregular motion case)

Figure 6.28 shows the fatigue damage along the riser and it can be seen that the damage is very small. The fatigue life of the riser in this case is quite high owing to the smaller stresses in the riser. The minimum fatigue life in this case is 1.15×10^7 .

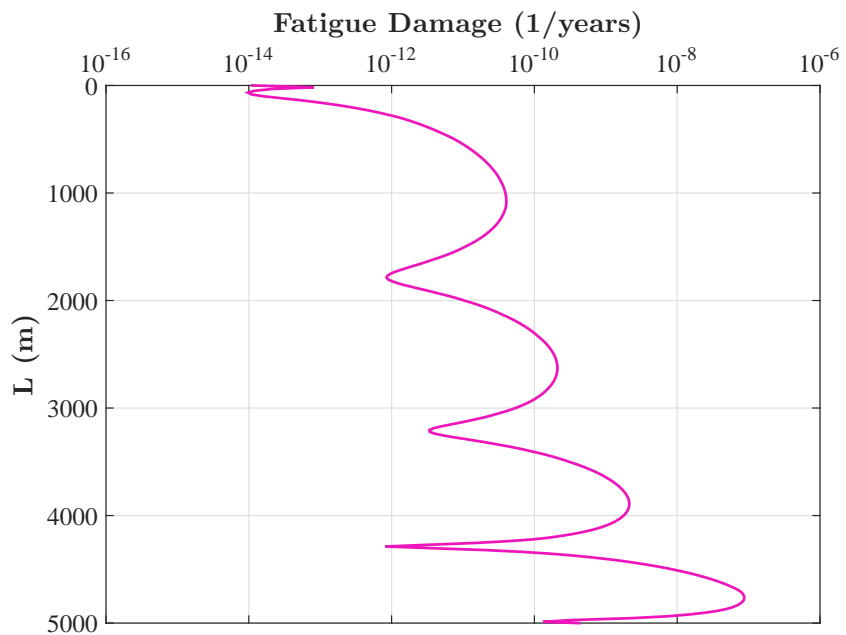


Figure 6.28 Fatigue damage along the riser (irregular motion case)

6.4.5 Current-induced VIV case

In current-induced VIV case, the VIV due to pure ocean current is investigated. The typical current data pertaining to the Pacific Ocean is obtained from the archives of National Oceanographic Data Center (NODC, 2016). The data contains current velocities measured by ship mounted ADCPs. From the data, the sample with maximum current velocities has been selected for the purpose of this analysis. Figure 6.29 shows the ocean current profile.

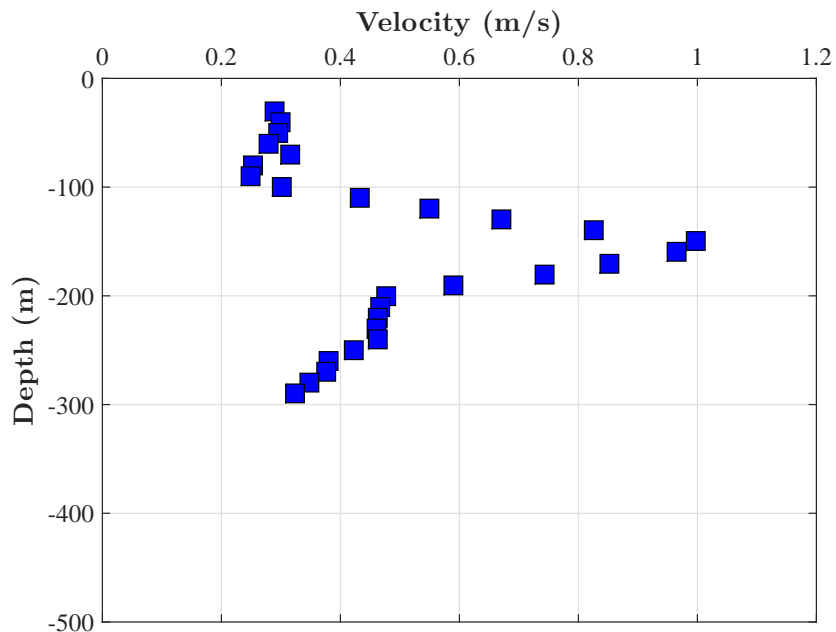


Figure 6.29 Ocean current profile (current-induced VIV case)

The VIV due to the current is analysed in VIVANA to obtain the response. Figure 6.30 shows the excitation frequencies along the riser because of the vortex shedding due to the current flow. The ocean current is heavily sheared and reduces to negligible velocity as we go deeper. Hence, the top part of the riser experience higher frequencies whereas the lower part is excited by very low frequencies.

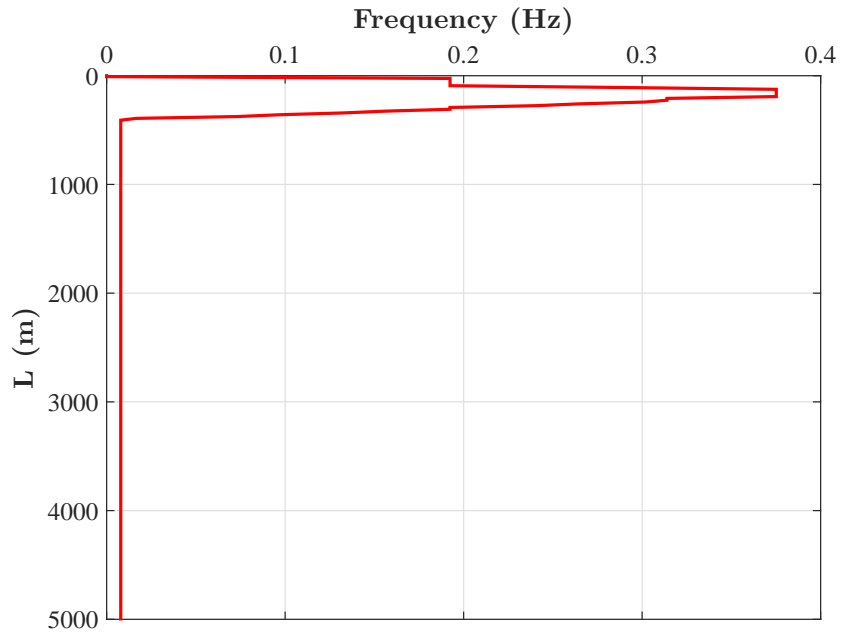


Figure 6.30 Excitation frequencies along the riser (current-induced VIV case)

The strain values are plotted in Figure 6.31. The strain on the riser are quite small owing to the vibration at very low modes in the current. Low strain results in a very high fatigue life for the riser. The minimum fatigue life for the riser is 89248 years. The fatigue damage is presented in Figure 6.32.

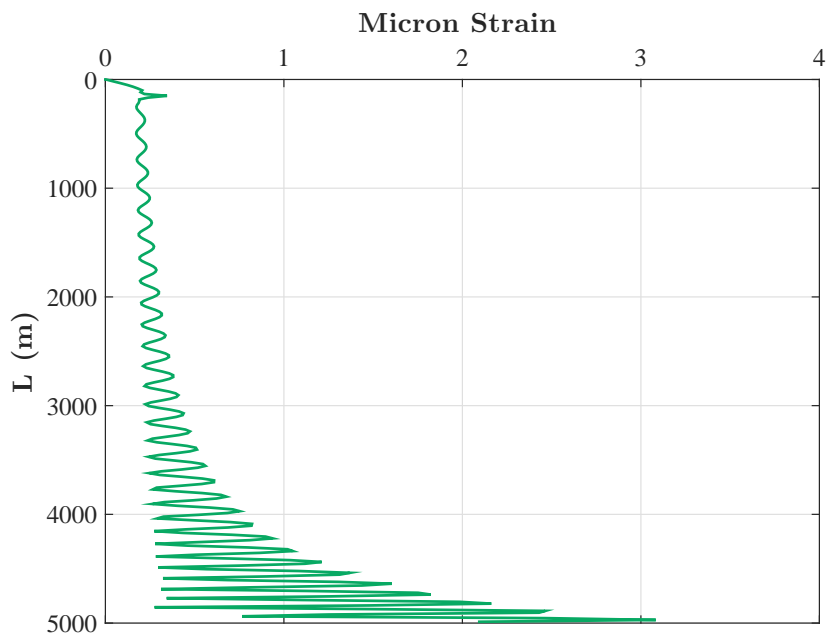


Figure 6.31 Strain along the riser (current-induced VIV case)

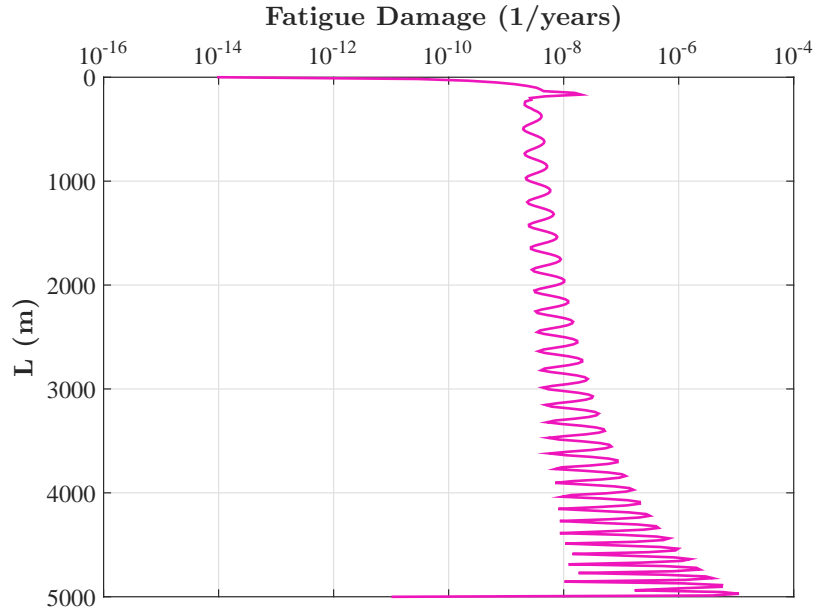


Figure 6.32 Fatigue damage along the riser (current-induced VIV case)

6.5 Discussion

In this chapter, various cases of low KC vessel motions were considered and the behaviour of the deep sea mining riser with regard to the VIV was investigated. The high frequency motions were found to excite very high modes of vibrations.

A comparison of the case studies are presented in Table 6.5.

Table 6.5 Comparison of case studies

Sl. No.	Type	Amp (m)	T (s)	f (Hz)	KC range	N	f_{resp}	Mode	Min. fatigue life (years)
1	Regular motion	1.5	6	0.166	7-15	2	0.33	29	117.7
			12	0.0833			0.17	15	1603.1
2.5		6	0.166	15-24	3	0.5	42	111.4	
		12	0.0833			0.25	22	324.9	
3		5	10	0.1	32-40	5	0.5	42	107.05
			15	0.0667			0.33	29	215.93
4	Irregular motion	5 (max)	95	0.105	24	4	0.0422	5	1.15×10^7
5	Current	-	-	-	-	-	0.375	32	89248

When comparing the fatigue life from various cases, it can be seen that the high frequency vessel motion-induced VIV can cause considerable fatigue damage to the riser. The minimum fatigue life in the first three case studies is very low when compared to the current-induced VIV. This implies that the possibility of such motions could cause considerable damage to the riser and hence should be taken into consideration during design and operation. It can also be seen that the low frequency motion at low KC numbers causes quite minimal damage to the riser. The capability of the mooring system/dynamic positioning system decides to an extent the motion of the vessel. Hence, from an operational point of view it is important to limit the amplitude and the frequency of vessel drift in order to reduce the effects of VIV on the riser.

Chapter 7

Conclusions

Vortex Induced Vibration is a major concern for a riser exposed to a current flow. It can cause fatigue in the riser and lead to its failure. Studies have pointed out that the vessel motion can also induce VIV which can be of the same magnitude as that caused by the current flow. Hence, it is important that the VIV is identified for the riser and mitigation measures taken to suppress VIV.

An empirical model was proposed to predict the VIV of a riser due to vessel motions and was validated. From the experimental results from the small-scale riser model tests, it was possible to validate the numerical model. Of special interest were the cases with low KC numbers, where the frequency of response depends on the frequency of imposed motion. The validation provided good results with the model being able to predict the response frequencies accurately. The strain values were difficult to match as those were influenced by the actual structural damping and measurement errors. Despite of this, good comparisons were obtained for several of the cases.

The data obtained from the measurements of an actual full-scale drilling riser was analysed and in some cases vessel motion-induced VIV was identified. The proposed model was validated against these results and provided useful insights into the VIV behaviour of a full-scale riser under vessel motion. The results of the validation studies provided confidence in extending the numerical model to analyse the 5,000 m deep sea mining riser.

The analysis of the riser provided good insights into the behavior of such a long riser under pure vessel motions of low KC numbers. A long riser with many natural frequencies can lock-on to shedding frequencies due to a wide range of current velocities. The stresses and strains at the bottom are high which results in large fatigue damage and hence measures to suppress VIV are required. VIV suppression devices like helical strakes, fairings or perforated shrouds should be installed to avoid vortex shedding behind the riser. The VIV due to ocean current was also investigated and compared with the vessel motion-induced VIV. It should be noted that the configuration of the present investigated riser is similar to a disconnected drilling riser or a free-hanging water intake riser. Hence, the present study can be extended to other application areas as well.

A further study should address the coupled analysis of the support vessel - vertical riser system in order to predict the global motions of the riser accurately. This will be an area of interest for future work. Furthermore, axial resonance, which is expected for the riser at the wave frequency range, can be investigated.

Bibliography

- Berndt, R. (2015). The Solwara 1 deepwater mining project. In *Third International Future Mining Conference*.
- BP and 2H Offshore (2008). VIV benchmarking repository–drilling riser without VIV suppression. Technical report, DATA PACKAGE TECHNICAL NOTE.
- Chung, J. S. (2010). Full-scale, coupled ship and pipe motions measured in North Pacific Ocean: The Hughes Glomar Explorer with a 5,000-m long heavy-lift pipe deployed. *International Journal of Offshore and Polar Engineering*, 20(1):1–6.
- Chung, J. S., Cheng, B. R., and Huttelmaier, H. P. (1994). Three-dimensional coupled responses of a vertical deep-ocean pipe: Part II. excitation at pipe top and external torsion. *International Journal of Offshore and Polar Engineering*, 4(4).
- Chung, J. S. and Tsurusaki, K. (1994). Advance in deep-ocean mining systems research. *Proceedings of the 4th International Offshore and Polar Engineering Conference. Osaka*.
- Cunff, C. L., Biolley, F., and Damy, G. (2005). Experimental and numerical study of heave-induced lateral motion (HILM). In *Proceedings of the 24th International Conference on Offshore Mechanics and Arctic Engineering, Halkidiki*.
- DNV RP C203 (2010). Fatigue design of offshore steel structures. Technical report, Det Norske Veritas.
- Fernandes, A. C., Mirzaeisefat, S., and Cascão, L. V. (2014). Fundamental behaviour of vortex self induced vibration (VSIV). *Applied Ocean Research*, 47:183–191.
- Goharzadeh, A. and Molki, A. (2014). Measurement of fluid velocity development behind

- a circular cylinder using particle image velocimetry (PIV). *European Journal of Physics*, 36(1).
- Gonzalez, E. C. (2001). *High frequency dynamic response of marine risers with application to flow-induced vibration*. PhD thesis, Massachusetts Institute of Technology.
- Gopalkrishnan, R. (1993). *Vortex-Induced Forces on Oscillating Bluff Cylinders*. PhD thesis, Department of OceanEngineering, MIT, Boston.
- Hoagland, P., Beaulieu, S., Tivey, M. A., Eggert, R. G., German, C., Glowka, L., and Lin, J. (2010). Deep-sea mining of seafloor massive sulfides. *Marine Policy*, 34(3):728 – 732.
- Kwon, Y. J., Kim, H. J., and Jung, D. H. (2015). A study for forced oscillation experiment for OTEC riser under current. In *Proceedings of the 25th International Ocean and Polar Engineering Conference, Kona, Big Island, Hawaii*.
- MARINTEK (2016). VIVANA 4.8.2 theory manual. Technical report, MARINTEK Report.
- Munson, D., Adams, T. M., and Hall, S. (2012). Determination of material damping values for high density polyethylene pipe materials. In *Proceedings of the ASME 2012 Pressure Vessels and Piping Conference, Toronto*.
- Natarajan, S., Howells, H., Deka, D., and Walters, D. (2006). Optimization of sensor placement to capture riser VIV response. In *Proceedings of the 25th International Conference on Offshore Mechanics and Arctic Engineering, Hamburg*.
- Nautilus Minerals (2016a). Retrieved 14th April 2016, from <http://www.nautilusminerals.com/irm/content/sms-information.aspx?RID=422>.
- Nautilus Minerals (2016b). Retrieved 16th April 2016, from <http://www.nautilusminerals.com/irm/content/how-it-will-all-work.aspx?RID=433>.
- NODC (2016). Joint archive for shipboard ADCP - online inventory. In *Retrieved from https://www.nodc.noaa.gov/General/adcp.html*.
- Rateiro, F., Goncalves, R. T., Pesce, C. P., Fujarra, A. L. C., Franzini, G. R., and Mendes, P. (2013). A model scale experimental investigation on vortex-self induced vibrations (VSIV)

- of catenary risers. In *Proceedings of the ASME 2013 32nd International Conference on Ocean, Offshore and Arctic Engineering, Nantes*.
- Sumer, M. B. and Fredsøe, J. (2006). *Hydrodynamics Around Cylindrical Structures*. World Scientific Publishing Company, revised edition.
- Thethi, R., Howells, H., Natarajan, S., and Bridge, C. (2005). A fatigue monitoring strategy and implementation on a deepwater top tensioned riser. In *Proceedings of 2005 Offshore Technology Conference, Houston*.
- Tognarelli, M. A., Taggart, S., and Campbell, M. (2008). Actual VIV fatigue response of full scale drilling risers: With and without suppression devices. In *Proceedings of the 27th International Conference on Offshore Mechanics & Arctic Engineering, Estoril*.
- Vedeld, K., Sollund, H., Fyrileiv, O., and Nestegård, A. (2016). A response model for vortex induced vibrations in low KC number flows. In *Proceedings of the ASME 2016 35th International Conference on Ocean, Offshore and Arctic Engineering, Busan*.
- Wang, J., Fu, S., Ong, M. C., and Li, H. (2016a). Experimental investigation on vortex-induced vibration of a free-hanging riser under vessel motion. In *Proceedings of the ASME 2016 35th International Conference on Ocean, Offshore and Arctic Engineering, Busan*.
- Wang, J., Jaiman, R. K., Adaikalaraj, P. F., Shen, L., Tan, S. B., and Wang, W. (2016b). Vortex-induced vibration of a free-hanging riser under irregular vessel motion. In *Proceedings of the ASME 2016 35th International Conference on Ocean, Offshore and Arctic Engineering, Busan*.
- Wang, J., Joseph, R. S., Ong, M. C., and Jakobsen, J. B. (2017). Numerical investigation on vessel motion-induced VIV for a free hanging riser under small Keulegan–Carpenter numbers. In *Proceedings of the ASME 2017 36th International Conference on Ocean, Offshore and Arctic Engineering, Trondheim*.
- Wang, J., Xiang, S., Fu, S., Cao, P., Yang, J., and He, J. (2016c). Experimental investigation on the dynamic responses of a free-hanging water intake riser under vessel motion. *Marine Structures*, 50:1–19.

Williamson, C. H. K. (1985). In-line response of a cylinder in oscillatory flow. *Applied Ocean Research*, 7(2):97–106.

Willis, N. R. T. and Thethi, K. S. (1999). Stride JIP: Steel risers in deepwater environments - progress summary. In *Proceedings of Offshore Technology Conference, Houston*.

Wu, J., Lie, H., Larsen, C. M., and Baarholm, R. J. (2015). An empirical heave induced VIV prediction model. In *Proceedings of the ASME 2015 34th International Conference on Ocean, Offshore and Arctic Engineering, St. John's, Newfoundland*.

Appendix A

Small-scale Riser Model Tests: Comparison of Eigen Frequencies

Table A.1 shows the comparison of eigen frequencies calculated from VIVANA and the ones obtained from the experimental analysis of Wang et al. (2016c) for the first 6 eigen modes for the Water Intake Riser.

Table A.1 Comparison of Eigen frequencies

Eigen mode	From VIVANA		From the literature (Wang et al., 2016c)	
	Time period (s)	Frequency (Hz)	Time period (s)	Frequency (Hz)
1	75.18	0.0133	62.5	0.016
2	20.74	0.048	17.24	0.058
3	8.4	0.119	7.69	0.13
4	4.33	0.23	4.16	0.24
5	2.61	0.383	2.5	0.4
6	1.73	0.577	1.667	0.6

Table A.2 shows the comparison of eigen frequencies calculated from VIVANA and the ones obtained from the experimental analysis of Wang et al. (2016a) for the first 7 eigen modes for the Free-hanging riser.

Table A.2 Comparison of Eigen frequencies

Eigen mode	From VIVANA		From the literature (Wang et al., 2016a)	
	Time period (s)	Frequency (Hz)	Time period (s)	Frequency (Hz)
1	6.04	0.1656	6.25	0.1600
2	1.83	0.5464	1.79	0.5600
3	0.90	1.1094	0.76	1.3100
4	0.55	1.817	0.53	1.8900
5	0.37	2.7382	0.35	2.8700
6	0.26	3.8684	0.25	4.0700
7	0.19	5.2036	0.18	5.4900

Appendix B

Modelling of Drilling Riser

The dimensions and weights of the drilling riser stack-up are given in Table B.1. The dry weight and submerged weight of the riser provided along with the dataset (BP and 2H Offshore, 2008) are important parameters to be taken into account during the modelling of the riser in RIFLEX. The submerged weight and buoyancy determines the tension along the riser and the dry weight distribution determines the vibration response.

The riser was modelled in RIFLEX taking into account both the dry weight and submerged weight. The weight parameter input given in RIFLEX is the unit dry weight of the riser. The external area input of the cross-section was determined such that the resulting buoyancy is in accordance with the submerged weight provided in the dataset.

The properties of the riser flex joints are given in Table B.2.

Table B.1 Riser dimensions and weights

Item	L (m)	Stress diameter (m)	Thickness (m)	Hydrodynamic diameter (m)	Unit dry wt. (kg/m)	Unit submerged wt. (kg/m)
Diverter	4.1	0.5334	0.02	0.5334	3114.72	0.00
16.7 ft Pup	5.1	0.5334	0.02	0.5334	706.76	614.88
Inner barrel	9.2	0.5334	0.02	0.5334	787.95	0.00
Outer barrel	30.4	0.6604	0.04	0.6604	863.10	750.89
Intermediate FJ	2.8	1.1938	0.35	1.1938	1904.01	1656.52
Termination joint	17.3	0.5334	0.02	0.5334	735.95	640.28
5 ft pup	1.5	0.5334	0.02	0.5334	1391.46	1210.49
20 ft pup	6.1	0.5334	0.02	0.5334	740.75	644.46
40 ft pup	12.2	0.5334	0.02	0.8636	614.44	534.56
BUOY3000	548.6	0.5334	0.02	1.2827	861.72	17.62
BUOY4000	228.6	0.5334	0.02	1.3081	904.98	27.54
BUOY5000	274.3	0.5334	0.02	1.3335	957.82	15.04
Slick	594.5	0.5334	0.02	0.8636	586.74	510.47
Lower FJ	2.7	1.4732	0.49	1.4732	2485.25	933.04
LMRP	3.4	5.6515	2.58	5.6515	29495.64	25661.20
BOP	7.2	5.6515	0.02	5.6515	26597.42	23139.76
Wellhead	4.4	0.9652	0.06	0.9652	1854.08	1613.09

Table B.2 Properties of riser Flex Joints (BP and 2H Offshore, 2008)

Item	Dry weight (kg)	Rotation stiffness (Nm/deg)	Submerged weight (kg)
Lower FJ	-	105690	2531.09
Intermediate FJ	5356.56	18970	4660.29
Upper FJ	8762.64	21680	-

Appendix C

Hydrodynamic Coefficients used for Deep Sea Mining Riser

The drag coefficient C_D and added mass coefficient C_a used for the model are as follows

▼ Hydrodynamic force coefficients

Input code:

Froude Krylov scaling:

Hydrodynamic diameter:

Quadratic drag coefficients: Linear drag coefficients:

CQx	CQy
0.0	1.2

CLx	CLy
0.0	0.0

Added mass coefficients:

CAx	CAy
0.0	1.0

Appendix D

MATLAB Codes for Acceleration Data Analysis

D.1 Low pass filter

```
1 function [yfilt,filtb,filta] = filter1(filtertype,y,varargin)
2 % filter1 performs frequency or wavelength filtering on a 1D array
3 % using zero-phase Butterworth filtering.
4 %
5 %% Syntax
6 %
7 % yfilt = filter1(filtertype,y,'fc',Fc)
8 % yfilt = filter1(filtertype,y,'lambdac',lambdac)
9 % yfilt = filter1(...,'fs',Fs)
10 % yfilt = filter1(...,'x',x)
11 % yfilt = filter1(...,'Ts',Ts)
12 % yfilt = filter1(...,'order',FilterOrder)
13 % [yfilt,filtb,filta] = filter1(...)
14 %
15 %% Description
16 %
17 % yfilt = filter1(filtertype,y,'fc',Fc) filters 1D signal y
18 % using a specified filtertype and cutoff frequency Fc. For
19 % high-pass or low-pass filters Fc must be a scalar. For band-
20 % pass and band-stop filters Fc must be a two-element array. The
21 % filtertype can be
22 %
```

```

23 % * 'hp' high-pass with scalar cutoff frequency Fc
24 % * 'lp' low-pass with scalar cutoff frequency Fc
25 % * 'bp' band-pass with two-element cutoff frequencies Fc
26 % * 'bs' band-stop with two-element cutoff frequencies Fc
27 %
28 % yfilt = filter1(filtertype,y,'lambdac',lambdac) specifies cutoff
29 % wavelength(s) rather than cutoff frequencies. This syntax assumes
30 % lambda = 1/f.
31 %
32 % yfilt = filter1(...,'fs',Fs) specifies a sampling frequency Fs.
33 % If neither 'fs', 'x', nor 'Ts' are specified, Fs = 1 is assumed.
34 %
35 % yfilt = filter1(...,'x',x) specifies a vector of monotonically-
36 % increasing, equally-spaced sampling times or x locations corresponding
37 % to y, which is used to determine sampling frequency. If neither 'fs',
38 % 'x', nor 'Ts' are specified, Fs = 1 is assumed.
39 %
40 % yfilt = filter1(...,'Ts',Ts) specifies a sampling period or sampling distance
41 % such that Fs = 1/Ts. If neither 'fs', 'x', nor 'Ts' are specified,
42 % Fs = 1 is assumed.
43 %
44 % yfilt = filter1(...,'order',FilterOrder) specifies the order (sometimes
45 % called rolloff) of the Butterworth filter. If unspecified, FilterOrder = 1 is assumed.
46 %
47 % [yfilt,filtb,filta] = filter1(...) also returns the filter numerator
48 % filta and denominator filtb.
49 %
50 %% Author Info
51 % The filter1 function was written by Chad A. Greene of the University of
52 % Texas at Austin's Institute for Geophysics (UTIG), October 2015.
53 % http://www.chadagreene.com
54 %
55 % See also butter and filtfilt.
56
57 %% Initial error checks:
58
59 assert(license('test','signal_toolbox')==1,'The filter1 function requires Matlab's Signal
    Processing Toolbox.')
60 assert(nargin>3,'Not enough input arguments.')
61 assert(sum(strcmpi({'hp';'lp';'bp';'bs';'high';'low';'bandpass';'stop'},filtertype))==1,'
    Filter type must be 'hp', 'lp', or 'bp'.'),
62 assert(sum([strcmpi(varargin,'fc') strcmpi(varargin,'lambdac')])==1,'Must declare a cutoff
    frequency (or frequencies) 'fc', or cutoff wavelength(s) 'lambdac'.')
63 assert(isvector(y)==1,'Input y must be a vector.')
64

```

```

65 %% Define defaults:
66
67 order = 1;
68 Fs = 1;
69
70 %% Parse Inputs:
71
72 % Replace filtertype string if necessary:
73 filtertype = strrep(filtertype, 'hp', 'high');
74 filtertype = strrep(filtertype, 'lp', 'low');
75 filtertype = strrep(filtertype, 'bp', 'bandpass');
76 filtertype = strrep(filtertype, 'bs', 'stop');
77
78 % Is a sampling frequency defined?
79 tmp = strcmpi(varargin, 'fs');
80 if any(tmp)
81     Fs = varargin{find(tmp)+1};
82 end
83
84 % Define sampling period:
85 tmp2 = strcmp(varargin, 'Ts');
86 if any(tmp2)
87     Fs = 1/varargin{find(tmp2)+1};
88 end
89
90 % Define sampling vector:
91 tmp3 = strcmp(varargin, 'x');
92 if any(tmp3)
93     x = varargin{find(tmp3)+1};
94     assert(isvector(x)==1, 'Input x must be a vector.')
95     assert(length(x)==length(y), 'Dimensions of input vector x must match dimensions of input
          signal vector y.')
96
97     Ts = unique(diff(x));
98     assert(all([isscalar(Ts) isfinite(Ts)])==1, 'Input vector x must be equally spaced.')
99     Fs = 1/Ts;
100 end
101
102 % Make sure user didn't try to define a sampling frequency AND a sampling period:
103 assert(any(tmp)+any(tmp2)+any(tmp3)<2, 'I am confused. It looks like you have attempted to
          define a sampling frequency and a sampling period. Check inputs of filter1.')
104
105
106 % Cutoff Frequency:
107 tmp = strcmpi(varargin, 'fc');

```

```

108 if any(tmp)
109     cutoff_freqs = varargin{find(tmp)+1};
110 end
111
112 tmp2 = strncmpi(varargin,'lambdac',4);
113 if any(tmp2)
114     cutoff_freqs = 1./varargin{find(tmp2)+1};
115 end
116 assert(any(tmp)+any(tmp2)<2,'I am confused. It looks like you have attempted to define a
        cutoff frequency and a cutoff period. Check inputs of filter1.')
```

```

117
118 % Filter order:
119 tmp = strncmpi(varargin,'order',3);
120 if any(tmp)
121     order = varargin{find(tmp)+1};
122 end
123
124 %% Error checks on inputs:
125
126 assert(isscalar(Fs)==1,'Input error: Undefined sampling frequency or period.')
```

```

127
128 switch filtertype
129     case {'low','high'}
130         assert(isscalar(cutoff_freqs)==1,'Low-pass and High-pass filters require a scalar
                cutoff frequency.')
```

```

131
132     case {'stop','bandpass'}
133         assert(numel(cutoff_freqs)==2,'Bandpass and bandstop filters require a low and high
                frequency.')
```

```

134         cutoff_freqs = sort(cutoff_freqs);
135
136     otherwise
137         error('Unrecognized filter type.')
```

```

138 end
139
140 %% Construct filter:
141
142 nyquist_freq = Fs/2;           % Nyquist frequency
143 Wn=cutoff_freqs/nyquist_freq; % non-dimensional frequency
144 [filtb,filta]=butter(order,Wn,filtertype); % construct the filter
145 yfilt=filtfilt(filtb,filta,y); % filter the data with zero phase
146
147 end
```


D.2 Fast Fourier Transform

```
1 function [fre_plot,amp_plot]=fft_total(input,fs)
2
3 [m,n]=size(input);
4 N=n;
5 m=round(m/2)*2;
6
7
8 for i=1:m
9     fre(i)=i*fs/m;
10 end
11
12 fre1=fre(1:m/2+1);
13 CF=zeros(m/2+1,N);
14 for i=1:N;
15 CF1=fft(input(:,i),m);
16 CF(:,i)=CF1(1:m/2+1)/(m/2+1);
17 magCF(:,i)=abs(CF(:,i));
18 angleCF(:,i)=angle(CF(:,i))/pi*180;
19 end
20
21 if N==1
22     mag_total=magCF;
23 else
24     mag_total=sum(magCF');
25 end
26
27 fre_plot=fre1(1:round(m/2));
28 amp_plot=mag_total(1:round(m/2));
```


Appendix E

Full-scale Measurement Data Logger Specifications

The specifications of the data logger used for the full-scale measurements (BP and 2H Offshore, 2008) are provided in the following pages.

INTEGRIPod™ -M Specifications



Overview

The 2H **INTEGRIPod™ -M** is a standalone motion monitoring system. It allows movement of a structure to be recorded in its on-board memory over a long period of time (see examples). Data is downloaded into a computer for subsequent post data processing. The basic measurement includes:

- Tri axial acceleration (basic model)
- Tri plane angular rate (optional model)

From the measurements, various other parameters can be derived:

- Linear displacement
- Acceleration due to motion
- Average Inclination
- Harmonics

Deployment of loggers

The data logger contains all electronics, batteries and sensors enclosed in a cylindrical casing. After initialization using a computer, loggers can be deployed to the designated locations. This may simply involve strapping directly to the structure using bands or design of tailor-made interfaces to suit (available for diver or ROV operation for subsea use).

Mounting method

Strapped using suitable bands
Retrofit ROV friendly cradles



Cradle options

Strapped, bolted, magnetic holder

Analogue signal inputs

Number of inputs	8 Maximum
Input range	0 – 2.5V
Accuracy / resolution	0.0012v/0.0006V

Memory disk reader

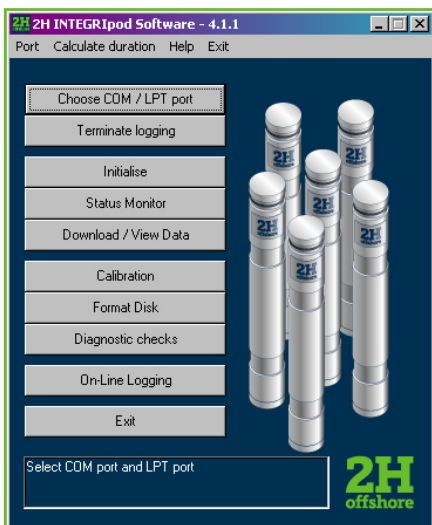
Communication	Centronic (parallel) port
Case size	80mm x 140mm x 40mm
Case material	ABS
Power	PP3 9V batteries
Supply Current	2mA maximum

Format of downloaded data files

Downloaded files	Time stamp files Data records for each session Compatible with Excel
Time stamp file	ASCII format
Data record file	ASCII format, Raw voltages for all sensors inputs

Maximum logging periods (examples)

Continuous logging @ 50Hz	50 days
Continuous logging @ 10Hz	25 days
10 minute logging every 0.5 hours @10Hz	75 days



Specification

G Sensors

Sensor direction	X, Y and Z
Range (g)	± 1.2 and ± 2
Cut-off response	4.5 Hz or configurable
Accuracy	±0.002 rms with 1.2g range
AC temp effect	No measurable effect
DC temp drift	Calibration can be provided
Alignment error	0.3 deg between axis
Sensor-X direction	Indicated on the logger body
Sensor calibration	Use gravity (1g and -1g)

Angular rate sensors

Sensing direction	X-Z, Y-Z and X-Y
Range	+/- 10 deg/s (nominal)
Cut-off response	10Hz
Accuracy	+/- 0.05 deg/s rms
Alignment error	0.3 deg

Data recording frequency

Record frequency [Hz]	30, 20, 15, 10, 5, & 2 150 Hz on special request < +/- 0.5% of the frequency error
-----------------------	---

Logging programme

Logging mode	Continuous and intermittent
In intermittent mode	
Log on period (min)	1, 10, 15, 20, 30
Cycle period (hour)	0.5, 1, 1.5, 2, 2.5, 3, 4, 5, 6

Communication ports

Port	RS232 port
Connection method	Standard RS232 cable

On-board memory

Memory media	128 Mb memory (standard) -needs formatting by reader
--------------	---

Software

Operating system	Win95, 98, 2000, NT, XP,
Functions	-Diagnostic check of loggers -Initialise loggers -Download data from loggers -On-line logging -Battery/memory life calculation

Power supply

Batteries	2 D-size 3.6V lithium
Battery capacity	13,500mA-hour nominal
Current (logging)	11-42mA (different sensors)
Standby	3mA maximum

Casing

Material	Superduplex stainless steel
Size [mm]	60 diameter x 310 length
Weight in air	3.5kg (with batteries)
Weight in water	2.0kg (with batteries)
Direction of sensor-X	Polarisation slot on base

Environmental

Operating	2° C to 30° C
Storage	-5° C to 50° C
Pressure rating	3000 m water depth
Seals	3 'O-rings' on cap

